Australian Government
Department of Defence
Defence Science and
Technology Organisation

Aerosol Characterisation in the Northern Territory of Australia during the Dry Season with an Emphasis on Biomass Burning

S. B. Carr, J. L. Gras, M. T. Hackett and M. D. Keywood

Intelligence, Surveillance and Reconnaissance Division
Defence Science and Technology Organisation

DSTO-RR-0298

ABSTRACT

Results are presented on the atmospheric aerosol derived from aircraft measurements in the vicinity of Jabiru in Kakadu National Park during June and September 2003. The focus of the measurements was on the biomass burning aerosol (smoke) which is ubiquitous throughout the Northern Australian dry season (June - October). Data were also obtained on the coarse mode aerosol which is composed mainly of sea salt and soil. A comprehensive characterisation was made of the aerosol microphysics, chemistry and optical properties. Additional ground based measurements were made at Jabiru to more fully characterise the chemistry of the boundary layer aerosol. A range of instrumentation was used including particle sizing instruments mounted inside the aircraft and two external aerosol spectrometer probes which were used to measure the aerosol number size distribution. Additional instrumentation included a filter-sampler to collect particles for chemical analysis, a nephelometer to measure the aerosol scattering coefficient, an absorption photometer to measure the absorption coefficient and various meteorological sensors. Results show clear differences between the beginning and the end of the dry season most notably in terms of smoke concentration aloft and the relative abundance of fresh and aged smoke. The vertical aerosol profiles changed markedly between months primarily due to the difference in mixing depth.

RELEASE LIMITATION

Approved for public release

Published by

Intelligence, Surveillance and Reconnaissance Division
DSTO Defence Science and Technology Organisation
PO Box 1500
Edinburgh South Australia 5111 Australia

Telephone: (08) 8259 5555
Fax: (08) 8259 6567

AR-013-472
August 2005

APPROVED FOR PUBLIC RELEASE

Aerosol Characterisation in the Northern Territory of Australia during the Dry Season with an Emphasis on Biomass Burning

Executive Summary

The importance of a detailed understanding of aerosol microphysics and chemistry cannot be overstated. From studies of global climate change to pollution monitoring and the consequent health effects aerosol, is a critical factor. The Australian Defence Force (ADF) employs a large number of communications, weapons and surveillance systems in the field that are all impacted upon by the atmospheric aerosol. This is particularly the case for imaging electro-optical (EO) systems either ground based (IRST, FLIR) or operated from airborne platforms (imaging hyper spectral systems). The atmosphere attenuates the energy output of the targets (signal) of interest and can affect the spectral and spatial features of the target and background. For this reason an atmospheric model such as MODTRAN [1] is critical. This model has been developed for Northern hemisphere environments and has often been employed in southern hemisphere environments. This needs to be done with great care. The major molecular constituents are likely to be fairly well represented by MODTRAN; on the other hand aerosols being produced often on a local scale are less likely to be adequately represented by the current models within MODTRAN. At the very least the adequacy of these models needs to be tested.

Task LRR 01/205 Atmospheric Aerosol Research aimed to fill in gaps in DSTO's knowledge about regional aerosol properties and to examine the adequacy of models such as MODTRAN for regional usage. The atmosphere is obviously a very large and complex environment that does not lend itself to simple or inexpensive analysis. For this reason it was decided to focus on a specific area that was important both from an operational perspective and that offered a unique regional environment to test the validity of aerosol models.

The region of Jabiru in Kakadu national park was chosen during the Northern Australia dry season. Two aircraft measurement campaigns were undertaken during June and September 2003 to characterize the seasonal variation (beginning to end) in the aerosol properties of the region. The main source of aerosol is biomass burning, and whilst not being unique to this continent, certainly the type of fuels and burning patterns used are unique; hence there is a need to study and characterise this aerosol in its own right. This report outlines the methodology employed to achieve this characterisation. Applications of the data to model validation will be reported on separately as will measurements taken across the continent during transit between Adelaide and Darwin [3].

The value of this work to the ADO will be a better understanding and usage of atmospheric aerosols models such as those found in MODTRAN. This will improve the

prediction capability of the ADO and allow for sensor optimisation both in terms of influencing procurement decisions and in deployment of systems. This will be primarily through modelling and simulations studies, though evaluation of operational systems and developmental systems on platforms such as the ISR test bed aircraft are extremely valuable. Knowledge of the atmosphere and its effects on military systems whilst important is only one aspect of the problem. Studies of the systems themselves, targets and environments (backgrounds) and the operational scenarios need to be undertaken to enure that the best systems are acquired and are deployed optimally for Australian conditions and in joint operations regionally or abroad.

Authors

Dr Stephen Carr

Intelligence, Surveillance and Reconnaissance Division

Before joining DSTO as a Research Scientist in early 1998, Dr Carr completed an Honours Degree in 1991 and a PhD in 1996 both in Theoretical Physics at The Flinders University of South Australia. Shortly after joining the Weapons Systems Division he became Task Manager of the Infra Red Search and Track (IRST) task for the Navy which he worked on from 1998 through to the end of 2001. During his time in WSD he was involved with work on anti-personnel land mine alternatives and land based IRST as part of ground based air defence studies. Since joining ISRD in 2001 as a Senior Research Scientist he has been Task Manager for LRR 01/205 Atmospheric Aerosol Research. This work has involved experimental measurements both ground based and on an aircraft done in collaboration with CSIRO and University. He has also gained additional knowledge on EO and IR systems beyond wide band systems such as IRST to include hyperspectral systems in particular in both visible and IR wave bands.

Dr John Gras

CSIRO – Division of Marine and Atmospheric Research

Dr Gras is a Senior Principal Research Scientist leading a team in the study and measurements of Air Pollutants: Sources and Exposure in CSIRO's Division of Marine and Atmospheric Research at Aspendale Victoria. He has some 30 years of experience in the study and measurement of atmospheric aerosol including multiple aircraft missions.

Ms Michelle Hackett

Intelligence, Surveillance and Reconnaissance Division

Michelle Hackett completed a Bachelor of Science, majoring in mathematics and physics, followed by Honours in Applied Mathematics at the University Queensland in 2001. She joined the Defence Science and Technology Organisation (DSTO) as a graduate and has been working in the Imaging Electro-Optics Systems (IEOS) group of the Intelligence, Surveillance and Reconnaissance Division (ISRD) until the present. During her time in the IEOS group, Ms Hackett has been researching the retrieval of atmospheric properties from remotely sensed

hyperspectral data. She has also contributed to the analysis of data in the Atmospheric Aerosol Research task.

Dr Melita Keywood

CSIRO – Division of Marine and Atmospheric Research

Dr Keywood is a Research Scientist working in the team lead by Dr Gras. She is also based at Aspendale in the Division of Marine and Atmospheric Research. Her main area of research interest involves the study of the chemical composition of atmospheric pollutants, including aerosol

---

Contents

1. Introduction

This report is the second in a series of three documenting atmospheric aerosol measurements undertaken during 2002 and 2003. The two other reports addressed ground-based measurements made at Jabiru in Kakadu National Park, Northern Territory (N.T.) Australia, during 2002 [2] and transcontinental aerosol measurements made between Adelaide and Darwin in 2003 [3]. In this report the results from two separate aircraft measurement campaigns conducted over Jabiru in June and September 2003 are presented. An additional report using the results presented here is planned, to investigate the applicability of models of atmospheric aerosol used in the study on the performance of electro-optical (EO) sensors in the tropical North of Australia.

There are very few airborne measurements of atmospheric aerosol for continental Australia. Previous measurements have been undertaken by CSIRO in collaboration with other agencies. These measurements have been mainly over the Eastern part of the continent [4]. A few campaigns have focused on characterising biomass burning smoke in both the Northern Territory and parts of Indonesia (Borneo) [5,6]. This includes measurements on the scattering coefficient enabling differences between the two regions to be highlighted.

Ground based measurements have also been conducted at Jabiru during 1995-1996 [7]. This data was useful as it enabled the identification of major sources of boundary layer (BL) aerosol in the region. To enable a more complete characterisation of the aerosol spatial distribution, further airborne measurements were considered necessary. A complete characterisation involves measurements of the microphysical, chemical and optical properties of the atmospheric aerosol (a closure study).

The focus of this activity is on the characterisation of biomass burning aerosol in the Northern Territory of Australia during the 2003 dry season. The available resources limited the study to a few select sampling windows at the beginning and at the end of the dry season (June and September). Despite this, good cross sections of data were obtained, affording a unique characterisation of the regional aerosol.

A range of scientific instrumentation was fitted to an aircraft (King Air). This equipment was either purpose built for aircraft sampling or was suitably modified to sample from an aircraft. An isokinetic inlet was fitted externally to the fuselage of the aircraft. This inlet was fed into the cabin of the aircraft providing suitable sampling lines for a range of aerosol measuring equipment.

Data were collected on the size distribution, concentration, light-scattering, light-absorption and chemical composition of the aerosol. Multiple sensors were employed to offer redundancy and to cover a significant amount of the aerosol size spectrum. This included an integrating nephelometer, an aerodynamic particle sizer (APS), a

scanning mobility particle sizer (SMPS), two externally mounted aerosol probes, an absorption photometer and filters to collect particulate material for later chemical composition analyses.

A joint activity was conducted, involving three research groups from the Defence Science and Technology Organisation (DSTO), the Commonwealth Scientific and Industrial Research Organisation's (CSIRO) Division of Marine and Atmospheric Research and the Queensland University of Technology (QUT). Airborne Research Australia (ARA) was contracted to provide the aircraft, pilot and engineer to support the activity.

1.1 Background

The principal aim of this activity was driven by a research program at DSTO to characterise regional aerosol from the point of view of atmospheric model validation. The initial focus has been on biomass burning aerosol in the top end of the Northern Territory of Australia. It was decided, at an early stage, that this could only be done rigorously by undertaking a fundamental study on aerosol including microphysical, chemical and optical properties. In particular knowledge about the vertical distribution of aerosol properties was considered important. Whilst the main objective was very narrowly defined, the application of the results of this work has a much wider scope.

2. Location and Aerosol Sources

2.1 Flight Plans

This activity was spread over two separate campaigns, one at the beginning, and the other at the end of the northern Australian dry season. The dry season extends from June through to October, with November typically marking the start of the build up towards the wet season. The base for flight operations was RAAF Base Darwin. The profiles flown were vertically stacked horizontal flight legs between around 0.5 and 6.0 kilometres (km). Each horizontal leg was 20 or 30 minutes in duration and the orientation of the legs was from a point southwest (SW) of Jabiru (13^0 07.53′ south 132^0 31.97′ east) to a point northeast (NE) of Jabiru (12^0 11.43′ south 133^0 15.12′ east) in Kakadu National Park, centred over Jabiru (Figure 1). The above latitudes and longitudes apply to September, when all flight legs were 20 minutes duration, with the aircraft moving with a true air speed (TAS) of around 100 metres per second (m/s). In June the flight path had the same orientation as for September but was centred over a point approximately 2 km east of Jabiru and the flight leg durations where either 20 or 30 minutes. This orientation was initially chosen so that the flight legs were perpendicular to prevailing wind directions on the ground. During the daytime, winds were predominantly from the southeast. The wind directions were variable from morning to afternoon and at different altitudes so this choice of orientation of the flight

legs turns out not to be that critical. This procedure ensured that the flight legs followed west of the escarpment that divided the terrain quite distinctly. The majority of fires that impacted on the measurements undertaken were located east of Jabiru, clustered in several parts of Arnhem Land.

The entire activity was referred to as the aircraft measurements campaign. This comprised the June 2003 and September 2003 campaigns. A total of 64 aircraft hours were available including for flight tests and ferrying flights.

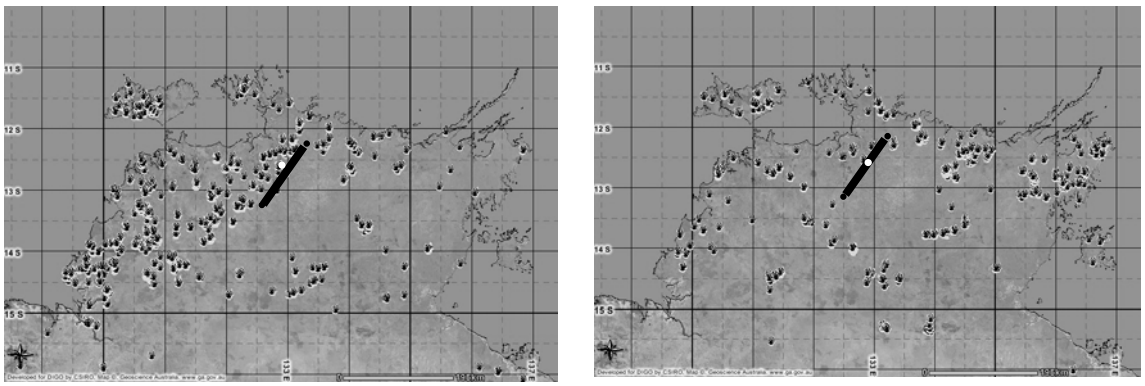

Figure 1: Maps of the Top End of the Northern Territory showing satellite fire spot data for 22-28 June 2003 (left) and 21-27 September 2003. The (black) lines indicate the flight paths flown at various altitudes between 0.5 and 6.0 km. In June the flight path was centred over a point about 2 km east of Jabiru airport (marked white) with the same orientation as for September.

Fire maps from the sentinel website [8], showing fire spot detections during the periods of the aircraft measurements (Figure 1), have been reproduced here with permission. The general location of flight paths is overlaid on these images, with Jabiru airport highlighted by the white dot. The fire spot data can be misleading. It shows transient events by detecting the differences between a bright pixel and the background. In the majority of cases genuine fire spots are detected, albeit with some false alarms. The satellites make a number of passes each day but in some cases the satellites' swaths do not cover Jabiru and the surrounding area. The cumulative effect of months of burning is not highlighted in this data. The instruments that measure particle concentration and particle scattering of light show elevated levels of smoke present in the atmosphere in September. While there may be more spot fires for the week of June there is more smoke in the atmosphere in the week of September (smoke lingers for weeks being constantly replenished during the dry season). This applies in general to the months of June and September.

For each campaign, four flights were conducted, each of approximately four hours duration. This included transit from Darwin to the sampling station, a vertical stack of horizontal flight legs and return transit to Darwin. For June, the flights were on the Monday, Tuesday and Thursday afternoons with the final flight on the Friday morning (Table 1). The conditions in June were fine and clear for the most part.

In September two morning (Tuesday and Thursday) and two afternoon (Monday and Friday) flights were conducted. Weather conditions were mainly fine, with some cloud cover on most days. Generally, the cloud band would increase in the early afternoon and be present at around 3.0 to 4.5 km in altitude. In the mornings the cloud cover was generally lower, at around 0.5 to 1.2 km and narrower, allowing measurements across the free troposphere (FT) boundary layer interface. The preference was for afternoon flights due to the build up of fires, but this was tempered due to the cloud conditions encountered. There is quite a difference between the results obtained in the morning and the afternoon. The altitudes selected were based on the objective of the flight, which was to obtain boundary layer data alone, or a combination of boundary layer and free troposphere data. Clouds also impacted on the choice of altitudes that were flown. The minimum altitude was set at around 0.5 km (1500 feet), primarily for aircraft safety reasons and the maximum altitude flown was 6.0 km (20 000 feet). A summary of the flights is given in Table 1. This includes time, location and the purpose of each flight. Times are given in Australian Central Standard Time (CST), which is 9.5 hours ahead of coordinated universal time (UTC).

Table 1: Summary of campaign flight plans. BL – Boundary Layer and FT – Free Troposphere.

Campaign	Flight #	Date/ Start Time	Flight Leg Altitudes (km)	Flight leg duration (mins)	Objective
	1	23rd 14:00	0.61, 0.91 (x2), 1.37.1.52, 1.83 & 2.44	30	BL
June	2	24th 13:30	0.76, 1.68, 3.05, 4.57 & 6.1	30	BL/FT
	3	26th 13:30	0.46, 0.76, 1.07, 1.37, 1.68, 1.98 & 2.29	20	BL
	4	27th 07:30	0.46, 0.76, 1.37, 1.98, 3.05 & 4.57	20	BL/FT
	1	22nd 13:15	0.61, 1.22, 1.52, 1.83, 4.57 & 6.1	20	BL/FT
September	2	23rd 08:00	0.46, 0.76, 1.22-1.52, 1.83, 2.44 & 3.05	20	BL
	3	25th 07:00	0.46, 0.76, 1.83, 2.44, 3.05, 4.57 & 6.1	20	BL/FT
	4	26th 11:30	0.46, 0.91, 1.22, 1.83, 2.44 & 3.05	20	BL

Measurements were also made on the transcontinental ferrying flights between Adelaide and Darwin passing over the centre of the continent with a refuelling stop in Alice Springs. These results are presented in a separate report [3]. All the measurements (including the transcontinental flights) were carried out in the same time zone hence times are specified in Australian Central Standard Time.

2.2 Ground Based Measurements

Instruments were installed at Jabiru, approximately 250 km east of Darwin, to enable collection of aerosol filter samples for detailed chemical analyses of the boundary layer aerosol. The instruments were installed at the Environmental Research Institute of the Supervising Scientist (ERISS) field station located opposite Jabiru airport, which is situated in Kakadu National Park. The aircraft flight paths were also centred over Jabiru. The airport and facilities at Jabiru were not appropriate to support our

activities. Hence the aircraft was based at RAAF Base Darwin and operated out of the section designated for night flight testing (NFT). All equipment calibrations, maintenance and preliminary data analyses were performed in Darwin.

2.3 Aerosol Sources

The main sources of aerosol expected for this region are biomass burning, the maritime environment and soil disturbance lofting mineral dust. Jabiru is approximately 60 km from the coastline; hence the coarse mode aerosol is expected to consist primarily of sea salt. There is little agricultural activity in the region but there is a mine nearby (Ranger) southeast of Jabiru airport. Over the majority of flight legs, surface disturbances are likely to be localised, minor and infrequent. Biomass burning is a constant occurrence throughout the dry season. Early in the dry season land managers light the majority of fires. The bulk of the burning is low intensity with removal of denser undergrowth that has built up over the preceding wet season. Towards the end of the dry season, fires become more intense as drier fuel sources are consumed. During this period the indigenous population lights a large number of fires. This is particularly the case in Arnhem Land where the grassy fuel dries out later in the year compared with the Western regions, and is thus prone to fires being started due to natural causes or accident when the fuel is tinder dry. On any given day the number and location of fires can vary greatly. Background smoke levels between June and September changed markedly.

Winds at ground level were mainly easterly. Many fires appeared in Arnhem Land, between the months of June and September, extending across the Arnhem Land plateau east of Jabiru to the Gulf (Figure 1). During flight 4 in September there were some fires (horseshoe fire front configuration) at the northeast limit of the flight legs, just east of the flight paths, which do not appear in Figure 1. The reason why they were not detected is unknown. In September the majority of the smoke crossing our flight paths emanated from the fires in Arnhem Land. The region of Arnhem Land can be divided into three bioregions. The Arnhem Land coast (ARC), Arnhem Land plateau (ARP) and central Arnhem Land (CA) [9]. Most fires emanated from the ARC region adjacent to the boundary with the CA region. This region consists of Darwin Wollybutt and Darwin Stringybark (both types of eucalyptus) in an open forest with an understorey of (sorghum) tussock grasses. The same eucalypt species were present in the CA region in an open forest to woodland with grass understorey. Fewer fires were present in the ARP region. Furthermore they were less likely to have impacted on any measurements. The exception would have been if the winds were strongly from the southeast, then this smoke may have crossed the flight paths. The measurements show that the greater smoke concentrations were found at the northeast limit of flight legs. This smoke emanated mainly from fires directly east of Jabiru in the ARC and CA regions. The ARP region consists of variable Bloodwood and Darwin Wollybutt open forest to woodland with spinifex understorey. More details about these bioregions, broad vegetation and specific vegetation communities can be found at the Tropical Savannas CRC website [9].

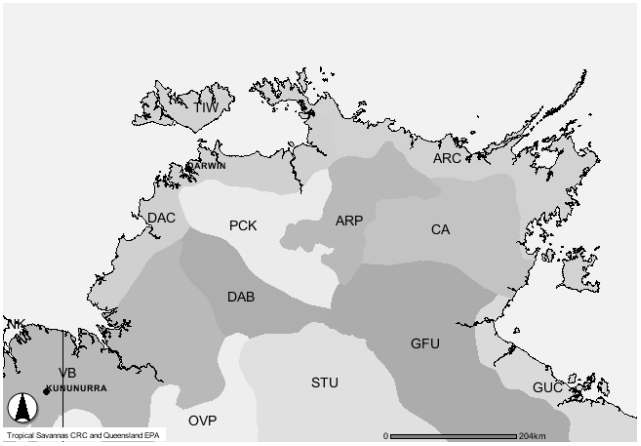

Figure 2: Map of the Top End of the Northern Territory showing the different bioregions. The CA, ARP and ARC regions are where the majority of fires were located that impacted on the reported measurements.

In June there was very little fire activity in the Arnhem Land region and hence much lower concentrations of accumulation mode aerosol were measured. Fires to the west and to the south of Jabiru were prevalent in hotspot satellite data [8]; this also occurred in September. The fire spot data can be misleading, as the intensity of these fires is not known and hence the relative amount of fuel burnt may be quite different between the months of June and September. During the week of the experiment in June there was more burning southeast of Darwin than in September, despite the fact that smoke concentrations in the atmosphere were smaller. During flight 1 in June one flight leg (0.91 km) was made west of Jabiru where there was a build up of fires in Kakadu. Winds were predominantly from the southeast hence the instruments did not measure this smoke on the original flight path. This region consists mainly of Darwin Boxwood and Round-leaved Bloodwood woodland with sorghum understorey to the south of Jabiru and Darwin Woollybutt and Darwin Stringybark open forest with sorghum understorey to the west and north of Jabiru. During flight 4 in June the aircraft flew southwest from Darwin to measure smoke that was present from fires the previous day before tracking northeast to the selected flight path pattern over Jabiru. The same vegetation classes were encountered in this region with a pocket of fires located in a region consisting of Darwin Stringybark and Darwin Woollybutt open forest with perennial and annual grass understorey.

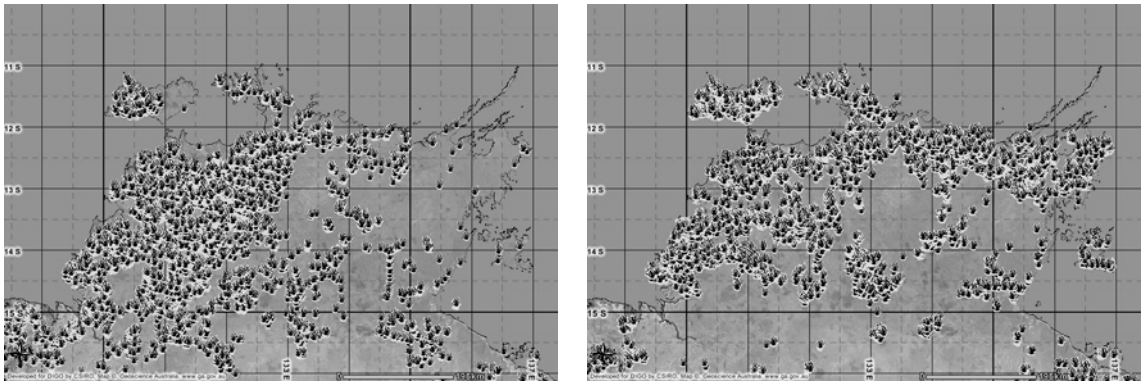

Figure 3: Cumulative fire spot detections for the periods 01 April – 28 June and 29 June – 27 Sept, 2003. During the early part of the dry season there is more burning occurring over the region southwest of Darwin due to controlled burning primarily by land managers. During the later stages there is a much great prevalence of fires across the top of Arnhem Land out to the Gulf. These fires are primarily a result of natural occurrences and the indigenous population.

The changes of biomass burning from the months of June and September 2003 reflect annual burning patterns that have been observed over many years.

2.4 Previous Measurements of Aerosol Composition at Jabiru

Filter measurements of the fine and coarse aerosol present in Jabiru were made over a 19-month period during 1995-1996 [7]. Those data were analysed for particulate mass, black carbon and over 40 elements. Absolute principal component analysis (APCA) of the fine size fraction identified 5 components - mineral dust, sea salt, biomass burning, sulphate and pollution components. Of these, four were used in chemical mass balance (CMB) receptor modelling techniques leaving out the pollution component and including a pure ammonia sulphate profile. For the CMB on the course data set three source profiles were used leaving out the biomass burning profile. The results of the CMB are given in the table below summarised from the reference mentioned above.

Table 2: Aerosol sources at Jabiru (1995-1996).

Component %	*Fine particle fraction (83% accounted for)*	*Coarse Particle fraction (67% accounted for)*
Biomass burning (dry season)	60%	
Sulphate		4%
Mineral Dust		36%
Sea Salt		27%

These analyses do not give any information on how the missing mass might be apportioned, although for the fine fraction, additional biogenic organic aerosol or nitrate components were postulated. Similar components were identified from the ground based filter measurements made at Jabiru for the present study (Section 4.1.3).

3. The Aircraft and Instrumentation

DSTO contracted the use of a commercial research aircraft from Airborne Research Australia. The Beech Super King Air B200T has been configured for scientific payloads and included specialized hard points. This aircraft had previously been used during the ACE Asia experiment [10] for which it was fitted with aerosol measuring equipment including wingtip probes. This assisted our efforts by making the current installation of aerosol measuring equipment relatively straightforward from an engineering and safety clearance point of view.

The aircraft was able to carry for four 19-inch racks plus four personnel including the pilot. The placement of equipment and racks was determined by space restrictions and by the location of the isokinetic inlet.

Figure 4: This first image shows the King Air with the isokinetic inlet protruding from the top right of the fuselage (long horizontal shroud). The four racks are visible in the second image. This image is taken looking towards the front of the aircraft. The APS and nephelometer are located in the rack on the right hand side of the image below the isokinetic inlet sub-sampling lines, which feed into the cabin. The rack in the background contains the SMPS whilst the two racks on the front left contain CSIRO equipment. Generally, conductive silicon tube or copper tube was used to plumb the instruments. The large loop of plastic tube above the APS rack connects the exhaust port of the manifold to the exhaust outlet.

Some of the equipment was mounted in racks with anti-vibration mounts. Temperatures inside the instruments when the aircraft was airborne were typically around 30 ^{o}C. On the ground, aircraft temperatures were extreme during the middle of

the day, which resulted in some instruments reaching their recommended upper operating temperatures during calibration and testing. To avoid overheating the APS during testing in the aircraft on the ground, the external cover was lifted and air was blown over the internal components of the instrument using a small fan.

3.1 Instruments Overview

DSTO instruments included a Thermo Systems Incorporated (TSI) 3563 three wavelength integrating nephelometer [11] and a TSI 3321 Aerodynamic Particle Sizer [12]. Both were fitted to a single 19-inch rack. This rack also contained a sine-wave inverter providing 1000 watts continuous AC. This was used to power DSTO and QUT equipment. It was fed directly from the aircraft 28-volt DC supply. The rack was placed as close to the isokinetic inlet as practical. It was necessary to mount the nephelometer vertically, placing the inlet in an awkward location with respect to the isokinetic inlet sub-sampling line. The APS was positioned directly under its sub-sampling line and was connected by a short length of conductive silicon (consil) tubing. Consil tubing was used to plumb all DSTO instruments; both inlet and exhaust lines. This prevented electrostatic charge build up along the sampling line.

QUT instrumentation included a TSI Scanning Mobility Particle Sizer [13] with a configuration composed of a TSI 3010 Condensation Particle Counter (CPC) and TSI 3080 Electrostatic Classifier, along with a short 3081 Differential Mobility Analyser (DMA). For the September campaign a TSI nanometer aerosol sampler and a TSI P-Trak Ultrafine particle counter for direct plume concentration measurements were also included (results not presented here). All of these instruments were mounted in a single 19-inch rack.

CSIRO instrumentation comprised an isokinetic inlet [14], two external aerosol probes (Active Scattering Aerosol Spectrometer Probe (ASASP-100X) and a Forward Scattering Spectrometer Probe (FSSP-100) [15]), an absorption photometer, filters to collect particles for mass and chemical analysis, a giant particle impactor plus various meteorological sensors. A video was made through the co-pilots window to provide situational information. Audio recordings of voice communications between scientists and the pilot were also made.

CSIRO data were logged to the CSIRO data acquisition system (DAS), as was the global positioning system (GPS) data. DSTO and QUT data was collected on two separate laptop computers using TSI propriety software, with synchronisation carried out before each flight to GPS time. Additionally, time markers recorded on the CSIRO DAS at various stages throughout each flight were also used to assist with time synchronisation. CSIRO also installed and operated a suite of ground based aerosol equipment at Jabiru to complement the airborne measurements. This also allowed sufficient mass to be collected to enable a detailed chemical analysis of the BL aerosol.

Aircraft-based meteorological sensors included reference wet and dry thermometers, used for ambient humidity determination, a Rosemount reverse flow thermometer for determination of ambient air temperature, and a pitot-static pressure sensor for determination of ambient pressure and aircraft true airspeed.

Table 3: Aircraft mounted aerosol size distribution instruments

Instrument (sizing)	*Nominal Radius* μm	*Location*
SMPS	0.013 - 0.573	Internal
APS (aerodynamic diameter)	0.487 - 20.5	Internal
ASASP-100X	0.2 – 3	External
FSSP-100	4 – 50	External
Giant Particle Impactor Slides	> 1	External

Table 4: Other aircraft mounted instrumentation

Instrument (other)	*Measured Quantity*	*Purpose*	*Location*
Nephelometer	Light scattering coefficients @ 450, 550 & 700 nm	Measure the amount of attenuation due to particle scattering	Internal
Absorption Photometer	Light absorption coefficient @ 525 nm	Measure the amount of attenuation due to particle absorption	Internal
Single particle collector (filter)	Particulates on filters (separate filters above and below the BL)	Chemical and morphological ID of individual species	Internal
Mass sampler	Total particulate mass (separate filters above and below the BL)	Total conc. of chemical species	Internal
Nanometer Aerosol Sampler (Sept only)	2-100 nm particles on TEM grids	Chemical and morphological ID of individual species	Internal
P-TRAK Ultrafine particle counter (Sept only)	Ultra fine particle counts (D > 10 nm)	High temporal resolution meas. of ultra fine particle conc.	Internal

Table 5: Ground based instrumentation at Jabiru

Ground Based Instrument	*Measured Quantity*	*Purpose*
MOUDI – 12 stage impactor	Size – segregated particles collected on polycarbonate substrates – 24 hr samples	Sized resolved chemical composition – soluble species by Ion Chromatography (IC) and insoluble species by nuclear methods (PIXE/INAA)
NOAA impactor 2-stage	PM1 samples collected on quartz filters	Organic carbon, elemental carbon and water soluble organic carbon
GRIMM – solid-state-laser single particle spectrometer /counter	Size distribution 0.3 – 20 μm (15 sizing channels)	Data on size distributions on the ground
Dry nephelometer	Light scattering coefficient @ 530 nm	Measure scattering at low humidity
Ambient nephelometer (Sept only)	Light scattering coefficient @ 530 nm	Measure scattering at close to ambient humidity

In the above table TEM refers to transmission electron micrograph, PIXE to proton induced x-ray emission and INAA to instrumental neutron activation analysis.

3.2 The Isokinetic Inlet

The isokinetic inlet provides two-stage deceleration of the airflow with a boundary layer bleed included immediately prior to the second decelerator to inhibit flow separation. Contained within the two-stage decelerator are six sub-sampling lines with internal diameters ranging from 4.75 mm up to 13 mm. These sub-sampling lines are designed for volumetric flow rates of between 1.7 and 28.5 litres per minute (L/min) for isokinetic sampling at an air speed of 100 m/s [14].

The two-stage decelerator resulted in a reduction of airspeed by about a factor of 20. Laminar flow is maintained within the decelerator and the six sub-sampling lines are orientated to face into the decelerated airflow. The lines then follow an open bend, terminating inside the cabin where they are coupled to various sampling lines that plumb the equipment inside the aircraft. All sampling equipment exhausts via a manifold that was connected to an exhaust line, which is built into the isokinetic inlet structure. The inlet has been tested by CSIRO on board an aircraft using internally and externally mounted particle spectrometers. It was concluded that no systematic size dependent sampling artefacts are evident for the inlet for particles with physical diameters less than around 3 μm. Larger particles are still transmitted through the inlet, as shown by measurements using the aerodynamic particle sizer, although the passing efficiency is reduced for larger sizes. The placement of the isokinetic inlet was fixed from a previous deployment, where it was placed to sample air with minimal impact from streamline deformation by the aircraft fuselage and propeller flow [16].

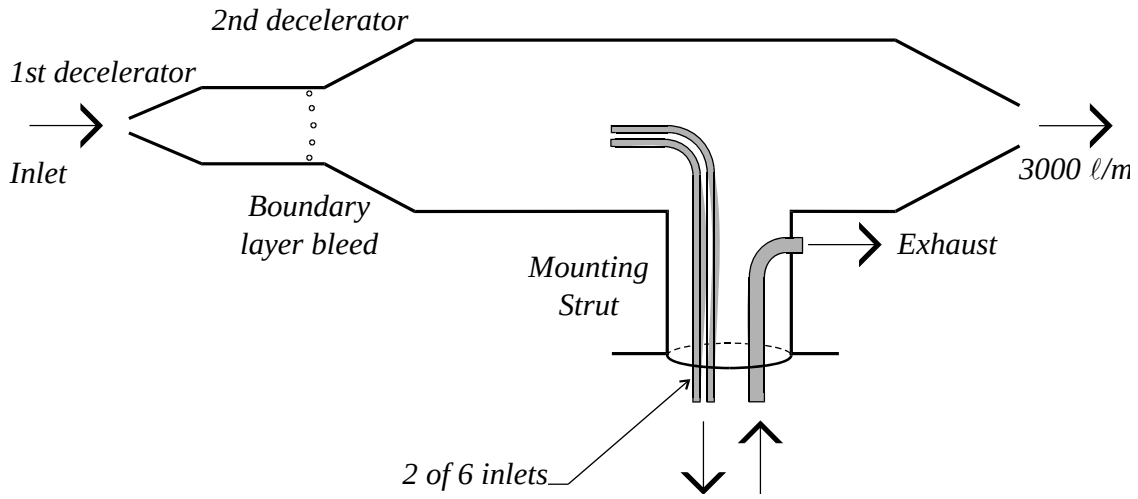

Figure 5: A schematic diagram of the CSIRO isokinetic inlet (not to scale).

3.3 The APS and Nephelometer

The APS was mounted on anti-vibration mounts using a lightweight aluminium plate, and the nephelometer was mounted securely within the rack via brackets. The top bracket was insulated from the rack using a piece of plastic foam. The method by which these instruments sample outside air is critical to performing accurate measurements. A great deal of care and attention was paid to the method by which the aerosol was aspirated into the sub sampling lines via the isokinetic inlet and to the coupling of transport tubing to various inlets. Conductive silicon tube was used to plumb both instruments including exhaust lines.

The nephelometer was calibrated before each flight. During September a zero baseline measurement (ZMB) measurement was also performed before each flight and then again before and immediately after each stack of horizontal flight legs. Data were also collected on the noise response of the instrument before and after most flights. For both campaigns the sizing accuracy of the APS was tested before, in the middle of, and after each campaign. This included sizing polystyrene latex (PSL) spheres at 1 μm, 3 μm (for September only) and 5 μm. Sizing calibrations of the APS were not conducted during the measurement campaigns due to the inherently stable operation of this instrument. A full calibration was carried out in May 2003 before the aircraft measurement campaign. The APS flows (sheath air and aerosol flow) were also measured before each campaign using a Gilibrator flow meter and were found to be within specification.

3.3.1 Sampling Issues

3.3.1.1 On the Aircraft

A stainless steel adaptor was machined for the APS that allowed coupling between the 0.95 centimetre (cm) consil tube and the 1.91 cm APS inlet to provide laminar air flow (a half angle of less than 7 degrees) [17]. A similar adaptor was machined that coupled the 0.64 cm isokinetic sub sampling line (made of stainless steel) to the consil tube. The volumetric flow rate through the 0.64 cm sub sampling line was around 4.8 L/min closely matching the sample flow rate of the APS (aerosol plus sheath flow).

For the nephelometer similar adaptors were machined enabling sampling from the 0.95 cm sub sampling line through the 0.95 cm consil tubing and into the 1.91 cm nephelometer inlet. The flow rate of the nephelometer was maintained between about 11 and 14.5 L/min closely matching the flow rate through the 0.95 cm sub sampling line of the isokinetic inlet (13.3 L/min). The inbuilt blower on the nephelometer was used to provide the flow through the instrument and was operated at about 20% of maximum power. This resulted in the nephelometer operating outside of its specified flow rate but enabled close to laminar flow to be maintained through the 0.95 cm consil tube.

In the absence of a complete study of the isokinetic inlet sampling performance in a wind tunnel with the APS and nephelometer plumbed as on board the aircraft, estimates of particle loses can be made using theoretically and empirically determined equations [18], although these corrections have not been applied to the APS or nephelometer data. The reasons behind this decision rest on the measurement being made. For the APS where size distribution is being measured, the FSSP provides a potentially more accurate measurement of the aerosol size distribution for diameters greater than 3 μm and certainly 5 μm. The majority of particle losses will occur inside the isokinetic inlet for sizes above 3 μm both as a result of the deceleration of the airflow and mismatch in velocity between the air inside the shroud and inside the sub sampling line. There will also be counting inefficiency associated with the APS itself, affecting concentration measurements. This effect is most noticeable below 1μm and above 3 μm. The APS data were used to fit size distribution functions that were truncated below about 1.5 μm. Therefore losses due to counting inefficiencies will not impact significantly on our analysis.

For the nephelometer the situation is different. The nephelometer measures an integrated quantity, namely the aerosol scattering coefficient. This involves an integral over the size distribution across the entire size range, albeit not weighted equally over size (the distribution tails off for larger particles, being lognormal in nature). Particle losses above 3 μm through the isokinetic inlet will impact on the measurement of the scattering coefficients particularly at the red wavelength. The concentration of coarse mode aerosol aloft is generally very low and its contribution to scattering minimal, when compared with the fine mode aerosol. Ideally, the effect of large particle losses

on the scattering coefficients should be taken into account, but this is not likely to affect the results appreciably. The exception may be during some of the early morning flights in September in the lower boundary layer region. In this region, as the analysis in Section 6.2 shows, the coarse mode concentration appears to be dominated by sea salt, which peaks in number concentration through the early hours of the morning (Section 6.2) and shows up as a lower Angstrom exponent (Figure 25). The situation for June is less clear due to the very small scattering coefficients that were measured particularly for blue and red wavelengths, which were often at the detection limit of the instrument.

3.3.2 Sampling Methodology.

In June, sampling times were set between 60 seconds and 600 seconds. This was reassessed during the course of initial sampling and ultimately the sampling time was set to 60 seconds for the APS and between 60 seconds and 300 seconds for the nephelometer. The longer sampling time for the nephelometer was used in the clean FT where the scattering signal often fell below the detection limit of the instrument. In September the aerosol concentration was typically 10 times higher in the BL (for the APS) and the APS sampling time was set to 30 seconds and also for the FT. For the FT, post analysis of the data was used to obtain average flight leg size distributions. For the nephelometer the averaging time was set to 60 seconds. In the FT this was usually increased to 240 seconds, providing twice the sensitivity but reducing the horizontal resolution.

Proprietary TSI software was used to log data from both instruments via a laptop computer. The Aerosol Instrument Management (AIM) software was used to control and log data for the APS. This software provides real time feedback to the user on the size distribution, concentration and statistical measures of the size distribution such as the count median diameter (CMD) associated with the sample, plus instrument status. Nephlog and NEPHWIN software was used to control and log data for the nephelometer.

A new file was created for each flight leg containing the samples over that flight leg. Post analysis of the data involved calculating flight leg average size distributions for the APS and modified box plots for the nephelometer. The nephelometer employs a real time smoothing filter on the photo multiplier tube (PMT) signal, it is this filtered signal that is averaged over the time set by the user which is generally less than 5 minutes. Rather then collect continuously, the sampling time of the nephelometer was based on the observed aerosol concentration. This limited the amount of post processing of data as the nephelometer was performing the averaging. To limit the amount of data collected by the APS the sampling time was set to no less than 30 seconds. In most cases it was necessary to calculate an average over flight legs, as the coarse mode aerosol concentration was low. Further averaging was then performed over regions (lower and upper boundary layer and the free troposphere) and flights to gain reliable counting statistics. Averaging over APS samples gives a real increase in

sensitivity. The ASASP was sampling continuously at one-second intervals and hence provides very good time resolved data on concentration changes.

The APS was operated in summing mode and not correlated mode. This was done to avoid any potential impact on the counting efficiency of the instrument. In theory, sampling in correlated mode should provide more accurate results, since the light scattering intensity measurement capability of the instrument can be used to distinguish between artificial particle counts and real particle counts. However Armendariz and Leith [19] have shown that the collection of correlated measurements of light scattering intensity and aerodynamic particle size introduced significant error to the reported particle concentrations and aerodynamic size distributions for the APS model 3320. They showed that the magnitude of the particle concentration error varied inversely with particle concentration. The APS 3321 is identical in all respects to the 3320, except for an improvement in signal processing that the manufacturer claims improves the small particle sizing efficiency of the instrument and provides for the virtual elimination of false background counts. This could not be verified for the APS 3321 before the measurement campaigns and hence sampling was only conducted in summing mode. During the measurements it was observed that the event 4 parameter indicating 'phantom' large particles was relatively small compared with events 1 (small particle detections logged for concentration but not sized, assumed to be less than 0.523 μm) and 2 (real particle detections). The event 3 parameter indicating coincidence events was also very small. Taken together these results support the observations in the report by the Southern Research Institute [20].

The APS was set to sample unit density particles. This choice will not affect the results of the measurements of the aerodynamic diameter if the density of the particles is less than about 2 g cm^{-3} or greater than 0. 8 $g\ cm^{-3}$. For densities outside this range, Stokes correction is necessary [21]. However Stokes correction was not applied to the data, which is available as an option under the APS software, since in general, the density of the ambient aerosol is not accurately known *a priori*. Subsequent determination based on composition showed that particle density fell within the expected range.

3.4 The SMPS

The information presented in this section was provided by QUT [22]. The SMPS was reconfigured to sample from an aircraft. It was mounted in a single 19-inch rack in two stages. The upper section of the rack contained the electrostatic classifier and the lower section the condensation particle counter. The classifier (mobility analyser) was mounted vertically alongside the CPC. The complete system was configured to resample the sheath and excess air. This provided the most stable operation under vacuum. In this configuration the sample flow rate was around 0.3 L/min. Software was written to log both temperature and pressure and the flows were controlled to maintain a constant volumetric flow rate. To achieve this, additional flow controllers were added to the configuration. Finally the instrument was recalibrated for particle size and concentration.

The 0.64 cm sampling line of the SMPS was coupled to the 4.75 mm sampling line of the isokinetic inlet using an adaptor. A length of 1.5 metres of conductive silicon tube was used. The SMPS sampled sub-micrometre diameter particles, so any losses due to non-isokinetic sampling should be minimal. Estimated diffusion losses for 500 hecto Pascal (hPa), are shown in Table 6, which was the lowest pressure encountered and hence will result in the largest losses due to diffusion.

Table 6: Diffusion losses for the SMPS at 500 hPa.

Particle Diameter (nm)	Losses %
10	6.5
15	3.9
20	1.8
30	1

The SMPS was operated in fast scan mode and took 150 seconds to complete a scan. This is composed of 120 seconds for a full scan of the size range and 30 seconds retrace time before the instrument can sample again. The multiple charge correction algorithm was also employed. A calibration using 100 nanometre (nm) size polystyrene latex (PSL) spheres was conducted before each mission. Butanol was added to the CPC before the aircraft was airborne limiting the risk of spillage and contamination of the aircraft.

There is some noise evident at the extremes of the measured size distributions, which is due to the so-called "smearing" effect. This effect tends to extend the tail of the lognormal distribution and is enhanced when sampling time is decreased. The source of the effect is the finite time needed for the aerosol concentration to change in the tubes that connect the exit of the classifier and the CPC. By using fast scan mode this effect has been enhanced, but there is an offsetting increase in the horizontal sampling resolution.

The measurement range of the SMPS depends on the atmospheric pressure at which the measurements were conducted. When the pressure is low the lower cut point diameter increases. The following highlights how the lower cut point can vary with altitude. The lower cut point is 13.1 nm at 0.75 km increasing to 14.1 nm at 1.2 km and to 15.7 nm by around 3 km. At the beginning of each leg the pressure needs to be manually entered into the software, for calculation of the lower cut-off diameter. The instrument required some time to provide stable pressure measurements before the low cut point could be set and sampling commenced. Irrespective, the concentration of particles in this size range (< 30 nm) is relatively small compared to the total concentration, so the error is small if these lower size bins are excluded.

Determination of the upper cut-off diameter is somewhat different. At higher altitudes the pressure in the SMPS was relatively low. For the same voltage between the electrodes in the EC, arcing will occur at lower pressures. As the upper cut-off

diameter depends, amongst other factors, on the maximum voltage between the electrodes at higher altitudes it had to be manually reduced (reduce the maximum voltage) in order to prevent arcing. As a result both the lower and upper size limits vary as a function of altitude.

3.5 CSIRO Equipment

3.5.1 ASASP-100X

The particle measuring systems (PMS) ASASP-100X is an externally mounted probe owned by the National Institute of Water & Atmospheric Research (NIWA) of New Zealand. The instrument is designed for aircraft operation and incorporates an integrated sub-sampling inlet system. The inlet can be heated in icing conditions but for these flights was operated unheated. This instrument samples at near ambient conditions.

Data from the ASASP-100X were logged once per second using the CSIRO data system with reporting over one-minute intervals. The nominal size range for this instrument is 0.12 μm to 3 μm diameter with 15 size channels. The ASASP was calibrated before the June and September flights using aerosolised and dried monodisperse polystyrene latex particles with sizes ranging from 0.2 to 2.02 μm. The flow rate was set at 0.5 cm^3s^{-1} and was calibrated before flights using a Gilibrator bubble flow meter. This spectrometer is a single particle counting device and hence correction for counter dead-time (or activity) is required for periods with high concentrations. Corrections for activity were applied for all samples. During shipping of the instrument for the first flight series (June) some laser misalignment occurred, which limited the size range to 0.13 to 4 μm (for a refractive index m=1.59-0i). Before the second flight series (September) the misalignment was located and corrected resulting in a nominal size range of 0.12 to 3.12 μm (for m=1.59-0i). On both flights some detuning of the laser's open cavity occurred at higher altitudes resulting in enhanced noise levels that encroached on the lowest size channel, limiting the lower range to effectively 0.22 μm (June) and 0.145 μm (September).

3.5.2 FSSP

The FSSP Probe gives a true *in-situ* measurement of large aerosol particle concentration and size (D > 4 μm nominal). Scattering size is derived by forward scatter of particles within a known scattering volume defined by the laser beam, shaping optics and particle transit times through the scattering volume. This scattering volume is aspirated directly by the aircraft motion and particles are sampled at ambient temperature and humidity. The inlet has a de-icing heater although this was not operated for these flights. The instrument has a 256 channel sizing capability however this is reduced to a practical array of 15 channels to avoid Mie ringing effects. Calibration via a series of glass spheres, with sizes between 7.8 μm and 40 μm, was conducted in the laboratory

before each flight series and confirmed after installation on the aircraft. The nominal range for the June flight was 4.2 μm to 47.3 μm diameter (for non-absorbing spheres). Part of the optics was replaced and realigned for the second (September) flight resulting in a size range of 2.4 μm to 45.6 μm diameter. On both flights, for some altitudes, the noise floor of the instrument encroaches into the first size channel, and these data need to be excluded. Data from the FSSP are recorded at a one-second rate and reported as one-minute integrals.

3.5.3 Aerosol Particle Absorption Photometer

The CSIRO particle absorption photometer is a filter-based device operating at a wavelength of 525 nm. The filter material used was polycarbonate (filter pore size 1 μm). This is a dual channel absorption photometer utilising diffuse illumination and matched detectors operating in an oven at 40^{o}C with a high degree of temperature regulation, and with a measured flow rate of nominally 2 L/min. Light absorption is determined differentially from the two detectors, one of which views the exposed portion of the filter and the other an unexposed portion of the same filter. Airborne operation introduces a number of problems with stability, including pressure induced changes and filter movement which is most pronounced during changes in aircraft altitude. The other significant factor with this type of measurement is the contribution to apparent absorption (the absorption as measured) by scattering. As with particles in the atmosphere, collected particles both absorb and scatter incident radiation. This scattering artefact is strongest for particles that are weakly absorbing (or equivalently those with a high single scattering albedo). Corrections were based on the method outlined by Hanel [23], which incorporates multiple scattering between the collected particles and the filter plus substrate. Scattering coefficients for the scattering correction at 525 nm were derived from the multi-wavelength nephelometer data reduced to the same (dry) humidity as the absorption cell using the humidity-scattering coefficient relationship reported by Gras et al. [6] for 530 nm integrated scattering coefficient, in similar smoke-impacted aerosol in this region.

3.5.4 Large Particle Impactor

A large particle strip impactor was operated on both flight series for additional information on giant particle numbers (redundancy for the FSSP data). Slides have been archived for later additional analysis if required.

3.5.5 Aircraft-mounted Particle Collection

A filter-based sampler was operated on all flights for collection of mass for determination of mass loading and chemical composition. This sampling was conducted at a nominal flow rate of 20 L/min ambient, with actual flow sensed using a mass flow sensor. For all flights the collecting substrates used were PTFE membrane filters (pore size 1 μm). For this type of filter all particle sizes are collected with high efficiency, however the actual collection efficiency for both coarse and fine mode

material will depend on the fractional transmission efficiencies of the isokinetic sampling inlet, sub-sampling and collecting tubing. Due to the relatively short level-leg flight durations and limited overall sample flow capacity of the isokinetic inlet, no attempt was made to take samples on individual flight legs. Instead two filters were set up for sampling over "low" and "high" altitudes with an automatic switch over at approximately 2500 m. Also several individual flights were combined on individual filters, giving a smaller set of composition determinations than flight days.

4. Chemical Composition of Particles

4.1 Ground Based Measurements at Jabiru

For the surface or boundary (mixed) layer, where most of the light extinction will take place, surface measurements can be used to derive size distributions of chemical composition. The concentration of aerosols at ground level and the simplicity of ground-based sampling compared to aircraft sampling make this an essential complement to the aircraft measurements.

4.1.1 Instrumentation

Size resolved aerosol chemistry was determined from samples collected with a Micro-Orifice Uniform Deposit Impactor (MOUDI). The MOUDI is a 10-stage cascade impactor (effectively 12 stage when the inlet stage and final filter are included, as in this work) with the stages having 50% cut-points ranging from 0.056 μm to 18 μm in aerodynamic diameter [24]. In each impaction jet, particle-laden air is directed at an impaction plate; when the jet encounters the plate, the flow streamlines are forced to make a sharp 90^o turn so that the air can flow around the plate and exit the impaction area. Large particles having significant inertia are unable to make the sharp 90^o turn and are carried forward to impact on, and thus be collected by, the impaction plate. Particles with less than a threshold inertia do not impact, but follow the airflow out of the impaction area. Subsequent discussion of the MOUDI data in terms of PM10 (particulate matter less than 10 μm), PM2.5 (particulate mass less than 2.5 μm) and PM1 (particulate mass less than 1 μm) size fractions does not directly use the individual stage data, but is based on a numerical inversion procedure, that yields a smooth size distribution from which each fraction is determined. The cut-points and collection efficiencies of each stage have been specifically calibrated for the MOUDI used in this work by the manufacturer, MSP Inc. This calibration is valid for a flow rate of 30 L/min, with the MOUDI acting as a "critical orifice" ensuring a very well-defined, essentially invariant flow (to within 1 L/min). As an additional check, a gas flow meter was attached to the outlet of the pump so that the total sample volume was measured. In general, the measured volume was within 5% of the calculated volume based on a flow rate of 30 L/min.

Samples were collected for 24 hours, on polycarbonate Poretics filters, 47 mm in diameter with 0.4 μm pore size, which were used for the first 11 stages. A teflon-backed Fluoropore filter 37 mm in diameter with 1 μm pore size was used for the final back-up filter. One sample in June (June 25th) was collected onto aluminium foil substrates.

The MOUDI inversion routine developed by CSIRO was based on an efficient, non-linear iterative inversion procedure of Twomey et al. [25], with the MOUDI stage transmission kernels derived from the Manufacturer's calibration supplied with the CSIRO MOUDI. The individual stage calibration curves were fitted with Winklmayr functions [26], to yield the suite of kernels. Smooth distributions of both the stage kernels and MOUDI mass distributions were obtained by carrying out the calculations using 20 points per decade in logarithmic particle diameter, over the particle diameter range 0.01 to 100 μm.

The inversion procedure convolves an initial "guess" (mass-size) distribution sequentially with each of the stage kernels, compares the resultant calculated stage mass with the measured stage mass, and adjusts the input "guess" distribution to make the calculated and measured stage masses agree. The stage kernel function was used in each case as the adjustment function, so the overall effect of the procedure was to construct a smooth input distribution from a linear combination of the kernel functions. The inversion was constrained to conserve total mass. The robustness of the inversion procedure is presented in [27].

The concentrations of elemental carbon (EC), organic carbon (OC) and water-soluble organic carbon (WSOC) were determined from samples collected using a NOAA impactor [28]. The impactor was operated at a flow rate of 30 L/min so that PM1 was collected on a 47 mm quartz fibre filter. A gas meter was attached to the outlet of the sample pump to determine the total sample volume.

4.1.2 Analytical Methods

Gravimetric mass on the MOUDI filters was determined using a Mettler UMT2 ultra-microbalance with a specialised filter pan. Electrostatic charging was reduced by the presence of radioactive static discharge sources within the balance chamber. The resolution of the balance is 0.1 μg. Various experiments confirmed that the uncertainty per measurement was on the order of 6 μg, which for a MOUDI sample of 12 filters results in a conservative propagated uncertainty of ~ 6% in the summed mass. Filters were weighed both before and after exposure at 20% RH.

Ion chromatography (IC) was used to measure soluble ions in aqueous extracts of the MOUDI filter samples. Portions of the filters were extracted in 12 mL of Milli-Q HPLC grade (high purity de-ionised) water and a bactericide (120 μL of chloroform) was added to preserve the extracted sample from biological degradation after extraction. The ions (Na^+, NH_4^+, K^+, Mg^{2+}, Ca^{2+}, Cl^-, NO_3^-, SO_4^{2-}, Br^-, NO_2^-, PO_4^{3-}, F^-, acetate, formate, oxalate and methane sulfonic acid (MSA)) were determined using a Dionex

DX500 gradient ion chromatograph employing Dionex IC columns (AS11 column and ARS1 suppressor for anions, CS12 column and CRS1 suppressor for cations). Quality assurance procedures include blind duplicate analysis, routine analysis of WMO standards and ion balances that meet USEPA acceptable criteria [29]. Details of these procedures can be found in [27].

Nuclear methods, primarily proton induced x-ray emission (PIXE) and instrumental neutron activation analysis (INAA), were used to analyse the elements H, F, Na, Al, Si, P, S, Cl, K, Ca, Ti, V, Cr, Mn, Fe, Cu, Co, Ni, Zn, Br, Pb. These measurements were carried out at the University of Gent.

The total carbon (TC), organic carbon (OC), and apparent elemental carbon (EC_a) contents of the quartz filter samples were measured by the thermal-optical transmission (TOT) technique of [30], using the procedure described for laboratory #11 in [31]. This involved stepwise combustion of the aerosol carbon to form CO_2, which was then reduced to methane and detected by a flame ionisation detector. With TOT the effects of charring during pyrolysis of organic compounds in the early stages of the combustion (artifact EC_a) are taken into account. Simultaneous monitoring of light transmission through the filter allows definition of EC_a as carbon that evolves after the light transmittance through the sample had reached its original level.

The WSOC content of the quartz filter samples was determined by analysing aqueous extracts of the samples with a Shimadzu TOC 5000A liquid analyser. The detector response was calibrated with standard solutions of potassium hydrogen phthalate provided by Shimadzu. In addition to the direct determination of the dissolved carbon content, the water extracts were also analysed after removal of the inorganic carbon (by acidification with HCl to pH 2, followed by 5-min sparging).

The main function of the size dependent chemical data is to derive size-dependent particle density and refractive index information (Section 4.3).

4.1.3 Observations

Mass Concentration

Figure 6 shows average concentrations for PM10, PM2.5 and PM1 at Jabiru, derived from the MOUDI for the June and September sampling campaigns. The June data show a wide range in concentrations. In particular, the sample collected on June 24th displayed very high concentrations, and field observations noted the presence of extensive fires north and northeast of the sampling site. While it is interesting to investigate the characteristics of these samples, since they pertain to a fresh smoke source, the data for June 24th are not included in averages to determine the typical composition for the sample periods. In addition, the sample collected on June 25th revealed very low concentrations. While this was the only MOUDI sample collected on aluminium foils, both the MOUDI and NOAA impactors sampled low concentrations on that day, suggesting that this is a valid sample.

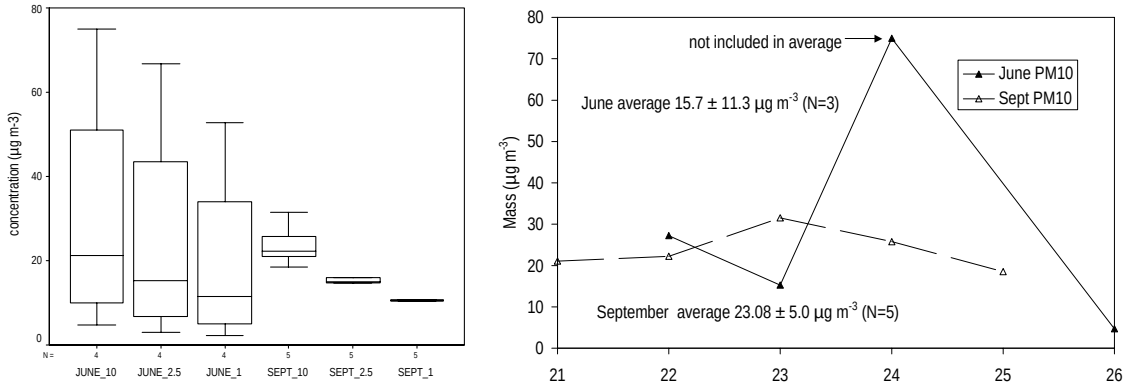

Figure 6: Box plot showing the median, quartiles, and extreme values. The box represents the interquartile range, which contains the 50% of values. The whiskers are lines that extend from the box to the highest and lowest values, excluding outliers. The line across the box indicates the median. The second figure shows the time series of PM10 at Jabiru determined from the MOUDI samples.

Figure 6 shows the time series for PM10 determined from the MOUDI for the June and September campaigns. The September samples showed less variation in concentration.

Size Distributions

The averaged mass size distributions determined from the MOUDI samples are shown in Figure 7. Both averaged distributions suggest the presence of two major modes; a coarse mode centred at a diameter of around 8 µm, and a fine mode at around 0.5 µm, separated by a dip in the distribution at around 2µm diameter. A third smaller mode may be inferred at around 0.1 µm diameter. The chemical composition of these modes gives information about the source of the contributing particles. The coarse mode is made up of refractive species such as Na, Cl, Mg and Ca which are derived from sources that produce aerosol by mechanical processes, such as bubble-bursting at the ocean surface (to give the seasalt constituents Na, Cl and Mg) and erosion at the earths surface to produce soil components such as Mg, Ca, Fe, Si and Al (Figure 8). As these constituents are emitted as aerosol directly into the atmosphere and the aerosol has not undergone any chemical reactions in the process of forming aerosol, they are considered primary aerosol. The fine mode particles are dominated by primary aerosol produced by combustion as well as secondary aerosol, which is produced by the partitioning of gas phase constituents to the particle phase. The combustion of plant biomass can be traced by the presence of non-seasalt potassium (nssK) in the fine particle mode (Figure 8), and the presence of elemental carbon. The secondary aerosol can be traced by the presence of non-seasalt sulfate ($nssSO_4$) in the fine mode (Figure 8), produced by the oxidation of SO_2 in the gas phase, to form sulfuric acid which has a low volatility and is able to readily partition to the particle phase. The presence of NH_4 in this fine mode represents the neutralization of the strong sulfuric acid in these particles (Figure 8). The presence of NO_3 in the coarse mode particles also represents

neutralization (Figure 8), with the weak acid produced from the oxidation of NO_2 (most likely produced by combustion) neutralizing the weakly alkaline seasalt aerosol made up substantially of Na and Cl.

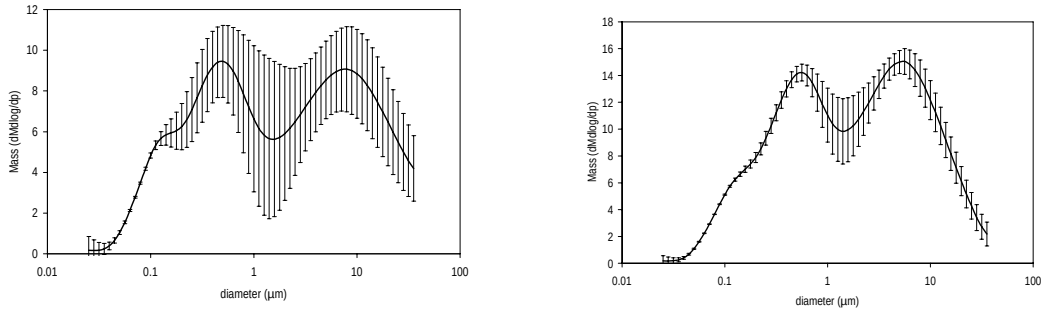

Figure 7: Averaged mass size distributions for June (left) and September 2003. Mass units are μg /m³ and error bars represent 1 standard deviation about the mean. N=3 and N=5 respectively (note that the sample collected on June 24 is not included in the average).

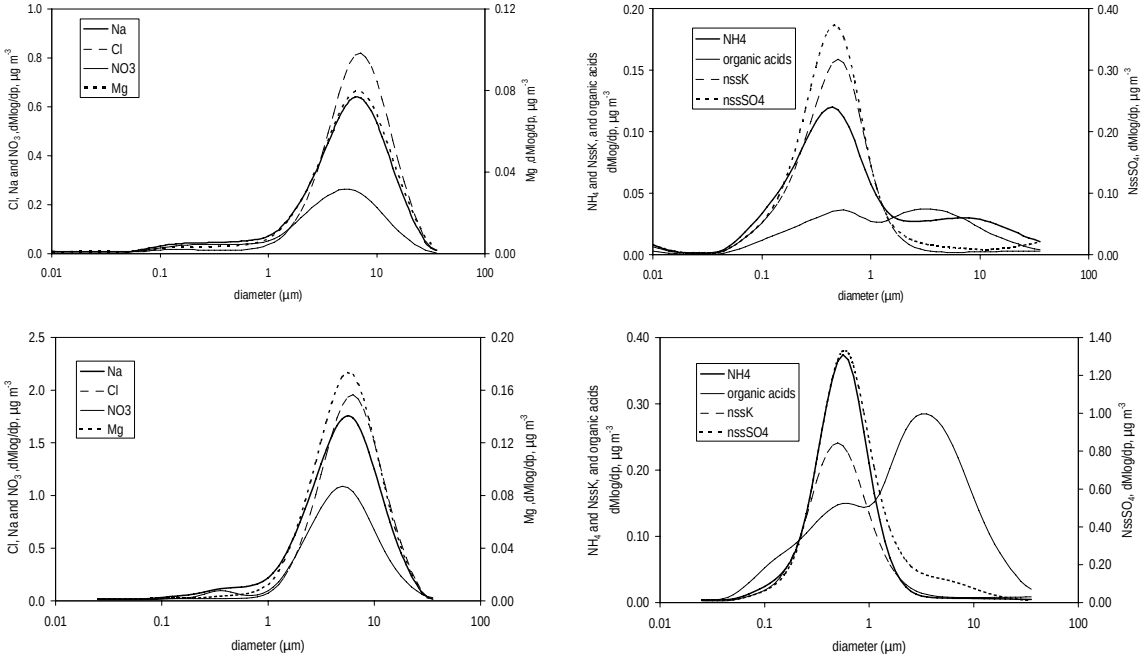

Figure 8: The first figure shows the averaged mass size distributions of Na, Cl and Mg, species derived from seasalt or soil dust through mechanical process such as bubble-bursting and erosion, and NO_3, derived from the oxidation of NO_2, for June (upper plots) and September 2003 (lower plots). The right hand panels show the averaged mass size distributions of nssK, produced during combustion, $nssSO_4$, produced during oxidation of gaseous SO_2, NH_4 (which neutralizes the strong sulfuric acid aerosol) and organic acid

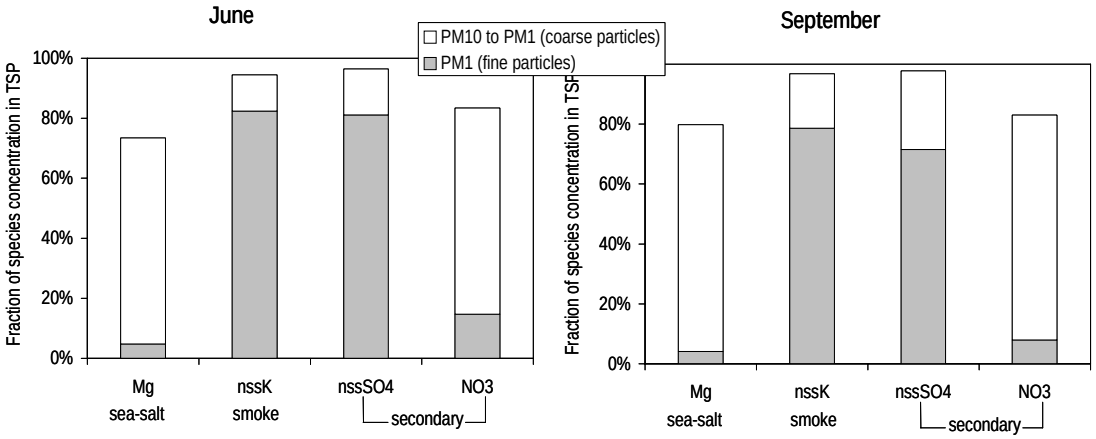

Figure 9: Fraction of concentration of marker species of the TSP concentration found in the coarse and fine particles.

Assuming the following markers for different sources, it is possible to assess the contribution of each source to different size fractions of the particle mass. The marker for seasalt is Mg, the marker for woodsmoke is nssK, and $nssSO_4$ and NO_3 are markers for secondary inorganic particle production. Figure 9 shows the contribution of each of these sources to the coarse (PM10 to PM1) and fine (PM1) particles for the June and September campaigns. As demonstrated qualitatively in the size distributions in Figure 8, the sea-salt marker Mg is predominately found in the coarse mode particles, while the smoke marker is predominately found in the fine particles. The secondary inorganic marker $nssSO_4$ is predominately found in the fine particle mode, while NO_3 is predominately found in the coarse particle mode.

Mass Balance: PM1

A mass balance can be performed using the organic composition data determined from the NOAA impactor and the PM1 inorganic composition data and gravimetric mass determined from the MOUDI. For both June and September, the averaged PM1 was comprised predominately of organic mass (OM), and the unmeasured residual fraction comprised the next significant fraction of the PM (Figure 10). The OM fraction of the PM1 was marginally larger during the September campaign, while the residual unexplained mass fraction was slightly larger during the June campaign. Elemental carbon (EC) and inorganic mass (IM) were similar for both campaigns.

The total carbon was dominated by WSOC species during both campaigns; these were more abundant during the June campaign (Figure 11). The insoluble organic carbon species fraction (WIOC) was greater in the June campaign than during the September campaign, whilst EC was relatively constant, at a few percent, across the two campaign

periods. Carbon measurements have a typical precision of around 10% although inter-laboratory comparisons of absolute concentration, particularly EC, may vary by a factor of two or more.

The predominance of WSOC in the organic fraction is reinforced by the IM composition, which had a large organic acid component (Figure 12), with the June campaign showing a greater organic acids fraction than the September campaign. IM during both campaigns was dominated by $nssSO_4$, with the fraction of $nssSO_4$ being greater during the September campaign. The woodsmoke tracer, nssK, and seasalt also made up a significant fraction of the IM for both campaigns, being greater during the June campaign. Both NO_3 and NH_4 were constant across both campaigns.

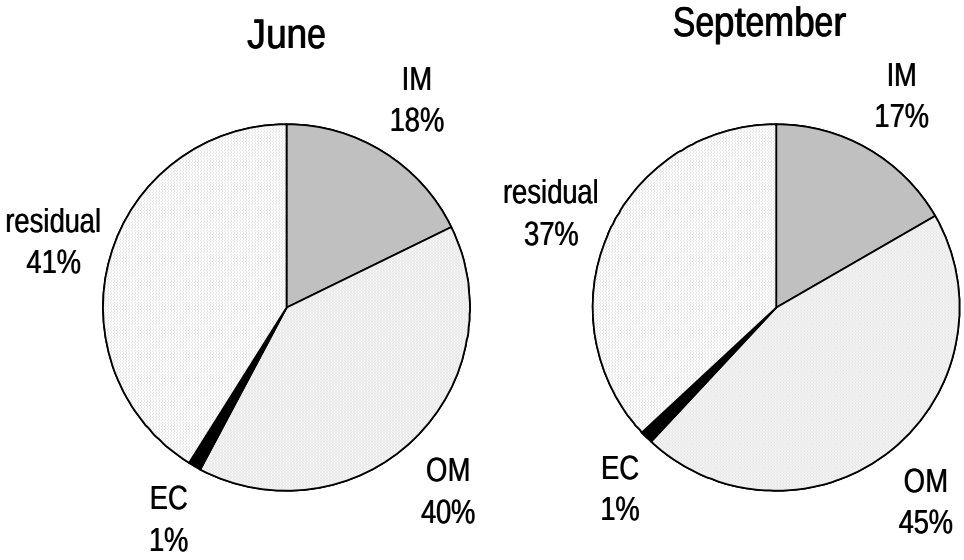

Figure 10: Pie chart showing division of PM1 (determined from the MOUDI samples) into IM (determined from the MOUDI), OM and EC (determined from the NOAA impactor samples) *and residual (determined as the difference between PM1 and the sum of IM, OM and EC).*

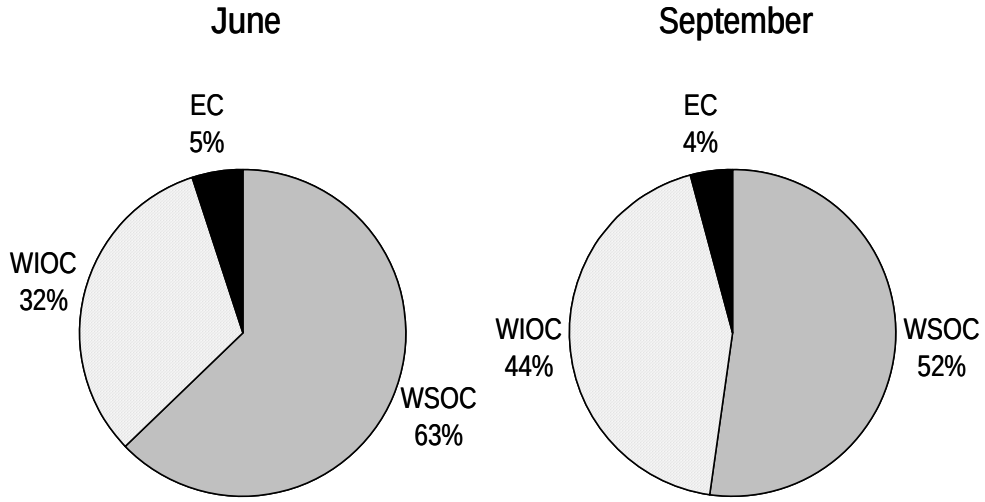

Figure 11: Pie chart showing the division of PM1 total carbon into WSOC, WIOC and EC (determined from the NOAA impactor samples).

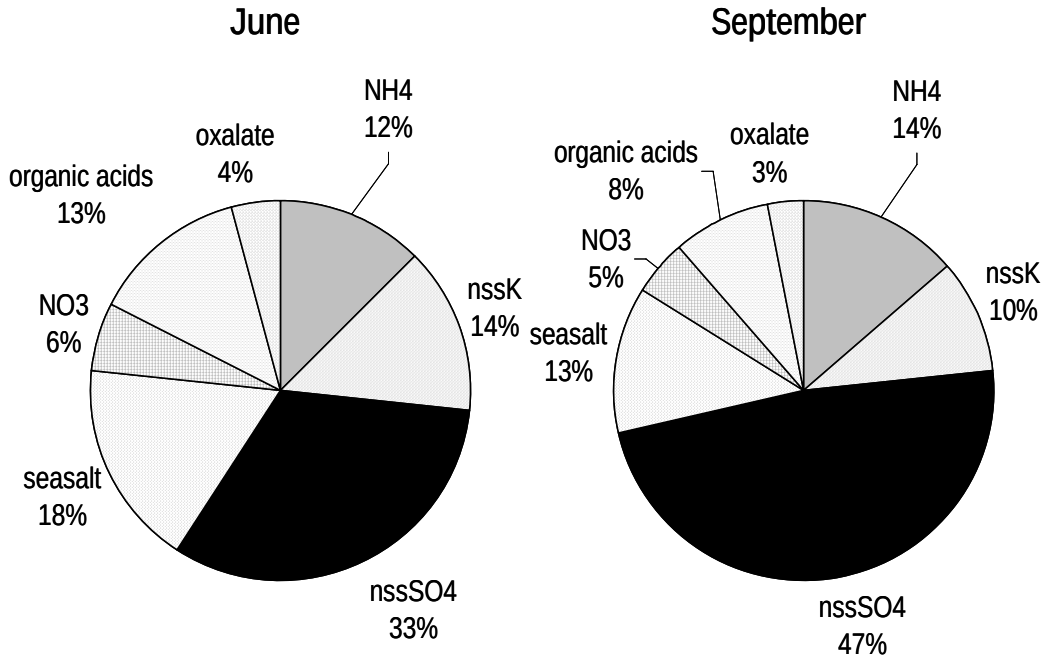

Figure 12: Pie chart showing the division of PM1 IM into its principle constituents, including the light organic acids (formic acid and acetic acid (determined from the MOUDI samples), NH_4, NO_3 and oxalate (determined from the MOUDI samples) nssK and $nssSO_4$ (determined from the MOUDI samples using Mg as the seasalt marker) and seasalt components (sum of Na, Cl, Mg, Ca, seasalt SO_4 and seasalt K).

June 24th 2003

The sample collected on June 24th 2003 was severely impacted by local fires, burning approximately to the north and northeast of the sampling site. This is shown in the mass size distribution, where the fine fraction mode has a higher amplitude than the coarse fraction mode (Figure 13). In this sample the fraction of mass made up of OM is twice that seen for the average June and September samples (Figure 7). In addition, the contribution of EC to the mass of this sample is twice that seen for the average. The smoke tracer, nssK makes up 42% of the IM mass (compared with 10-15% for the average samples). The fraction of mass made up of oxalate is also higher in the sample collected on June 24th. Finally, nssSO_4 makes up only a small fraction of the PM1 IM for the June 24th sample.

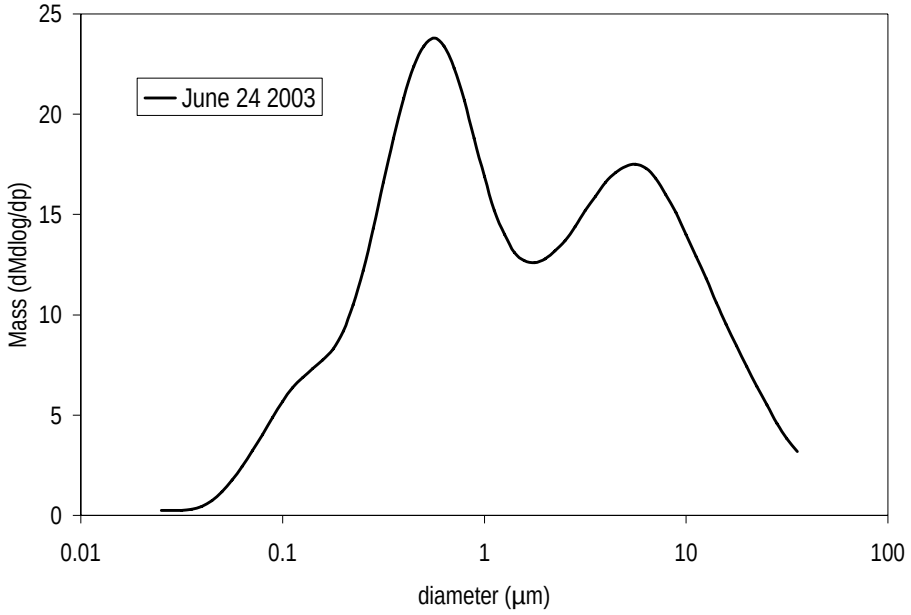

Figure 13: Mass size distributions for sample collected on June 24 2003, when the ground-based site was impacted by local smoke (mass units are μg /m³).

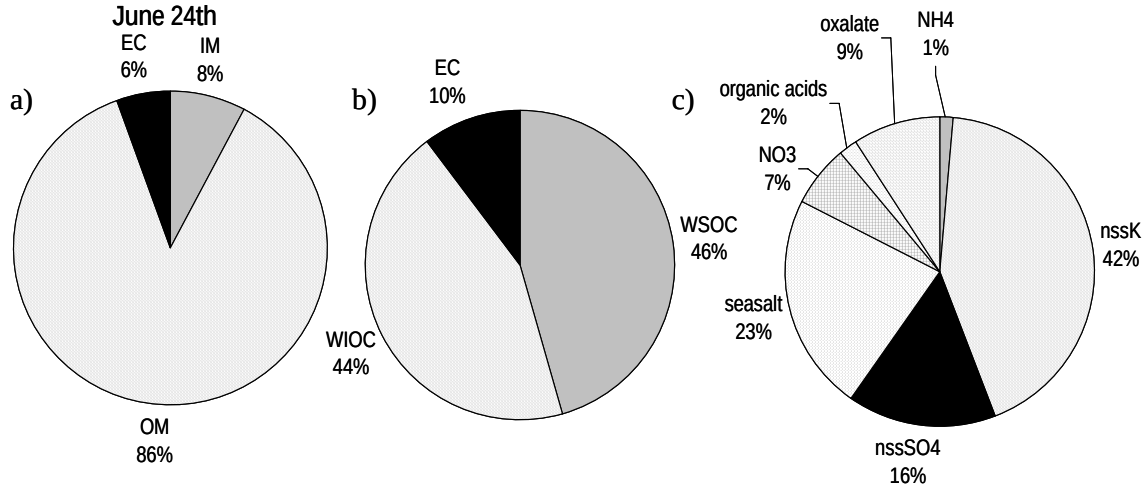

Figure 14: Pie chart showing a) the division of PM1 (determined from the MOUDI samples) into IM (determined from the MOUDI), OM and EC (determined from the NOAA impactor samples) and residual (determined as the difference between PM1 and the sum of IM, OM and EC; b) the division of PM1 total carbon into WSOC, WIOC and EC (determined from the NOAA impactor samples); and c) the division of IM into organic acids (the sum of formic acid and acetic acid determined from the MOUDI samples), NH_4, NO_3 and oxalate (determined from the MOUDI samples) nssK and nssSO_4 (determined from the MOUDI samples using Mg as the seasalt marker) and seasalt components (sum of Na, Cl, Mg, Ca, seasalt SO_4 and seasalt K).

Summary

Analysis of the nine samples collected during two campaigns at Jabiru in 2003 shows a spectrum of biomass smoke influences on the aerosol chemistry. The June 24th sample was severely impacted by local smoke, and shows very high OM loadings. Similarly the nssK and oxalate concentrations are high in this sample.

The average June and September samples show less smoke influence. OM and nssSO_4 were greater in the September period, indicating stronger secondary particle production during the September campaign, including both inorganic and secondary organic components. Slightly greater nssK, oxalate and organic acid concentrations during the June campaign, suggest that these samples may have been more strongly influenced by smoke than the September campaign.

Comments

Care needs to be exercised in using the Jabiru measurements to make a general conclusion about the boundary layer aerosol. In particular local sources need to be accounted for and their effect on the results interpreted appropriately as has been done above. Using the samples that were collected when the effect of these fires had diminished is more likely to accurately reflect the boundary layer aerosol concentration

other than when travelling through a plume or very close to a fire or fires. The absence of fires near Jabiru in September means that these measurements are more appropriate to use in making general conclusions about the boundary layer aerosol chemical composition. Chemical composition samples, size distribution measurements and scattering coefficient data all reflect more uniform aerosol at Jabiru during September.

The analysis in section 6.2 reveals that the chemistry data in September was affected by the prevailing wind conditions resulting in the observed diurnal variation in both the coarse and fine mode number concentrations. These shifting wind directions resulted in the 24-hr mass samples being influenced by fires to the north and northeast of Jabiru and elevated seasalt concentrations due to strong northerly and northeasterly winds over night. Other than for the morning flights, the aircraft samples will have experienced less exposure to those aerosol sources.

4.2 Aircraft Chemistry Measurements

The flow rate for the chemical mass sampler on the aircraft was limited to around 15-20 L/min ambient by the overall flow capacity of the isokinetic sampling system. Combined with the low ambient loadings on all flights this resulted in a very small amount of mass being collected.

Aerosol mass was determined gravimetrically at low relative humidity, from samples collected on PTFE membrane filters. Typical uncertainty in absolute aerosol masses analysed this way is around ± 3 μg and the two blank filters gave values consistent with this level of uncertainty (-3 μg and -5 μg). Mass loadings were lower in June than September and lower in the upper tropospheric samples than those in the lower troposphere (altitude < 2.5 km). For June, individual mass loadings in the upper troposphere were 1.9 ± 0.4 μg m^{-3} and 3.3 ± 0.6 μg m^{-3} (a third sample with 14.9 ± 3.5 μg m^{-3} was rejected as an outlier with a low flow volume). In September the upper troposphere concentrations were found to be 1.3 ± 0.3 μg m^{-3}, 1.3 ± 0.4 μg m^{-3} and 5.6 ± 0.4 μg m^{-3}. For the lower troposphere samples (non transit flights) in June the loadings were 6.7 ± 0.8 μg m^{-3} and 9.4 ± 2 μg m^{-3}. Corresponding loadings for September were 5.1 ± 0.6 μg m^{-3} and 8.7 ± 0.5 μg m^{-3}. In all cases the uncertainty range indicated refers to a ± 1 σ value of 3 μg on the collected mass.

The soluble aerosol composition was determined in aqueous extracts using high-sensitivity ion chromatography (as described above in Section 4.1.2). Composition was similar in both altitude ranges and in both sampling periods (June and September), being consistent with three principal components, sea-salt, smoke and $nssSO_4$ in varying amounts. The most obvious difference in composition between June and September samples is the much stronger contribution from $nssSO_4$ in the September samples.
Approximate volume weighted compositions for nssK (the smoke tracer), $nssSO_4$ and sea-salt for the two altitude ranges are shown below in Table 7.

Table 7: Volume weighted composition

Campaign	*Altitude*	*nssK* (ng/m^3)	*nssSO_4* (ng/m^3)	*Seasalt* (ng/m^3)
June 03	Low	56	72	428
	High	2	45	297
Sept 03	Low	63	483	223
	High	19	217	81

Particles were also collected by impaction on electron microscope grids on the June flights for analysis by electron microscopy. These samples were analysed at the Meteorological Research Institute in Tsukuba Japan (Dr. K. Okada). The single particle analyses, of the sub-micrometre fraction, show that particles collected in the upper troposphere were consistent with sulfuric acid morphology. Further EDAX analyses of selected particles may be desirable to quantify other components in these particles.

4.3 Determination of Refractive Index and Particle Density

This section describes the procedures that were used to determine the refractive index and density of particles in three broad altitude ranges: the free troposphere (FT), the upper boundary layer (UB) and the lower boundary layer (LB). The thermodynamic model SCAPE 2 [32] was used to estimate the state and composition of atmospheric inorganic species as distributed between the gas and aerosol phases. The model characterises the chemistry of the ambient aerosol as a function of relative humidity (RH) so that the water mass associated with the particles can be determined by calculating the water activity of the mixed electrolyte solution. Output from this model, specifically the molar fractions of the modelled chemical composition, together with elemental carbon and organic carbon concentrations, were used to calculate the refractive index and density of the aerosol.

Aerosol samples were collected on board the aircraft with a filter sampler that divided the atmosphere into two altitude ranges, less than 2.5 km, or broadly the boundary layer, and the free troposphere (> 2.5 km). This altitude division was selected because sample flow rate on the aircraft was limited by the total instrument configuration and capacity of the isokinetic inlet, and the aerosol loading was expected to be relatively low at higher altitudes. Sampling was started and finished manually soon after take-off and just before landing, whilst the altitude changeover was carried out automatically, based on ambient air pressure.

SCAPE2 requires the following chemical species as input data; sulfate, nitrate, ammonium, sodium, chloride, potassium, calcium, magnesium and carbonate. Except for carbonate, all these species were measured in samples collected on the aircraft. The carbonate concentration was determined by calculating the acidity (as hydrogen concentration) associated with sulfate, nitrate, formate, acetate and oxalate and assuming excess hydrogen ion concentration is associated with bicarbonate. Ambient RH and temperature were determined from the wet bulb/dry bulb measurements on board the aircraft.

An averaged SCAPE input chemical composition was determined for the June and September campaigns for each of the atmospheric levels (FT, UB and LB) from the aircraft aerosol samples (Table 8). Also shown in Table 8 are the EC concentrations (determined using the CSIRO Absorption Photometer) and the OM concentrations (determined by the difference between gravimetric mass and the sum of the inorganic mass elemental carbon concentration)

Table 8: Scape2 input data for June & September campaign. Note that the UB and LB chemistries are the same. This is due to the fact that the aerosol samples were collected from above and below 2.5 km.

JUNE	Temp	RH	Na	SO_4	NH_3	NO_3	Cl	K	Ca	Mg	Carbonate	EC	OM
	(K)		($\mu g\ m^{-3}$)										
FT_coarse	281.2	0.300	0.371	0.022	0.007	0.093	0.315	0.001	0.006	0.006	0.018	0.001	2.46
FT_fine	281.2	0.300	0.048	0.038	0.018	0.021	0.015	0.005	0.003	0.001	0.022	0.025	1.63
UB_coarse	293.7	0.389	0.844	0.059	0.021	0.401	1.265	0.015	0.013	0.021	0.020	0.006	4.60
UB-fine	293.7	0.389	0.110	0.105	0.054	0.090	0.060	0.066	0.007	0.002	0.025	0.105	3.05
LB-coarse	293.7	0.389	0.844	0.059	0.021	0.401	1.265	0.015	0.013	0.021	0.020	0.006	4.60
LB-fine	293.7	0.389	0.110	0.105	0.054	0.090	0.060	0.066	0.007	0.002	0.025	0.105	3.05
SEPT	Temp	RH	Na	SO_4	NH_3	NO_3	Cl	K	Ca	Mg	Carbonate	EC	OM
	(K)		($\mu g\ m^{-3}$)										
FT_coarse	278.2	0.187	0.297	0.136	0.010	0.138	0.241	0.010	0.241	0.034	0.231	0.008	0.75
FT_fine	278.2	0.187	0.032	0.249	0.098	0.013	0.009	0.024	0.009	0.002	0.288	0.149	0.77
UB_coarse	296.1	0.485	1.173	0.505	0.031	0.581	1.062	0.048	1.062	0.196	0.040	0.024	5.08
UB-fine	296.1	0.485	0.127	0.923	0.319	0.057	0.038	0.117	0.038	0.011	0.050	0.453	5.22
LB-coarse	296.1	0.485	1.173	0.505	0.031	0.581	1.062	0.048	1.062	0.196	0.040	0.024	5.08
LB-fine	296.1	0.485	0.127	0.923	0.319	0.057	0.038	0.117	0.038	0.011	0.050	0.453	5.22

The aircraft filter sampler operated through the isokinetic inlet via a sample line of around 2 m length and with several long 90° bends. No specific size selective stages were included ahead of the sampler however transmission efficiency for diameters greater than around 1 μm is expected to be low, with this sampler primarily reflecting fine mode composition. In order to account for the coarse mode chemical composition in the SCAPE2 modelling, a coarse mode composition was based on the MOUDI chemical size distributions determined on the ground at Jabiru for each campaign, together with the coarse mode tracers determined on the aircraft. This used the ratios

of SCAPE2 input chemistry data in the coarse and fine modes measured in averaged MOUDI distributions for the June and September sampling periods (Figure 7) and the concentration of the species in the aircraft chemistry samples, giving the coarse mode SCAPE2 input concentrations shown in Table 8.

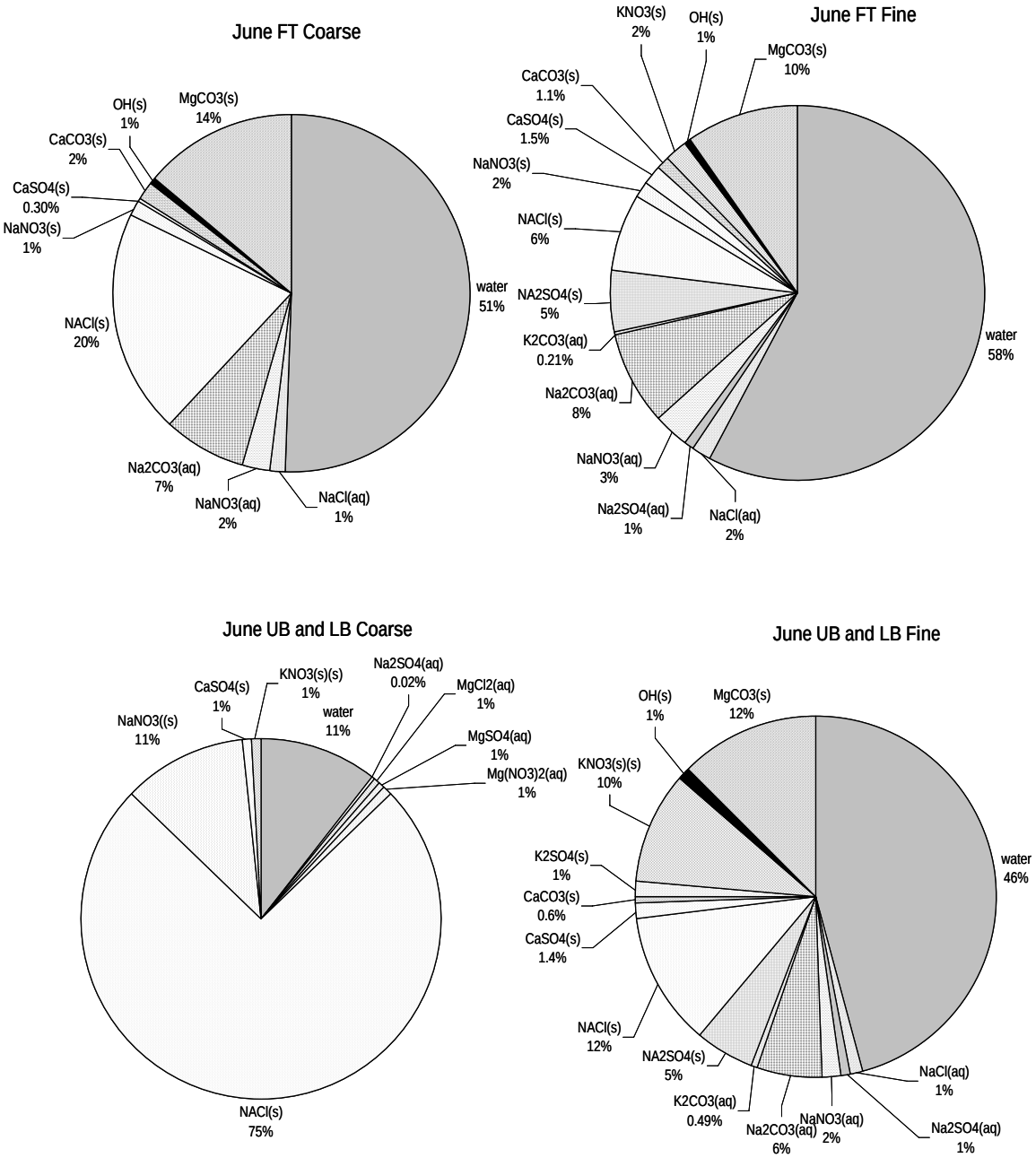

Figure 15: The modeled compositions of the coarse and fine modes for each of the atmospheric levels for June. Water makes up a significant portion of the June coarse and fine aerosol in the FT, and is a significant proportion of the fine UB and LB aerosol. However, in the coarse UB and LB aerosol the composition is dominated by NaCl in the solid phase.

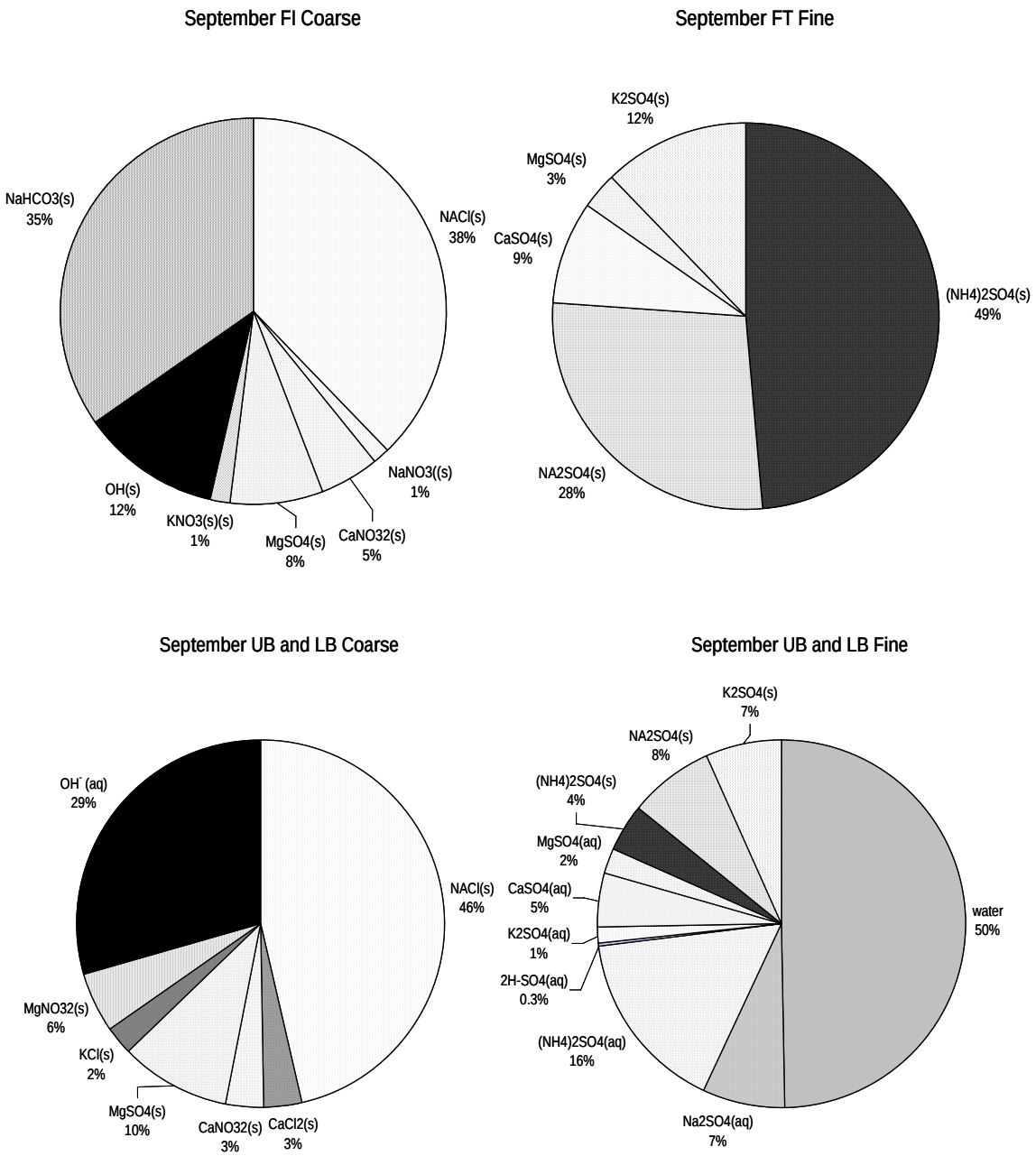

Figure 16: Modelled compositions of the coarse and fine modes for each of the atmospheric levels for September. Water is absent from the FT coarse and fine aerosol (which had a very low RH), and is only significant in the fine UB and LB aerosol.

NaCl and carbonate species dominate the solid and aqueous phases of the June FT coarse aerosol. This is also the case for the June FT fine aerosol, with the addition of sodium sulphate species in both the solid and aqueous phases. The June UB and LB coarse aerosol modes are dominated by NaCl in the solid phase, with some $NaNO_3$

(representing the volatilization of Cl from sea salt during reaction with atmospheric HNO_3). The aqueous phase is minor, dominated by sulphate and nitrate species. The June UB and LB fine aerosol shows the solid phase dominated equally by NaCl, $MgCO_3$ and KNO_3. Less abundant sulphate species are again Na and K. The aqueous phase species are dominated by carbonates.

Aqueous species are absent from the September coarse and fine FT aerosol. For the coarse aerosol, NaCl and $NaHCO_3$ dominate, and the fine aerosol is exclusively made up of sulphate species. The aqueous phase of September coarse UB and LB aerosol is dominated by OH-, while most of the mass is dominated by NaCl and nitrate species in the solid phase. The fine September UB and LB aerosol is dominated by aqueous species, which are exclusively sulphate compounds.

The refractive index (at mid-visible wavelength) and density were calculated using the results on the compounds present in the aerosol generated by SCAPE2. The refractive index of a mixture can be determined by summing the partial molar refractivities for the individual compounds making up the mixture. Similarly, from the density of the individual species output by SCAPE, the density of the aerosol can be determined. The refractive index and density of the coarse and fine aerosol from the different atmospheric levels for the June and September campaigns are listed in Table 9. These densities may be used, for example, to correct from aerodynamic to physical diameter. Refractive index is required for calculation of the aerosol optical properties in conjunction with the physical size distributions and conversely for correcting optically-derived sizes determined using light-scattering based size spectrometers (e.g. ASASP and FSSP).

Table 9: Density and refractive index estimated for the coarse and fine particles from the different atmospheric levels for the June and September campaigns.

	density	Refractive Index	
	g cm^{-3}	real	imaginary
	June		
FT coarse	1.54	1.542	-0.00004
FT fine	1.43	1.548	-0.00107
UB and LB coarse	1.50	1.549	-0.00008
UB and LB fine	1.45	1.550	-0.00236
	September		
FT coarse	1.60	1.542	-0.0005
FT fine	1.48	1.558	-0.0106
UB and LB coarse	1.49	1.546	-0.0003
UB and LB fine	1.46	1.552	-0.0054

5. Number Concentration and Particle Size Distributions

5.1 Introduction

Particle size distributions are fundamental to characterising the aerosol, and correspondingly, collection of physical size distribution data was a major component of the study. Four sizing instruments were used, two external probes (ASASP and FSSP), an APS and an SMPS. The range of instruments offered redundancy over parts of the size spectrum and in theory allows for measurement of the complete size distribution from around 0.01 μm to around 40 μm. In practice the small coarse mode concentration aloft and the limitations of the sampling instruments lowers this upper limit. Corrections for some sampling artefacts are not included. In particular the external probes have not been corrected to take account of differences between the ambient refractive index and that of the calibrating particles, although, as shown in Table 9, calculated values of the real part are typically around 1.55, with a very small imaginary (absorbing) component. This is quite close to the refractive index of the polystyrene calibration particles (1.59); hence corrections will be small, for example, with the ASASP. Even so, some differences can still be expected between measurements made using different physical attributes of the aerosol and the use of data from multiple instruments, particularly where there are overlapping ranges, can reveal potential sampling issues for the different instruments and sampling configurations. Overall this provides a much higher degree of confidence in the derivation of the physical properties than can be achieved using a single instrument and sampling configuration.

The SMPS sample rate was 150 seconds. APS samples were predominantly of 30 second duration and the external probes were sampling continuously at a 1 second rate with data reported in 1 minute integrals. Analysis of the APS and ASASP individual flight legs show a similar response to concentration changes along the horizontal for periodicities greater than the APS sampling rate (30 seconds). The agreement is weaker for the SMPS data due to the longer sampling time. Sampling for the APS and SMPS was initiated at the commencement of each flight leg, but because of the different sample durations and the time required for the SMPS to stabilize for each new altitude, the samples are not completely synchronised. Flight leg averages include all samples taken over that particular leg. ASASP and FSSP start and end times for flight leg averages were chosen to be consistent with the APS start and end times. Any events that were observed in one instrument and not in another (such as a smoke plume) were noted. This could occur for example if there was a delay in the commencement of sampling, which occurs for the SMPS due to a delay in pressure stabilization. Aerosol concentrations usually remained relatively uniform along most flight legs, with the obvious exception of local fire plumes or spatial gradients in concentration due to the non uniform distribution of fires. The altitude distribution of concentration was relatively uniform in the haze layer and the FT. Typically a decrease was observed in

concentration in the upper boundary layer region and for some flights this was close to an exponential decrease with increasing altitude (Flight 3 in September).

Amalgamating flight legs over defined altitude regions increases the number of particles in each average distribution thus reducing statistical uncertainty. This is particularly important for the large particle (super-micrometre) part of the spectrum where concentrations are low. Three regions were considered: the lower boundary (LB) layer (or haze layer), the upper boundary (UB) layer and the free troposphere (FT). This analysis is consistent with the chemistry data in Chapter 4. Overall averages for each region were obtained by averaging over flights, giving three average size distributions for each campaign. These campaign averages are presented below for the SMPS and APS and for the combined size distributions, which include the ASASP and FSSP.

Table 10: Altitude regions considered in calculating campaign averages. The flight legs that are included in each regional average are shown for each flight. Units are in km.

Campaign	*Flight #*	*LB*	*UB*	*FT*
June	1	0.61, 0.91, 1.37		1.83, 2.44
	2	0.76, 1.68		3.05, 4.57, 6.1
	3	0.46, 0.76, 1.07, 1.37		1.68, 1.98, 2.29
	4	0.46	0.76, 1.37	1.98, 3.05, 4.57
September	1	0.61, 1.22, 1.52, 1.83		6.1
	2	0.46, 0.76	1.83, 2.44, 3.05	
	3	0.46, 0.76	1.83, 2.44, 3.05	4.57, 6.1
	4	0.46, 0.91, 1.22, 1.83	2.44, 3.05	

For the September flights the differences observed between number concentration and size distributions made it straightforward to assign flight legs to the BL and FT. The APS showed a significant drop in the coarse mode concentration in the FT and the shape of the size distribution derived using the SMPS changed markedly between the BL and FT. Assignment of flight leg distributions to the LB and UB regions was based primarily on differences in concentration. The shape of the coarse mode size distribution remained relatively constant through the entire boundary layer depth. The same procedures were followed for the June flights, although on some occasions the distinctions were less obvious. Altitude regions defined this way corresponded quite well with the atmospheric structure indicated by the temperature and relative humidity profiles. In June, only two flight legs are considered to be part of the UB region. These flight legs are both from flight 4, a morning flight, and the aerosol was clearly stratified, as evidenced by concentration changes with altitude. Also, low concentrations of coarse mode aerosol were observed further indicating little vertical mixing. This can be compared with other flights for June where the boundary layer appears well mixed, up to boundary with the free troposphere. Flight 4 thus represents quite different atmospheric conditions to other June flights. One anomaly that can be seen in Figure 17 is that for June the concentration in the FT size distribution appears larger than that in the UB distribution. This is an

artefact resulting from different numbers of flight legs in the averages, with the FT distribution derived from just one flight (Flight 4) but the UB average from eleven flight legs encompassing all four flights. The FT distribution for flight 4 is smaller in magnitude than the corresponding UB size distribution, consistent with expectation.

Campaign averages for the different altitude regions give the best possible representation of the ambient conditions; this approach also largely removes difficulties associated with different sample cycling times for the different instruments.

5.2 Fine Mode Size Distributions

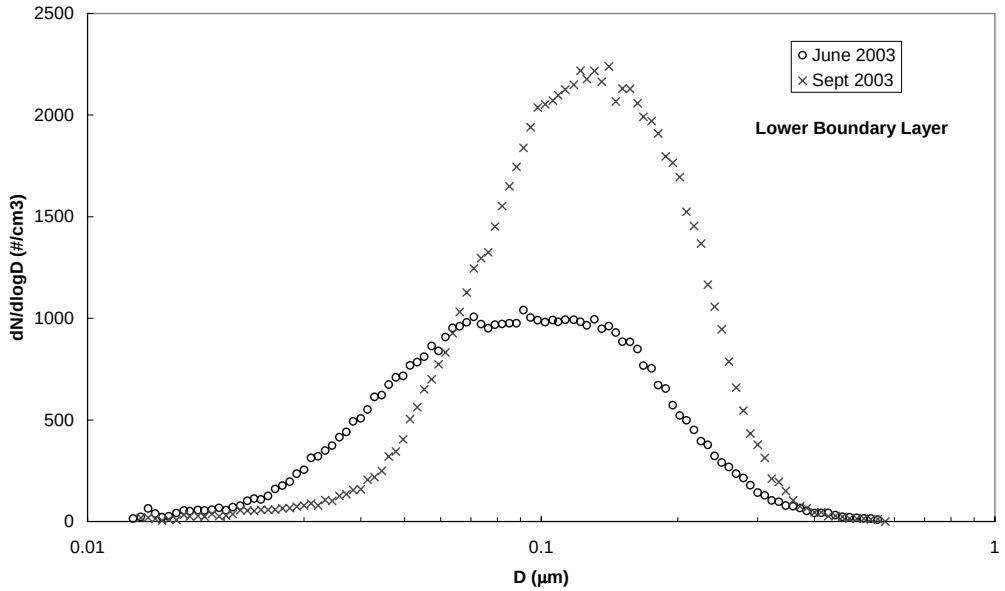

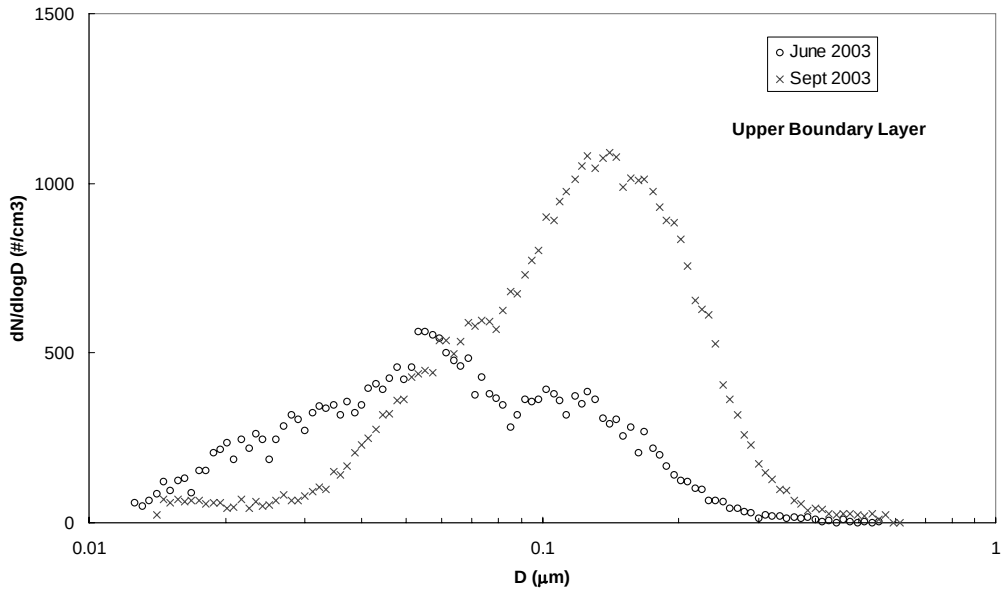

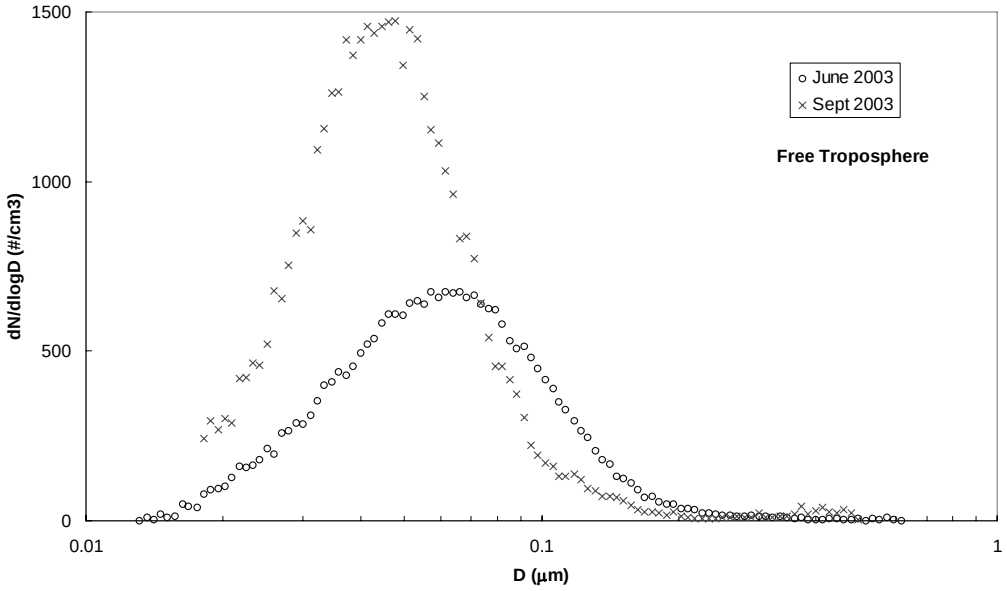

Figure 17: Average size distributions for the two different months of the campaign. These data are from the SMPS

Campaign average distributions for the aerosol fine modes are shown in Figure 17. For the June flights, large variations in particle concentrations along the flight legs were quite typical. This is attributed to the presence of localised smoke plumes that were intersected along the flight paths. This variability was also found in the sub 100 nm size range, identified here as an Aitken or possibly 'fresh smoke' mode. In September the flight paths were generally further from the fires and variability in the sub-100 nm range was also reduced.

One clear difference between the boundary layer fine particle distributions observed in June and September is the larger concentration of particles in the size mode with a mode diameter around 150 nm in September. This mode is usually identified as the accumulation mode and in these conditions is expected to be dominated by aged biomass burning smoke, which was observed to be much more abundant in the latter part of the dry season. Analysis of fine aerosol composition data for Jabiru clearly shows that at ground level this mode is predominantly carbonaceous (Section 4.1.3), and produced from the burning of biomass (in this case vegetation including savannah grasses). Reduced local visibility over wide areas and the presence of spot fires visible from the aircraft and in satellite images support the generality of the Jabiru chemical data.

Normally both size modes were present in the boundary layer size distributions but with varying concentrations. In June the modes were similar in magnitude, which is consistent with the observation of less smoke in the haze layer. In September the overall level of aged smoke was greater in the boundary layer. June is quite early in

the burning season whereas September is near the peak. The size distribution data show an appreciable change in aerosol microphysical characteristics between June and September. For the June flights the division of the boundary layer into two regions is somewhat speculative since only two flight legs qualified, hence the June upper boundary layer distribution should be considered more indicative than for than the other regions.

For June the flight leg size distribution sample deviations were larger for the Aitken mode than for the accumulation mode. This is attributed to the sampling of more fresh smoke plumes enriched in Aitken mode particles.

The observation of two fine particle modes is consistent with observations reported by Hedberg et al. [33] and Guyon et al. [34]. Whereas Guyon et al. [35] raise the possibility that this bimodal feature may be an artefact of the PCASP, the present observations, and those of Hedberg et al., both made using a mobility analyser; confirm that it is a real feature. The typical modal diameters for the present data are slightly smaller than those reported by Guyon et al.

The submicrometre size mode in the FT distributions has a typical modal diameter at around 50 nm in September and around 65 nm in June, and is slightly broader. Both values are smaller than the modal sizes observed in the boundary layer, which is indicative of largely independent sources. As shown in section 4.2, the composition of the collected aerosol in the free troposphere for both June and September was also somewhat different to that in the boundary layer, with much lower concentrations of smoke tracer (nssK) but nssSO4 levels about one half of those in the boundary layer. This implies a smaller relative contribution from primary smoke particles and larger contribution from secondary production.

Table 11: Estimated Count uncertainty at the given diameter. The fifth column contains the total number of counts recorded by the SMPS for each region. The total count (N) is the best estimate of the mean total count, from which the standard deviation is estimated assuming a Poisson distribution, $\sigma_c = \sqrt{N}$.

Campaign	Region	Diameter (μm)	Number Concentration ($\#/cm^3$)	Total Counts $\times 10^6$	Estimated Count Standard Deviation (σ_c) %
June	LB	0.05	716.267	53.29	0.014
		0.1	990.615	73.70	0.012
		0.5	18.348	1.37	0.085
	UB	0.05	422.357	5.406	0.043
		0.1	364.484	4.665	0.046
		0.5	0	0	
	FT	0.05	605.737	46.52	0.015
		0.1	450.019	34.56	0.017
		0.5	6.355	0.488	0.143
Sept	LB	0.05	404.126	29.79	0.018
		0.1	2037.484	150.20	0.008
		0.5	14.102	1.04	0.098
	UB	0.05	363.929	16.559	0.025
		0.1	802.489	36.51	0.017
		0.5	24.205	1.101	0.095
	FT	0.05	1341.701	23.82	0.020
		0.1	192.744	3.423	0.054
		0.5	4.789	0.085	0.343

As shown in Table 11, large counts were obtained with the SMPS even at the limit of the instrument's sizing capability. In general the variation between samples across a flight leg was high if there were isolated smoke plumes along the flight path or an increase in smoke concentration towards one end of the flight leg. Because the counts are high, the impact of Poisson noise is negligible for most size bins. This noise has the greatest impact for the smallest size bins in the BL and for the larger size bins in the FT, where concentrations of fine mode aerosols are lowest. In general noise was not a problem and it was possible to fit size distribution functions. The major sample variation, other than for the extreme bins, is due to changes in the concentration of smoke particles.

5.3 Coarse Mode Volume Distributions

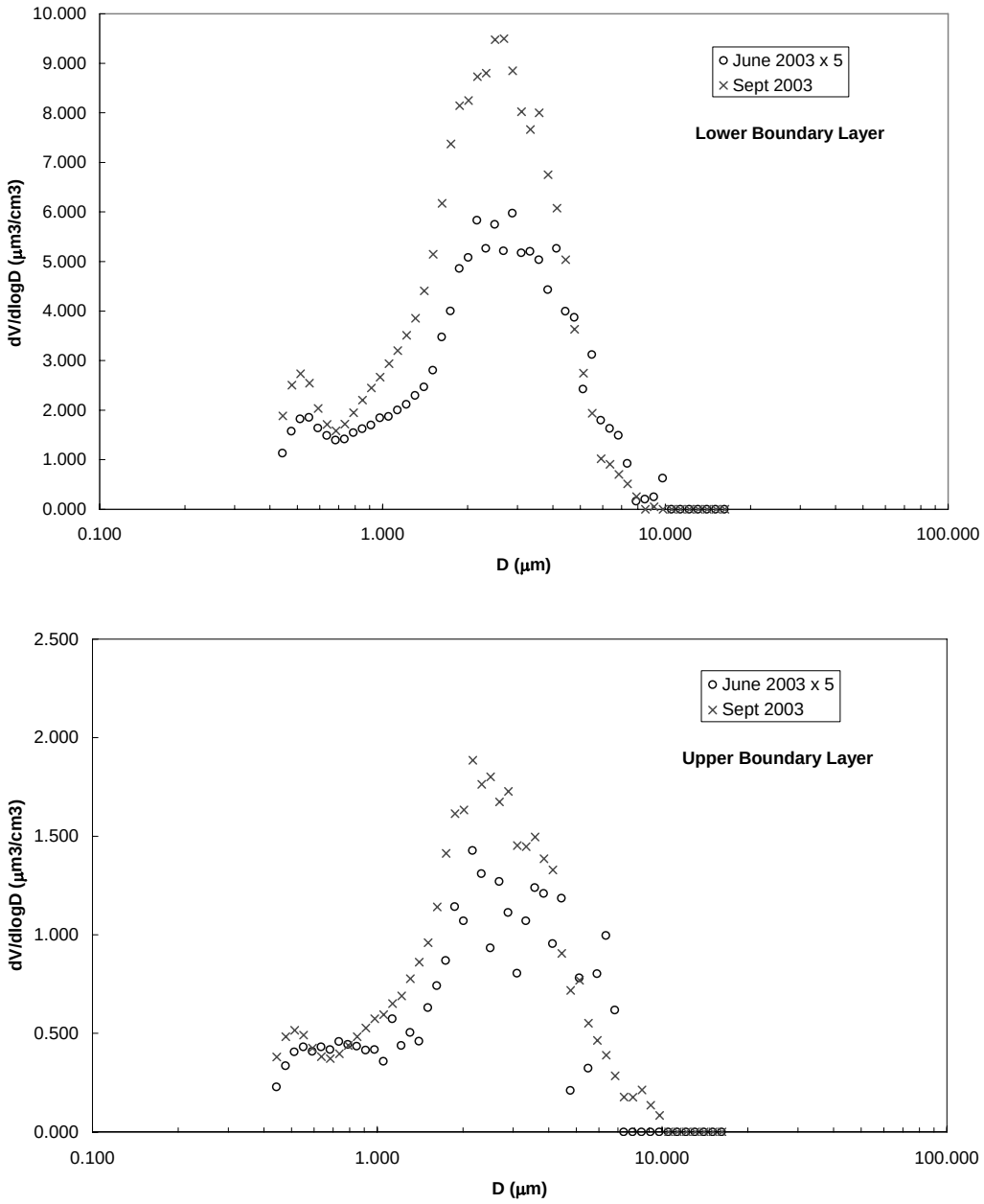

Figure 18: Average volume distributions for the two different months of the campaign. These data are from the APS.

Due to the very low concentration of coarse mode aerosol, volume distributions were calculated from the measured size distributions, making the assumption that the particles are spheres. This assumption is not accurate for all particulate species

encountered. For example, dry sea salt aerosol may be cube-like or irregular in appearance.

The volume distributions weight the number concentration by the diameter cubed and hence emphasise the coarse mode. The coarse mode particle number concentrations are very low especially for the UB distribution, even after averaging over each campaign. The number of samples that belong to the UB region per campaign is considerably less than the LB region and hence the variation in counts per bin is typically higher for this region. In the free troposphere the coarse mode is exceedingly small and hence the data tend to be noisy. For the largest particles sampling losses start to become important for the APS.

The drop in concentration for sizes less than about 0.6 μm is due to counting inefficiencies with the APS 3321. Whilst significant improvement has been made in small particle detection performance for this model and in the rejection of large particle phantoms counts it is unlikely counting efficiencies are 100%. The previous model 3320 (identical in all respects except for an improvement in signal processing) was shown to have counting efficiencies of 30% for 0.5 μm diameter particles, 100% for 0.9 μm diameter particles and 60% for 5 μm diameter particles [19]. Because the other sizing instruments are more accurate below 0.5 μm and above 5 μm it is not necessary to try to correct for these counting inefficiencies. As is evident in Figure 18, the volume distribution drops sharply for large sizes. The counts in the larger size bins very quickly fall below the detection limited of the instrument (1 count per minute). This is a result of the combination of counting inefficiency, and above 3 μm and certainly above 5 μm, to particle losses in the isokinetic inlet and sampling line. For this reason the FSSP data, once corrected for ambient refractive index and relative humidity, provide the more accurate coarse mode tail and will be preferred in this region of the size spectrum over the APS data. The APS, because of its superior sizing resolution over the probes, does provide a detailed representation of the coarse mode peak in the volume distribution. The data as displayed above should be considered most accurate in terms of shape and magnitude between about 0.6 and 5 μm and optimal between 0.9 and 3 μm.

The drop in concentration for the FT size distribution appears around 0.8 μm (not shown). The reason for this is that there is very little particulate matter in the accumulation or the coarse mode and hence the effect of the counting inefficiency shows up more strongly and becomes apparent at a larger size. This will be exacerbated if sizing corrections are applied to the FT distributions as a result of the pressure induced size shift (Section 5.3.2).

One obvious finding from the APS volume distributions was the absence of a well defined coarse mode in the FT (not displayed). This is expected as most coarse mode aerosols are generated at or near the earth's surface, requiring convective lifting without removal to reach the FT; gravitational settling is also stronger than for fine

aerosol. Large particles were not completely absent in the FT but the concentration was extremely low.

By averaging over each campaign sufficient counts can be obtained to clearly define the coarse mode. Losses can be estimated using theoretical and empirically determined relationships to take account of kinematic losses (particles can not follow the rapidly changing air flow (either in terms of magnitude or direction)). Transport losses should be small due to the short length of tubing used for the APS. The main losses would be expected at the entrance to the isokinetic inlet, entrance of the APS sub-sampling line and the APS inlet.

A final observation is that the tail end of the accumulation mode of the volume distributions for the FT (not displayed) is larger in Sept than for June.

Table 12:Estimated count uncertainty at the given diameter. The fifth column contains the total number of counts recorded by the APS for each region. The total count (N) is the best estimate of the mean total count, from which the standard deviation can be estimated assuming a Poisson distribution, $\sigma_c = \sqrt{N}$.

Campaign	Size Distribution	Diameter (μm)	Number Concentration ($\#/cm^3$)	Total Counts	Estimated Count Standard Deviation (σ_c) %
June	LB	1	0.618	154191	0.255
		3	0.067	16717	0.773
		5	0.007	1747	2.393
	UB	1	0.118	5074	1.404
		3	0.010	430	4.822
		5	0.002	86	10.783
	FT	1	0.043	10492	0.976
		3	0.003	732	3.696
		5	0.000	0	
Sept	LB	1	4.731	1135440	0.094
		3	0.509	122160	0.286
		5	0.038	9120	1.047
	UB	1	1.053	177957	0.237
		3	0.101	17069	0.765
		5	0.012	2028	2.221
	FT	1	0.021	1260	2.817
		3	0.006	360	5.270
		5	0.000	0	

The above analysis assumes that count variation from sample to sample in a given size bin is described by a Poisson distribution. This is the limiting uncertainty due to the random arrival of particles into the APS. In practice, real changes in the atmospheric

aerosol e.g. as a result of flying through a smoke plume and APS instrument noise will also contribute to the sample standard deviation. By averaging over many samples these effects should be effectively smoothed out yielding average distributions that represent typical size distributions for the different regions and months. For June the reason the total counts for the UB are comparable to the FT (less for some diameters) because the total sample time was only 43 minutes compared with 244 minutes for the FT.

5.3.1 Conversion from Aerodynamic to Physical Diameter

The APS measures the aerodynamic diameter (D_a) of particles. If the density of the particles is around 1 g cm^{-3} then this is the same as the physical diameter (D) of the particles. However, in most cases the average density of the assumed internally mixed aerosol is greater than 1. In section 4.3 the results are presented for the average aerosol density and refractive index (Table 9) for the different altitude regions for both June and September, showing an average density around 1.5 g cm^{-3}. Hence, correction for non-stokesian effects on the aerodynamic diameter size distributions are unnecessary [21]. To obtain the desired physical diameter size distribution it is necessary to take account of the actual mass density of the internally mixed aerosol for the coarse mode and for the different altitude regions. Shape effects can be important, especially for non-spherically shaped salt crystals, which can compose a significant fraction of the coarse mode aerosol [36, 37]. In this report no attempt is made to take account of shape effects and the shape factor is assumed to be unity.

The following conversion equation was used:

$D = \frac{1}{\sqrt{\rho}} D_a$; where ρ is the average aerosol density.

A Cunningham slip correction factor [38] can also be included but was omitted for this work. The Cunningham slip correction factor should be close to unity for particles larger than 1 μm. Because an average coarse mode density was used the magnitude of the diameter conversion remains independent of diameter (within that mode), allowing simple scaling to physical diameter using the above equation. The normalized particle concentration per size bin does not alter (only the bin upper and lower limits and hence the GMD). The result is that the entire size distribution shifts to the left with the magnitude dependent on the density of the average internally mixed coarse mode aerosol. This correction has been applied to the plots in Figure 18.

5.3.2 APS Pressure Induced Size Shift

The APS will undersize particle diameters at low ambient pressure due to the change in the time of flight of the particle. This under sizing is greatest for particles less than 1 μm. TSI calibrate the APS at a fixed atmospheric pressure and hence the instrument

does not size particles accurately when operating on an aircraft at altitude. It is not practical to calibrate the instrument at all ambient pressures encountered. For this study the APS was calibrated on the ground at sea level and the altitude size shift was corrected in post processing of the data.

The size shift was measured in the laboratory using a purpose built pressure chamber over a range of pressures from around 1013 hPa down to around 500 hPa and for PSL spheres ranging from 0.7 to 20 μm in diameter. A table of APS size as a function of atmospheric pressure and PSL sphere diameter was generated [39].

In summary, at an ambient pressure of around 500 hPa the maximum size shift was 25% for particle diameters $\leq 1\ \mu$m and 13% for diameters $> 1\ \mu$m. In all cases the shift is towards smaller sizes. The majority of the aircraft flight legs were at altitudes where the APS pressure was above 720 hPa. In this case the maximum shift drops to 7%. This equates to one size channel (above 750 hPa) but is less certain since the peak was often spread across two bins.

These size shifts are larger than those reported by Huebert et al. [40]. They found for a 1 μm PSL sphere a size decrease of 3% when the pressure was decreased from 820 to 600 hPa. The present work gives a size decrease of around 13% or two size channels. This difference perhaps reflects the difficulty in performing these measurements and implies that a still unknown uncertainty needs to be attached to the correction. Consequently, rather then attempt to correct the size shift for this work the uncorrected sizes are used for the campaign average size distributions for the LB and UB regions. This can result in a slight distortion of the size distributions due to averaging over different altitudes (and hence pressures) with the maximum effect greatest for smaller particles. The maximum size shift for the vast majority of flight legs is one size channel based on our size-shift measurements. This is not insignificant but given the discrepancy with other size shift measurements by other groups, should be considered conservative.

The free troposphere data for September were generally measured at pressures less than 600 hPa where the magnitude of the size shift becomes more significant. However the main use of the APS is to measure the coarse mode distribution, which is negligible in the free troposphere. Therefore the region where the APS size shift starts to become significant is a region where the APS data are of less value when compared with the ASASP or SMPS data. If however the free troposphere APS size distribution is to be used then some account for the size shift needs to be made, probably involving re-binning the data so that it can more accurately be compared with the ASASP distribution. In this report the uncorrected FT data on the combined size distribution plots only are shown. Many of the size channels exhibit large fluctuations between samples and between channels, suggesting that sampling noise has more impact than systematic size shift effects.

5.4 Combined Size Distribution Data

Combining data from all four sizing instruments on one plot, such as Figures 19 and 20, gives an overall picture of the aerosol size distribution across four orders of magnitude in particle size and eight orders of magnitude in particle concentration. This allows rapid assessment of the agreement between the data from the different instruments. The ASASP and FSSP data do not include any correction to take account of possible differences between calibration and ambient refractive index. The conversion of aerodynamic to physical diameter for the APS is included but not the correction due to the pressure induced size shift. Overall the agreement shown in Figures 19 and 20, for the size distribution segments from the different sizing instruments is reasonable, lending confidence that this combination represents the true underlying physical size distribution.

One reason for the apparent mismatch between the external probes and the internal instruments is due to RH differences in the sampling. Dynamic heating in the isokinetic inlet and heating in the sampling lines and instruments primarily affects the internally mounted instruments, reducing the sample RH. Due to the hygroscopic nature of most aerosols this results in a size reduction.

The size and volume distribution functions displayed in sections 5.2 and 5.3 for the SMPS and APS more readily highlight the structure (shape) of the nucleation, Aitken, accumulation and coarse modes. These data are easier to use when fitting standard size distribution functions (Section 5.5). It is therefore of value to show the data in both forms particularly as the ASASP and FSSP do not individually cover entire size modes. The ASASP bridges the accumulation and coarse modes and the FSSP provides the large-particle end of the coarse mode.

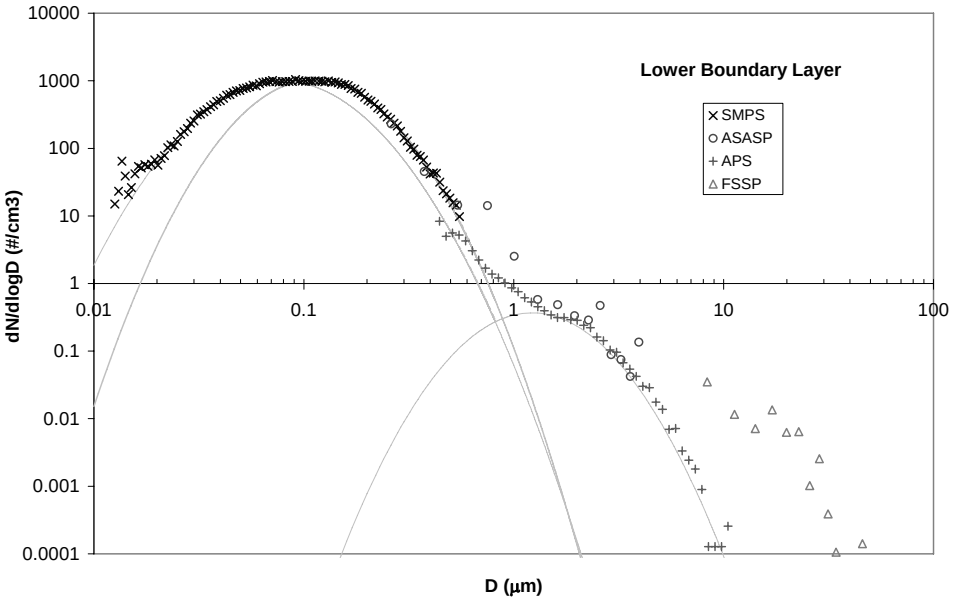
Lower Boundary Layer
SMPS
ASASP
APS
FSSP
dN/dlogD (#/cm3)
D (μm)
10000
1000
100
10
1
0.1
0.01
0.001
0.0001
0.01
0.1
1
10
100

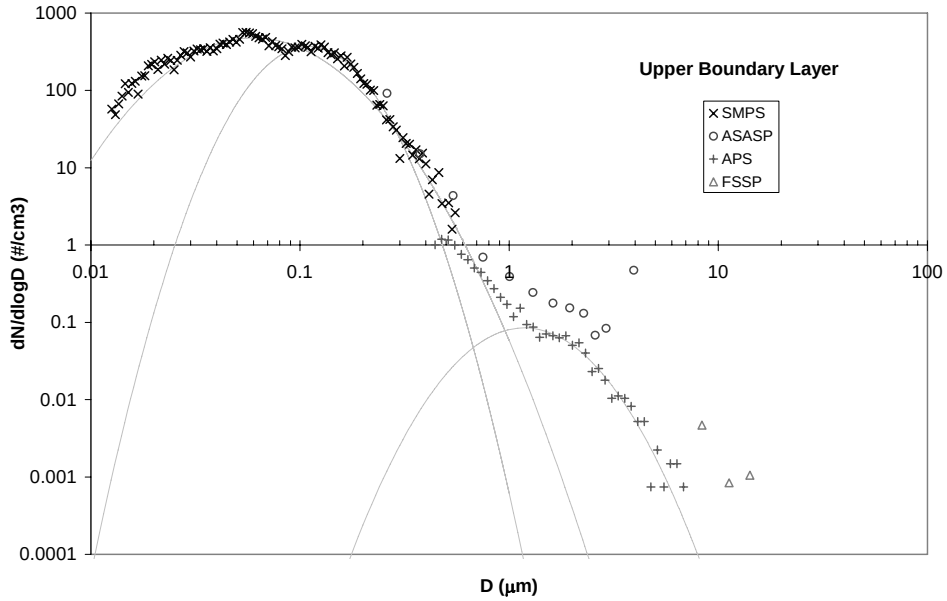
Upper Boundary Layer
SMPS
ASASP
APS
FSSP
dN/dlogD (#/cm3)
D (μm)
1000
100
10
1
0.1
0.01
0.001
0.0001
0.01
0.1
1
10
100

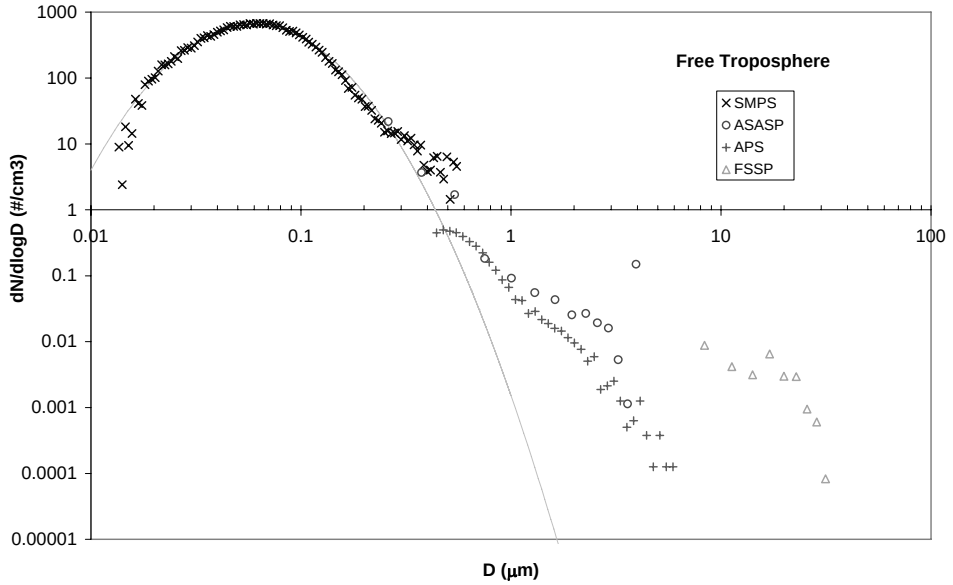

Figure 19: Combined average size distributions for June 2003. Also displayed are the fitted lognormal functions for the various modes using the parameters from Tables 13 and 14.

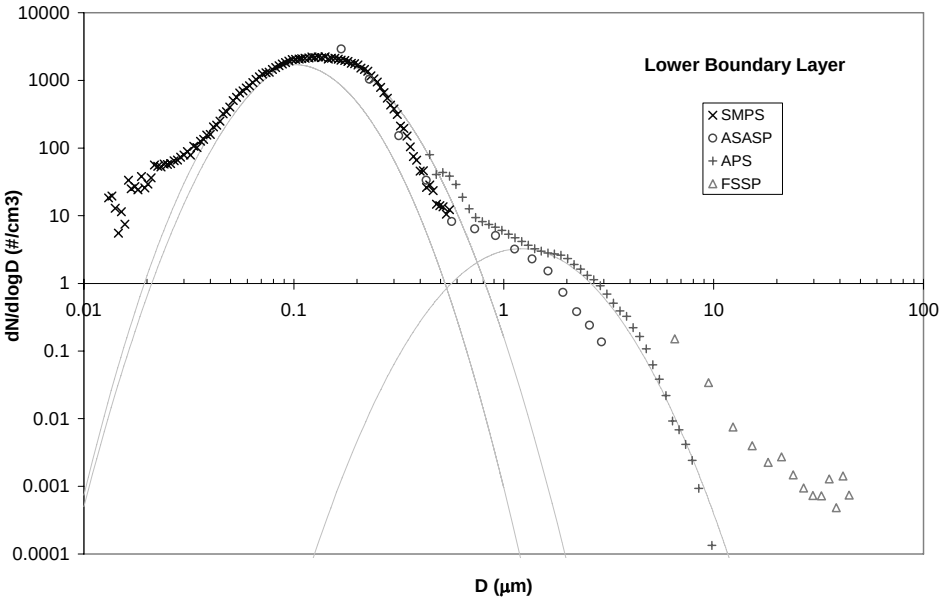

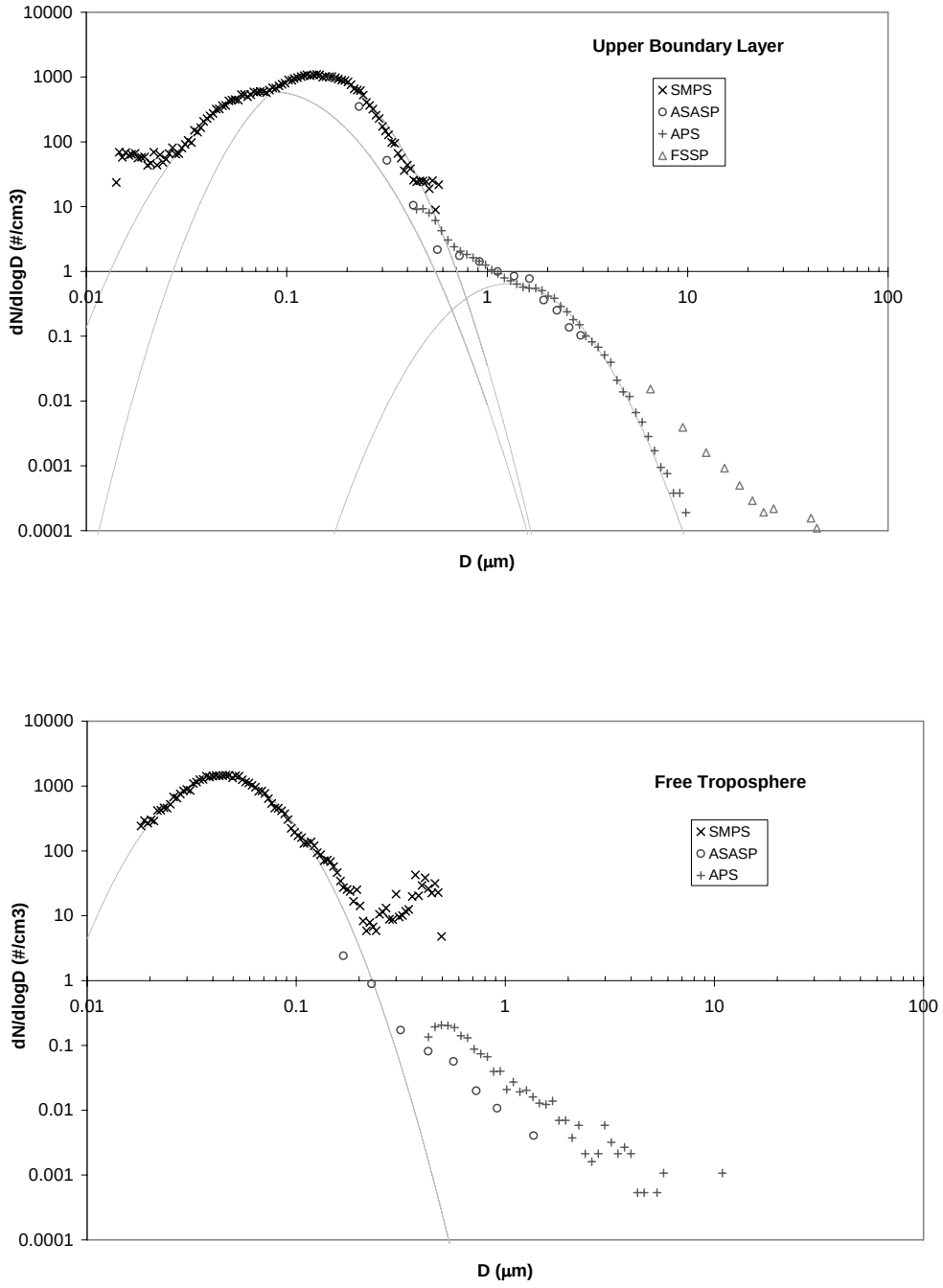

Figure 20: Combined average size distributions for September 2003. Also displayed are the fitted lognormal functions for the various modes using the parameters from Tables 13 and 14.

One feature that can be seen in Figures 19 and 20 is mismatch between the APS and FSSP data. This is particularly noticeable for June. The free troposphere coarse mode data is not considered reliable, as it is quite noisy and the coarse mode concentration is very low. The RH is generally low in the FT so this should not have a major impact on size measurements. The refractive index of the aerosol in the FT could be different from the calibration particles. In this case the impact of correcting for the FSSP data for ambient RI could be significant. Differences between the APS and FSSP, as plotted here, will generally derive from a combination of effects including, uncorrected altitude sizing shift in the APS, dry size determined with the APS versus ambient with the FSSP, inlet transmission function for the APS, refractive index correction for the FSSP, systematic volume sampling errors in both instruments and different measurement metrics (e.g aerodynamic size corrected to physical size versus optical size). Notably the differences typically show lower large particle concentrations for the APS at large sizes consistent with a diameter growth of around a factor of two between dry and ambient and possibly significant inlet transmission losses for particle diameters larger than around 5 μm.

Generally the ASASP data bridge the distributions from the SMPS and APS satisfactorily. Here also differences can be expected due to difference in sampling humidity (ASASP at ambient, SMPS and APS dried), inlet transmission function, ASASP refractive index correction (relatively small based on determined ambient refractive indices) and measurement metrics (optical size for ASASP, mobility size for SMPS and aerodynamic size corrected to physical size for APS), also uncorrected altitude size shift for the APS and systematic flow and calibration errors on all instruments. Each of these instruments also tends to be prone to increased uncertainty towards the lower and upper ends of their sizing ranges, and this can be exaggerated at increased altitude.

In the next section the fitting procedure adopted to determine the fine and coarse mode aerosol size distribution functions is outlined. In that procedure, data was assessed and truncated to minimise the effects of sampling artefacts. In this way the best possible fit was found using the available data. ASASP and FSSP data were not used to fit the dried particle functions, since this would require both refractive index correction and humidity growth correction

5.5 Fitting Size Distribution Functions

The most efficient and useful way to summarise the size distribution data obtained from the range of instrumentation used is to fit analytic size distribution functions. The following size distributions have been fitted to data obtained from the SMPS and APS. Therefore they represent a ‘dry’ aerosol size distribution as opposed to an ambient size distribution.

As has been observed during these measurement campaigns the aerosol can be described as comprising four different size modes: usually known as the nucleation, Aitken, accumulation and coarse modes. Normally the overall size distribution can be approximated as the sum of these separate modes, each with its own lognormal distribution. Other types of distributions also prove useful in describing the coarse mode, particularly the Junge (or power law) distribution is sometimes used to describe the distribution shape for particles larger than a few tenths micrometre diameter.

The general fitting procedure adopted was a non-linear least squares technique using the weighted cumulative distribution function rather than the density function, for an improved fit. The non-linear optimisation was performed using mathematical software, MATLAB® (© 1994-2005 The MathWorks, Inc.) and Mathcad® (© 2005 Mathsoft Engineering & Education, Inc.), as described in Appendix A. The procedure involved establishing first guesses of the lognormal parameters (defined below) and using them to iteratively acquire a minimised solution of the weighted least squares (WLS; Appendix A). In general, the minimisation technique produced stable, convergent solutions, as presented in Tables 13 and 14. MATLAB and Mathcad produced the same answer within the accuracy of each method. The results presented in Tables 13 and 14 were obtained using MATLAB.

For the coarse mode, where the counts are low, it was advantageous to fit the volume distribution rather than the number distribution. In each case the three mode parameters for the lognormal were determined, A_i the total number of particles in the mode, the count median diameter (or geometric mean diameter) D_{m_i} and the geometric standard deviation σ_i.

The lognormal function takes the form

$$\frac{dN(D;A_i,D_{m_i},\sigma_i)}{d\ln D}=\frac{A_i}{\ln(\sigma_i)\sqrt{2\pi}}\exp\left[\frac{-(\ln D-\ln(D_{m_i}))^2}{2(\ln(\sigma_i))^2}\right].$$

Here the function is represented in its more familiar natural logarithm form. The parameters were determined by fitting the data on a log base 10 scale, as displayed in the size distribution plots (Figures 19 and 20). The volume distribution rather than the current number distribution function can be obtained by replacing N with V; A_i with the total volume of mode "i", V_{A_i}; and D_{m_i} with the volume median diameter D_{Vm_i}. Once these fitted parameters have been determined there are relationships that exist between A_i and V_{A_i} and between D_{m_i} and D_{Vm_i} (the Hatch-Choate conversion equations) enabling determination of the number distribution parameters from the fitted volume distribution parameters.

Table 13: The parameters of the fitted lognormal size distribution function for the fine mode aerosol. For the boundary layer regions in September two sets of data are presented corresponding to treating the Aitken and accumulation modes separately and treating the fine mode as one mode. A is $\#/cm^3$ and D is in μm.

Distribution	A_1	D_{m_1}	σ_1	A_2	D_{m_2}	σ_2	A	D_m	σ
June 03									
LB	630	0.078	1.785	575	0.112	1.669			
UB	345	0.060	1.940	173	0.110	1.534			
FT							397	0.059	1.743
Sept 03									
LB	795	0.101	1.533	1170	0.131	1.591	1240	0.126	1.655
UB	355	0.085	1.687	522	0.138	1.546	652	0.122	1.892
FT							667	0.044	1.546

Table 14: The parameters of the fitted lognormal volume and calculated size distribution functions for the coarse mode aerosol. V_{A_c} is $\mu m^3/cm^3$, A is $\#/cm^3$ and D is in μm.

Distribution	V_{A_c}	D_{Vm_c}	σ_c	A_c	D_{m_c}
June 03					
LB	0.658	2.720	1.675	0.207	1.224
UB	0.141	2.658	1.680	0.048	1.184
Sept 03					
LB	4.975	2.540	1.644	1.762	1.211
UB	1.033	2.535	1.610	0.336	1.283

The SMPS distributions in the lower regions of the atmosphere exhibit a bi-modal structure. For September, where the accumulation mode dominates, this shows up as a small shoulder, which can be attributed to a smaller Aitken mode due to fresh young smoke. In June the Aitken mode and accumulation mode are similar in magnitude resulting in a clear bimodal structure for the fine mode size distribution. Whereas the June data are evidently best represented by a bimodal distribution function, the modal structure of September is not as distinct and could be represented by a single mode. Consequently two alternative distributions are presented for September. One includes an Aitken mode separately to the accumulation mode and the other treats the fine aerosol as a single mode. In the case of fitting two modes each mode was treated separately. In the majority of cases there was sufficient structure in the size distribution to make a split between the two modes, and each mode was fitted using a truncated data set that was sufficient to provide a unique and reproducible fit. For both the single and double mode structures, the noisy data in the smallest radii bins were excluded from the minimisation procedure. This was necessary in order to produce stable and convergent fitted size distribution functions.

Some inaccuracies in the fitted coarse mode volume distributions result from poor constraint less than 0.7 μm and greater than 5 μm diameter. The data outside these limits was not used due to known counting and sampling losses. The mismatch between the APS and FSSP in this region is too great to combine the data without correction for humidity growth.

Only the APS data were used to constrain the fitted volume distribution, and this was truncated for diameters less than about 1.5 μm and greater than about 4.8 μm. The volume distributions clearly show the impact of the accumulation mode at diameters less than 1.5 μm. This shows up as a sharp increase in the slope of the distribution as the accumulation mode particles start to dominate the coarse mode concentration in these size bins (Figure 18). It is also likely that concentration data from this instrument will be less accurate at diameters greater than 5 μm due to losses in the isokinetic inlet. The calculated number distribution is shown on the combined size distribution plots. It would be possible to use the ASASP and FSSP data, although the same issue arises with an even larger mismatch between the two data sets. This data would also require some extrapolation between the size limits of the two probes.

A lognormal distribution was fitted to the coarse mode rather than a Junge distribution although there is enough uncertainty in the data to allow for both types of size distribution. The ultimate use of these fitted size distribution functions is in calculations of aerosol optical properties such as scattering coefficients that involves integration with the scattering cross section, a non-linear function of particle diameter. As noted in Seinfeld [41] use of Junge distributions in higher order calculations of aerosol quantities such as the volume distribution or optical properties should be avoided.

5.6 Ground Based Measurements at Jabiru

A GRIMM solid-state laser single particle spectrometer was installed at Jabiru for both campaigns. This provided ground level data for the aerosol properties at Jabiru and also indirectly for the region around Jabiru where the aircraft flights were conducted.

The instrument was set to sample at 60-second intervals and the size range covered was from 0.3 μm to 20 μm in 15 size channels. These data were analysed for both the fine and coarse mode number concentration variation and campaign averages were also produced for the size distribution (not displayed here). The main constituents of the aerosol particles that appear to impact on the fine and coarse mode number concentration are biomass smoke and sea salt.

In September a diurnal pattern was observed in the coarse mode concentration and that was repeated throughout the entire week. This occurred because in the late evening and through the early hours of the morning the winds at Jabiru were strongly from the north to northwest. This direction represents the shortest path between Jabiru and the coast. During these periods the coarse mode concentration was seen to rise to a

maximum due to sea-salt before dropping away as the winds started to move around from the East. A similar but less pronounced pattern was also observed in the fine mode concentration (Figure 26 for the total concentration, which is dominated by the fine mode aerosol), which has been identified to be the result of two pockets of fires to the northwest and north of Jabiru that would have resulted in smoke being blown towards Jabiru during these times. Smoke from these fires should not have impacted on the aircraft measurements, as conditions were either calm or winds had swung around from the east during these measurements. This illustrates the potential for measurements at Jabiru to be biased by events not seen during the aircraft measurements. However the nature of the fuel source being burnt in these fires is the same as the fires in Arnhem Land. The main impact would be that the MOUDI and NOAA impactor 24 -hour average samples will show somewhat different contributions of smoke, to the campaign averages from the aircraft measurements.

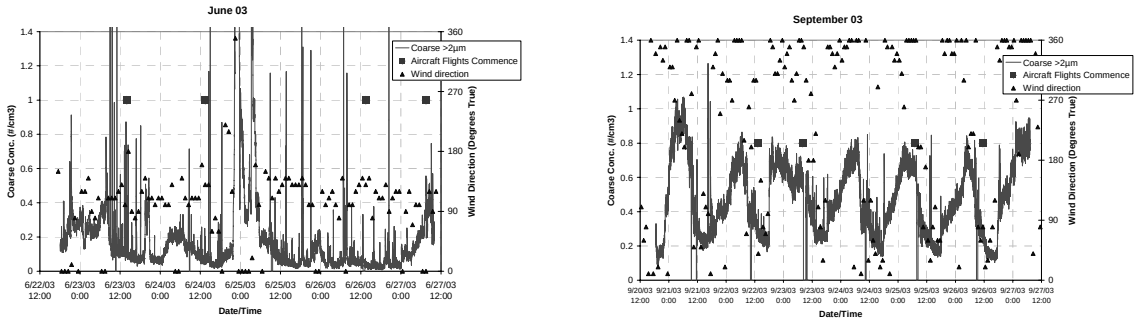

Figure 21: Coarse mode concentration and wind direction over the specified dates highlighting the strong correlation of wind direction with coarse mode concentration for September.

Wind rose data and historical average meteorological data from Jabiru [42] suggest that the weather patterns observed during the study, particularly wind direction, were typical for both June and September. Hence this type of pattern would be expected in the coarse mode concentration in September in general, but the fine mode variation would be dependant on the presence of fires to the north or northwest of Jabiru.

The winds encountered in June were from the east to southeast and hence the diurnal coarse mode concentration variations seen in September were not observed and concentration changes appeared to be more random. The wind pattern also had an impact on the aircraft measurements, which were flown after 7 am local time. Generally the wind was either calm or from the east during the day. Most of the smoke encountered emanated from fires burning in Arnhem Land, which therefore can be considered the primary source of the fine mode aerosol. However during the morning flights in September the coarse mode peak was observed (Figure 21) representing elevated levels of coarse mode aerosol resulting from sea salt generation. This is the most likely explanation for the increase in the coarse mode concentration that was observed in the boundary layer distributions in September.

Weather patterns clearly played a major role in the observed differences in the aerosol characteristics between June and September. Most notably the increase in fire activity east of Jabiru in Arnhem Land combined with strong Easterlies during the day and a change in wind direction at night, resulting in elevated levels of sea salt in the atmosphere.

6. Aerosol Optical Property Measurements

Measurements of the atmospheric aerosol light scattering and absorption coefficients were made using a nephelometer and an absorption photometer (absorption data are not presented in this report). The nephelometer measures the scattering coefficient at wavelengths of 450, 550 and 700 nm, which shall be referred to subsequently as Blue (B), Green (G) and Red (R). The three wavelengths allow calculation of the Ångstrom exponent, a measure of the size dependence of the scattering. It is also possible to calculate the single scattering albedo, the ratio of scattering to extinction, from the light scattering and absorption coefficients.

The Ångstrom exponent is defined as

$$\mathring{A}(\lambda_B / \lambda_R) \equiv (\lambda_B / \lambda_R) = \log(\beta(\lambda_B) / \beta(\lambda_R)) / \log(\lambda_R / \lambda_B)$$

where $\beta(\lambda_i)$ is the scattering coefficient at the wavelength λ_i, $i = B, R$ and with λ_i given in nm.

Flight leg medians were calculated for both the green (550 nm) scattering coefficient and the Ångstrom exponent (450 nm/700 nm). This information is displayed as modified box plots in Figures 22-25. The box plots provide a useful indication of the variation in scattering coefficient across the flight legs with the outliers generally associated with smoke plume samples. This variation was more dramatic in June than September, since the median scattering coefficients were very low in June and scattering coefficients associated with smoke plumes encountered along the flight path were well in excess of median levels.

Morning flights showed more stratification of the atmosphere than those carried out in the afternoon. This is evidenced by a greater variation in measured aerosol quantities as a function of altitude below the inversion.

The 4.5 km (15kft) flight leg from flight 1 in September was excluded because of the presence of extensive cloud. The 4 and 5 km flight legs for flight 2 in September have been included although the aircraft clipped some cloud tops. All of these flight legs were excluded from the campaign-average size distributions.

6.1 Nephelometer – Flight Leg Statistics

In the box plots altitude is plotted in kilo feet (kft) which is the metric used for altitude on-board the aircraft. The aircraft altimeter was calibrated in feet and the altitudes flown were in multiples of 500 feet. To convert from kilo feet to km multiply by 0.3.

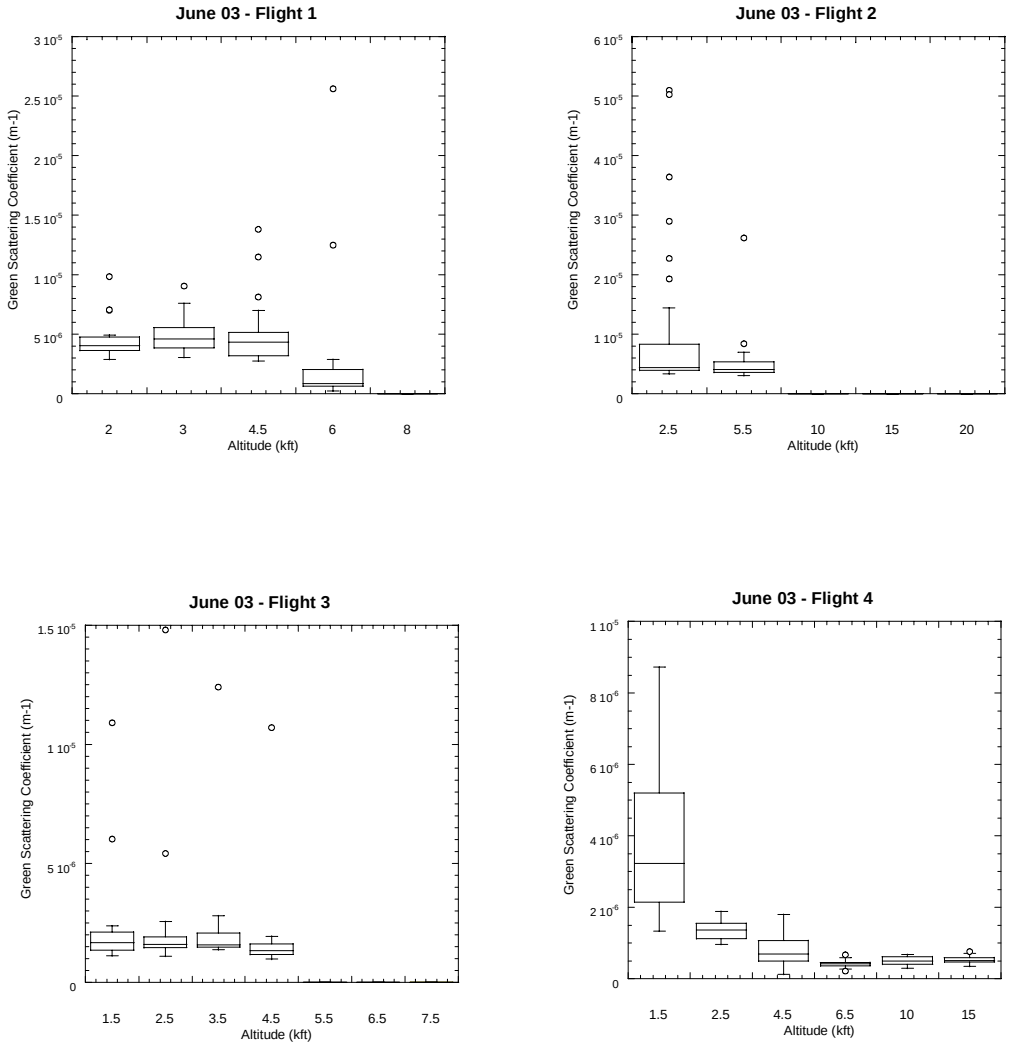

Figure 22: Modified Box plots of the scattering coefficient at 550 nm (green) for the individual flights legs for June 2003. The scattering coefficients are given in units of m^{-1}. The solid line is the median value and the lower and upper line of the box represent the 25th (lower quartile (LQ)) and 75th percentile (upper quartile (UQ)) respectively. The whiskers are points within which data is statistically significant i.e. the upper whisker = UQ + 1.5 IQD and the lower whisker = LQ - 1.5 IQD, where IQD= UQ - LQ is the inter quartile distance. The open circles represent outliers. Note that the outlier samples are typically those where the aircraft either flew directly through a plume or was impacted by smoke from fires nearby. They occur predominantly for afternoon flights when fresh fires are burning. Flight legs that have no data are below the sensitivity of the instrument.

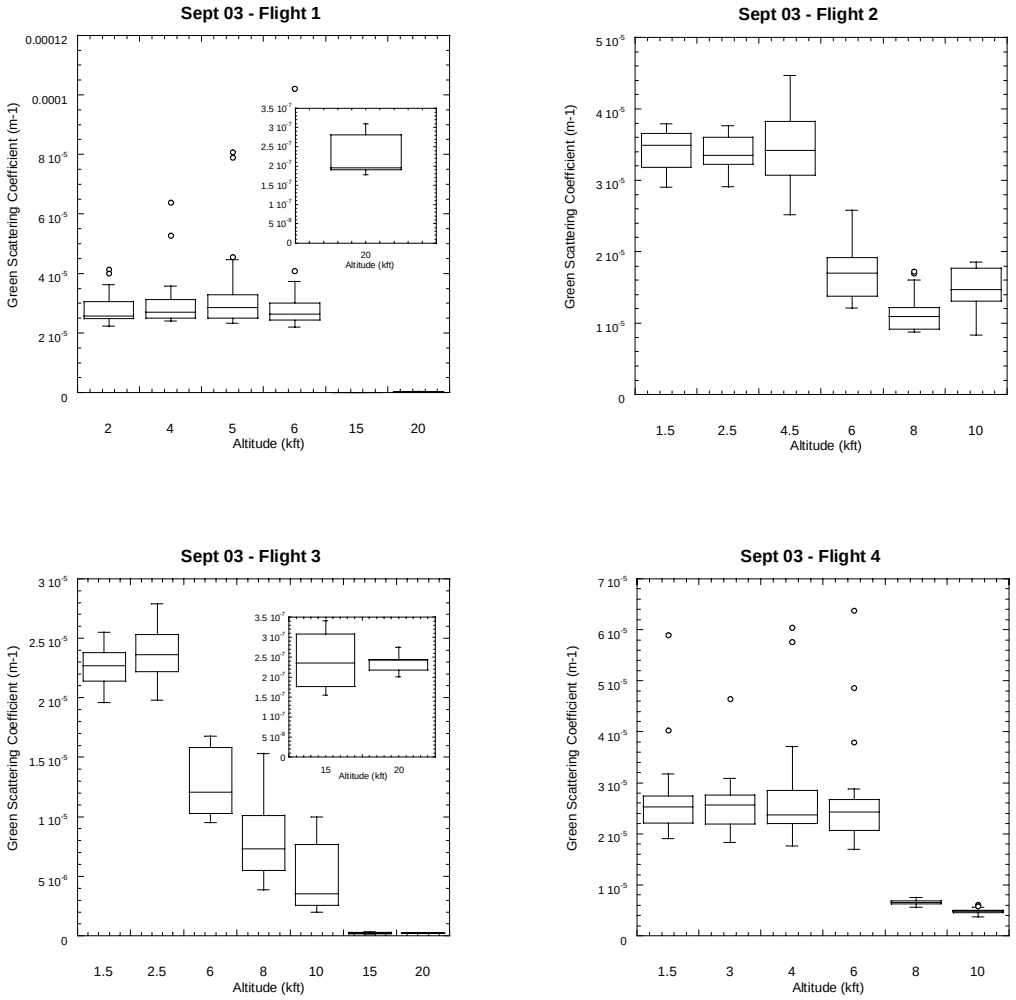

Figure 23: Modified Box plots of the scattering coefficient at 550 nm (green) for the individual flights legs for September 2003. The scattering coefficients are given in units of m^{-1}. *Note that the outlier samples are typically those where the aircraft either flew directly through a plume or was impacted by smoke from nearby fires. They occur predominantly for afternoon flights when fresh fires are burning. Flight legs that have no data are below the sensitivity of the instrument. The insets show the FT flight leg Modified Box Plots on a different scale for given flight legs.*

The results for September highlight changes in altitude profile of the aerosol scattering coefficient (and concentration) between morning (flights 2 and 3) and afternoon flights. One noticeable feature in the upper boundary layer 550 nm (green) scattering coefficient is a clear variation with altitude in the morning flights, showing the stratified nature of the atmosphere, and hence aerosol concentration, in this region.

This is also evident in flight 4 for June, the only morning flight. The LB legs for June and September for both morning and afternoon flights produce median scattering coefficients at 550 nm (green) that are similar in magnitude across each flight leg on those particular flights. This reflects the uniformly mixed nature of the aerosol in the lower region of the boundary layer.

Another striking feature of these plots is the lack of outlier samples for morning flights. This is attributed to a reduced number of smoke plumes, where many fires have burnt out or died down over the previous night and the build up, or initiation of new fires, has not occurred before the time of sampling.

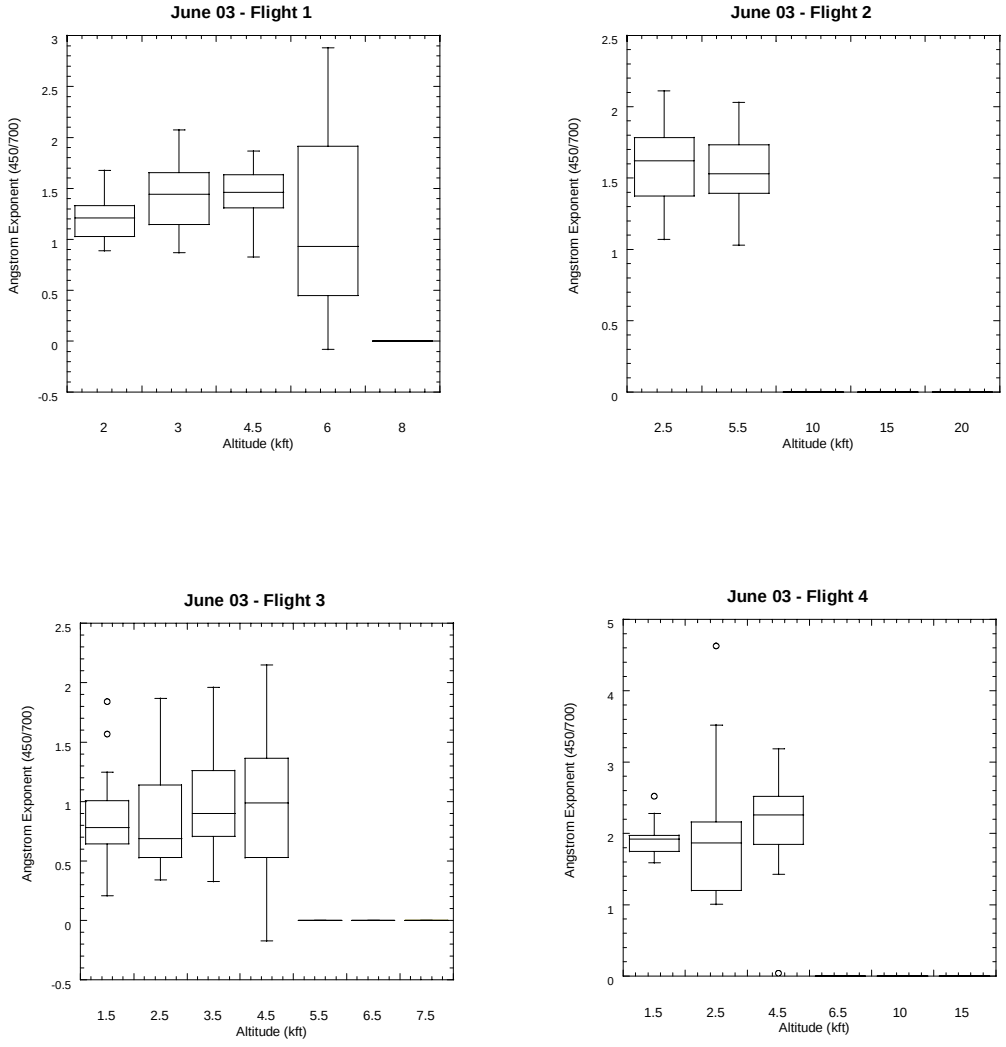

Figure 24: Modified Box plots of the Ångstrom exponent (450/700) for the individual flight legs for June 2003. The Ångstrom exponent is unit less. Flight legs that have no data plotted are below the noise response of the instrument at blue and/or red wavelengths.

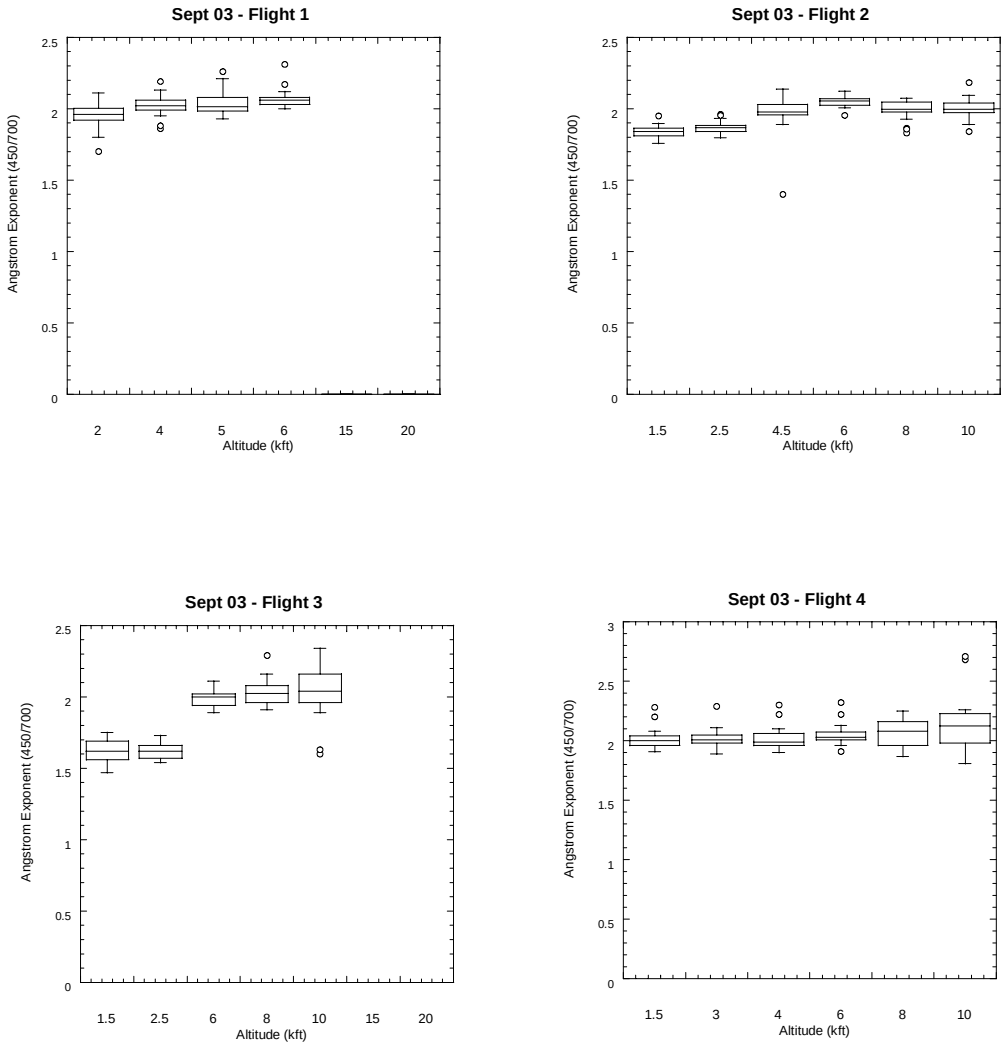

Figure 25: Modified Box plots of the Ångstrom exponent (450/700) for the individual flights legs for September. The Ångstrom exponent is unit less. Flight legs that have no data plotted are below the noise response of the instrument at blue and/or red wavelengths.

The Ångstrom exponent indicates the relative amounts of scattering at short and long wavelengths (here blue and red). This in turn reflects the nature of the underlying aerosol mixture and particularly the size distribution. In the majority of cases in September, the median Ångstrom exponent is around 2 except for flight 3. In the latter case the lower boundary layer flight legs reflect a slightly stronger large particle scattering, which lowers the Ångstrom exponent for these two flight legs. This was a very early morning flight and the source of the course mode aerosol is likely to have been sea salt. As discussed previously, the coarse mode number concentration at Jabiru had a periodic diurnal pattern with the peak occurring through the early hours of the morning (Section 5.6). As the wind became more easterly during the day the sea salt concentration dropped. It is most likely that because flight 3 was conducted earlier in

the day than flight 2, a higher level of sea salt aerosol was encountered which preferentially increased the red scattering coefficient, lowering the Ångstrom exponent for the lower altitude legs. The median Ångstrom exponent was broadly similar for all of the September boundary layer altitudes, other than for flight 3.

The June Ångstrom exponent data reflect a much lower aerosol concentration. The spread around the median values is very large, with blue and red scattering coefficients in many cases near the detection limit of the instrument. Consequently, these data should be viewed with some caution. Ångstrom exponents are generally smaller than those observed in September indicating relatively greater concentrations of smaller particles, consistent with the observations of particle size distribution.

Ångstrom exponent data for the morning flight in June (flight 4) had a median value of around 2, similar to exponents observed in September and indicative of a mix of smoke and other aerosol components on that flight similar to those encountered in September.

6.2 Ground Based Measurements at Jabiru

A Radiance Research nephelometer, operating at a single wavelength of 530 nm (green) was installed at ERISS in Jabiru during the June and September campaigns. This nephelometer was set up to measure the scattering coefficient for a dry aerosol i.e. RH < 40%. For the September deployment, a second radiance research nephelometer was also installed to simultaneously measure the scattering coefficient at near to ambient RH. Both nephelometers were operated continuously during the time of the aircraft measurements except for a period of about 30 hours between 9 am on the 23rd September through to 2 pm on the 24th September when the ambient nephelometer was offline.

The purpose of these measurements was to obtain values for the ground based scattering coefficients complementing values obtained from the aircraft measurements. In September a second objective was to measure f(RH) *in situ* to allow for humidity growth correction for scattering coefficients measured on the aircraft in the boundary layer. Corrected scattering coefficients can be obtained by converting the scattering coefficients measured at the nephelometer sample RH to ambient RH using the expression for $\beta_{sc}(\gamma)$ and the value of ξ obtained from the f(RH) measurements (Appendix B.1). This is important especially towards the end of the dry season when RH on the ground especially during the morning can approach 60%.

The temporal record of the dry scattering coefficient (5 minute averages) shows the obvious presence of fires close to Jabiru in June. As expected, there is strong correlation between the scattering coefficient and the total number concentration (1 minute averages).

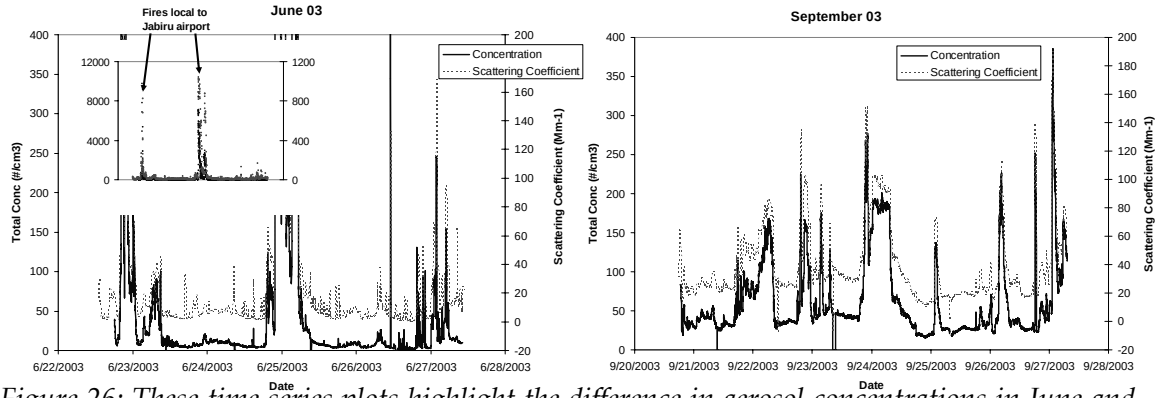

Figure 26: These time series plots highlight the difference in aerosol concentrations in June and September. Generally, aerosol concentrations are greater in September, although two fires that were local to Jabiru were observed in June (see inset).

The diurnal variation in concentration for September is a result of a combination of fires to the north and northwest of Jabiru and prevailing wind conditions as discussed in Section 5.6. Most of the peaks that occur around midnight are attributed to smoke that has blown towards Jabiru on the prevailing northerlies that occurred overnight in September. These elevated levels will bias the 24-hour mass samples (for chemical analysis) and hence will not represent typical daytime levels of smoke present at Jabiru.

Fires in Arnhem Land that impacted the various boundary layer flight legs, particularly in the north-east sector of the flight legs, had a smaller impact at Jabiru. This is most likely due to strong easterlies transporting the smoke to just to the north of Jabiru. Smoke from some of the fires further east over near the Gulf of Carpentaria should have reached Jabiru. There was an overall increase in particle number concentration in September (Figure 26), which is also evident in the scattering coefficient data. In addition to changes in particle concentration; other factors influencing the ambient scattering coefficient changes will include particle size distribution and composition, also relative humidity.

7. Conclusions

Results of aircraft-based measurements of the atmospheric aerosol in the vicinity of Jabiru, N.T. have been analysed and presented here. Two measurement campaigns were conducted, the first in June and the second in September 2003; these enabled an examination of differences in aerosol properties between the start and the end of the dry season. The range of instruments used during the campaigns gave a relatively complete characterisation of the aerosol, including microphysical, chemical and optical properties of the aerosol.

The main results are:

1. The biomass burning aerosol (smoke) concentration and light scattering coefficients aloft were found to be much greater in September than June.
2. Particle number size distributions observed in the boundary layer in September were dominated by a mode at around 150 nm diameter, usually identified as the accumulation mode. In the free troposphere the dominant mode was more typically around 50 nm diameter. The majority of particles in these modes are most likely to be composed of aged smoke (more than a few hours) reflecting elevated levels of smoke in the boundary layer.
3. In June, particles in the free troposphere particle number size distributions were dominated by a mode with a typical (mode) diameter of around 60 nm and in the boundary layer by two modes with typical mode diameters around 50 nm and 100nm. These modes are usually identified as Aitken and accumulation modes. These differences in mode properties with altitude and season highlight the complexities of understanding ambient aerosol and difficulties in interpreting contributions from background, emissions from specific sources and aerosol evolution during transport.
4. In both June and September the coarse mode aerosol was characterised by a mass distribution mode with a typical (mode) diameter of around 3 μm. Chemical components were also similar in June and September. The major component appears to be sea salt with some contribution from soil. The ground based chemistry measurements at Jabiru were strongly influenced by local weather patterns. In September particularly, when winds over night were from the northwest resulting in greater sea salt concentrations. This also produced a periodic diurnal variation in the coarse mode concentration for September that was not evident during June.
5. Ground based concentrations of the fine mode aerosol (smoke) concentration at Jabiru were closely linked to the presence of spot fires and influenced strongly by wind pattern.

Further work will involve incorporating the absorption coefficient with the green scattering coefficient to calculate the single scatter albedo and the correction of the ASASP and FSSP size distributions for ambient refractive index. Corrections of the scattering coefficients for angular truncation errors will be made and for the ambient RH making use of the expressions given in Chapter 6. Some attempt could be made to determine the effect RH changes have on the sizing of the SMPS and APS. A future closure study should be possible by comparing measured scattering coefficients with values calculated using the particle size distribution and chemical composition. Another form of closure study should be possible by comparing in-situ extinction coefficients with column integral values derived remotely at ground level.

These results will form part of the final version of the report, which will be published in the open scientific literature as a complete closure study of the atmospheric aerosol in the vicinity of Jabiru. This additional analysis is not expected to impact significantly on the use of the results presented in this report. It is the knowledge on the particle number size distribution in the different regions of the atmosphere and on the chemical composition of the aerosol that will be of immediate benefit to users in DSTO. These results will be used to assess the level of fidelity of currently available aerosol models, such as those found in MODTRAN.

In conclusion it is worth emphasising that this is the first complete set of aerosol measurements from this region of the continent. As such they provide DSTO with a unique knowledge base from which to evaluate aerosol models and hence to apply them with a greater deal of accuracy then has been possible previously. This set of airborne measurements will form the quantitative basis for further work that is done by DSTO on aerosol models, particularly as it relates to providing advice to the ADF on the performance of military E/O sensors.

8. Acknowledgements

The authors' acknowledge the efforts of the Chief ARA pilot Gabriel Kalotay and the Chief Engineer Rudi Gaissmaier. Special thanks are given to Mark Burridge for machining the adaptors for the isokinetic inlet and for the APS and nephelometer and for providing on ground support during the weeks of the test flights and during the measurement campaigns. The efforts of the CSIRO team of Mr Bernard Petraitis, Mr Charles Tivendale and Dr Bim Graham are appreciated. Bim's efforts in running the instruments at Jabiru and for the initial analysis of the ground based chemistry measurements are particularly appreciated. Finally thanks are given to Dr Zoran Ristovski from QUT who was responsible for the installation, testing and data collection for the QUT SMPS during June and to Dr Milan Jamriska for the same in September. QUT also provided us with the raw SMPS size distribution data, which was used in the analysis presented in this report.

9. References

1. Kneisys, F. X. et al. (1995) *The MODTRAN 2/3 and LOWTRAN 7 Model*, Ontar Corporation, North Andover MA
2. Carr S. B. and Burridge M. A. (2004), The Operation of a Three Wavelength Nephelometer and some Measurements made at Jabiru During 2002, DSTO Technical Note DSTO-TN-0544
3. Carr S. B. (2004), Transcontinental Aerosol Measurements from Adelaide to Darwin, DSTO Research Report DSTO-RR-0285
4. Gras, J. L. (1991) Southern Hemisphere Tropospheric Aerosol Microphysics, *J. Geophys. Res.*, **96** (D3) 5345-5365
5. Tsutsumi, Y. et al. (1999) Aircraft measurements of ozone, NOx, CO, and aerosol concentrations in biomass burning smoke over Indonesia and Australia in October 1997: Depleted ozone layer at low altitude over Indonesia, *Geophys. Res. Letters,* **26** (5) 595-598
6. Gras, J. L. et al. (1999) Some Optical Properties of Smoke Aerosol in Indonesia and Tropical Australia, *Geophys. Res. Letters,* **26** (10) 1393-1396
7. Maenhaut, W. et al. (2000) Aerosol Composition at Jabiru, Australia, and Impact of Biomass Burning, *J. Aerosol Sci.*, **31** (Suppl. 1) S745-S746
8. Dyce, P. (October 2004) Sentinnel Hotspots, *CSIRO Land and Water* http://www.sentinel.csiro.au/
9. Jacklyn, P. (October 2004) Savanna Information, *Tropical Savannas CRC* http://savanna.ntu.edu.au/information/index.html
10. International Global Chemistry Project (November 2004) Aerosol Characterisation Experiment Asia http://saga.pmel.noaa.gov/aceasia/index.html
11. TSI Inc. (April 2001) Model 3550/3560 Series Integrating Nephelometer, *Instruction. Manual,*P/N 1933563 http://www.tsi.com/documents/1933563d-3550-3560.pdf
12. TSI Inc. (January 2004) Model 3321 Aerodynamic Particle Sizer® Spectrometer, *Instruction Manual,* P/N 1930092, Revision E http://www.tsi.com/documents/1930092e-3321.pdf
13. TSI Inc. (June 2004) Model 3936 SMPS (Scanning Mobility Particle Sizer), *Instruction Manual,* P/N 1933796, Revision I http://www.tsi.com/documents/1933796i-3936.pdf
14. Gras, J. L. (2003) The CSIRO Isokinetic Aerosol Inlet, Internal CSIRO Division of Atmospheric Research Report
15. *see e.g.* Baumgardner, D. (2003) Airborne Measurements for Cloud Microphysics, *RAF Technical Bulletin No. 24* http://raf.atd.ucar.edu/Bulletins/bulletin24.html
16. Wilson, J. C. and Seebaugh W. R. (2001) Measurement of Aerosol from Aircraft In: Baron P. A. and Willeke K. (eds.) *Aerosol Measurement: Principles, Techniques and Application, 2nd Edition*, John Wiley and Sons, New York, Chapter 30

17. Baron P. A. and Willeke K. (2001) Gas and Particle Motion: Baron P. A. and Willeke K. (eds.) *Aerosol Measurement: Principles, Techniques and Application, 2nd Edition*, John Wiley and Sons, New York, Chapter 4 pgs 63-64
18. Brockmann, J. E. (2001) Sampling and Transport of Aerosols In: Baron P. A. and Willeke K. (eds.) *Aerosol Measurement: Principles, Techniques and Application, 2nd Edition*, John Wiley and Sons, New York, Chapter 8
19. Armendariz, A. J. and Leith, D. (2002) Concentration measurement and counting efficiency for the aerodynamic particle sizer 3320, *Journal of Aerosol Science,* **33** 133-148
20. Southern Fine Particulate Monitoring Project (July 2002) Seventh Quarterly Progress Report Reporting Period: April 1 – June 30, 2002, *DOE Cooperative Agreement No. DE-FC26-00NT40770,* Southern Research Institute, Birmingham, AL
    http://www.netl.doe.gov/coal/E&WR/air_q/docs/40770R07.pdf
21. Chen, B. T. et al. (1990) A Study of Density Effect and Droplet Deformation in the TSI Aerodynamic Particle Sizer, *Aerosol Science and Technology,* **12** 278-285
22. Ristovski, Z. (2004) *Private Communication*, Queensland University of Technology
23. Hanel, G. (1987) Radiation budget of the boundary layer: Part II, Simultaneous Measurement of Mean Solar Volume Absorption and Extinction Coefficients of Particles, *Beitr. Phys. Atmosph.*, **60**, 241-247
24. Marple et. al. (1991) A Micro-orifice Uniform Deposit Impactor (MOUDI): Description, Calibration and Use, Aerosol Science and Technology, **14** 434-446
25. Twomey, S. A. and Zalabsky, R. A. (1981) Multifilter technique for examination of the size distribution of natural aerosol in the submicrometer range, *Environmental Science and Technology*, **15** 171-184
26. Winklmayr, W., Wang, H-C., and John, W. (1990) Adaptation of the Twomey algorithm to the inversion of cascade impactor data, *Aerosol Science and Technology*, **13** 322-331
27. Ayers, G. P., M. D. Keywood, J. L. Gras, D. Cohen, D. Garton, and G. M. Bailey (June 1999) Chemical and physical properties of Australian fine particles: A pilot study. Report prepared for the Environment Protection Group, Environment Australia.
    http://www.dar.csiro.au/res/aq/CSIRO_AFP.pdf
28. Quinn, P. K. and Coffman, D. J. (1998) Local closure during the First Aerosol Characterization Experiment (ACE1): Aerosol mass concentration and scattering and backscattering coefficients. *Journal of Geophysical Research*, **103** 16575-16595
29. USEPA (1994) Quality Assurance Handbook for Air Pollution Measurement Systems, Volume V: Precipitation Measurement Systems (Interim Edition), Research Triangle Park, N.C.
30. Birch, M. E., and R. A. Cary (1996) Elemental carbon-based method for monitoring occupational exposures to particulate diesel exhaust, *Aerosol Science and Technology*, **25** 221-241

31. Schmid, H., L. Laskus, H. J. Abraham, U. Baltensperger, V. Lavanchy, M. Bizjak, P. Burba, H. Cachier, D. Crow, J. Chow, T. Gnauk, A. Even, H. M. ten Brink, K.-P. Giesen, R. Hitzenberger, C. Hueglin, W. Maenhaut, C. Pio, A. Carvalho, J.-P. Putaud, D. Toom-Sauntry, and H. Puxbaum (2001) Results of the "carbon conference" international aerosol carbon round robin test stage I, *Atmospheric Environment*, **35** 2111-2121
32. Kim, Y.P., Seinfeld, J.H and Saxena, P (1993) Atmospheric gas-aerosol equilibrium 1. Thermodynamic model, *Aerosol Science and Technology*, **19** 157-181
33. Hedberg, E. et al. (2002) Chemical and physical characterization of emissions from birch wood combustion in a wood stove, *Atmospheric Environment,* **36** 4823-4837
34. Guyon, P. et al. (2003) Physical properties and concentration of aerosol particles over the Amazon tropical forest during background and biomass burning conditions, *Atmos. Chem. Phys.,* **3** 951-967
35. Guyon, P. et al. (2003) *Interactive* comment on "Physical properties and concentration of aerosol particles over the Amazon tropical forest during background and biomass burning conditions" by P. Guyon et al., *Atmos. Chem. Phys. Discuss.,* **3** S935-S942
36. Brockmann, J. E. and Rader, D. J. (1990) APS response to Nonspherical Particles and Experimental Determination of Dynamic Shape Factor, *Aerosol Science and Technology*, **13** 162-172
37. Marshall et al. (1991) The Behaviour of Regular-Shaped Non-Spherical Particles in a TSI Aerodynamic Particle Sizer, *J. Aerosol. Sci.,* **22** (1) 73-89
38. Hinds, W. C. (1999) *Aerosol Technology: Properties, Behavior and Measurement of Airborne Particles, 2nd Edition*, John Wiley & Sons, New York, Chapter 3
39. Carr, S. B. (2003) APS Size Shift Table, Internal DSTO Document
40. Huebert, B. J. et al. (13 September 2000) Passing Efficiency of a Low Turbulence Inlet (PELTI), *Final Report to NSF*, Honolulu, HI http://saga.pmel.noaa.gov/aceasia/platforms/lt_inlet/final_report/Pelti_ReportFinal13Sept00.pdf
41. Seinfeld, J. H. and Pandis, S. N. (1998) *Atmospheric Chemistry and Physics: From Air Pollution to Climate Change*, John Wiley and Sons, New York, page 428
42. Cleland, S. (2002) *Private Communication*, Commonwealth Bureau of Meteorology
43. Nelder, J. A. and R. Mead (1965) A Simplex Method for Function Minimization, *Computer J.*, **7** 308-313
44. Reid, J. S. et al. (2004) A Review of Biomass Burning Emissions Part III: Intensive Optical Properties of Biomass Burning Particles, *Atmos. Chem. Phys. Discuss.,* **4** 5201-5260
45. see e. g. Hanel, G. (1984) Parameterization of the influence of relative humidity on optical aerosol properties. In Aerosols and the climatic effects, Eds H.E Gerber and A, Deepak. Deepak Publishing Hampton, V.A. 117-122

46. Anderson, T. L. et al. (1996) Performance Characteristics of a High-Sensitivity, Three-Wavelength, Total Scatter/Backscatter Nephelometer, *J. Atmos. Oceanic Technol.,* **13** 967-986
47. Anderson, T. L. and Ogren, J. A. (1998) Determining Aerosol Radiative Properties Using the TSI 3563 Integrating Nephelometer, *Aerosol Science and Technology,* **29** 57-69

Appendix A: Method of Fitting Distribution Functions

As an extension to the details presented in Chapter 5.4, this Appendix briefly describes the mathematical procedure through which the size distribution functions were established. The approach here is an application of maximum likelihood parameter estimation. The parameters of the fitted function are to be determined so that the probability that the measured sample is observed, when the expected value is given by the fitted function, is maximised.

Let, y_i^* be the measured data points per channel, where each channel is defined by x_i (eg. in our case particle diameters), and where there are n channels (or size bins). The likelihood function is maximized when the following expression for the weighted least squares (WLS) function is minimised with respect to the parameters of the fitting function α, β and γ;

$$WLS(\alpha,\beta,\gamma) = \sum_{i=1}^{n} \frac{\left[y_i^* - y(x_i;\alpha,\beta,\gamma)\right]^2}{y_i^*}$$

where $y(x;\alpha,\beta,\lambda)$ is the function to be fitted at the bin diameters x_i.

The minimisation of the WLS function was performed using the non-linear conjugate gradient method in Mathcad and, for more accurate results, by the Nelder-Mead simplex direct search method [43] in MATLAB. By adjusting for noisy data in the smallest radii bins, and choosing reasonable first guess parameters (within 50% of the true values), these minimisation methods produced stable, convergent and reproducible solutions for A_i, D_{m_i} and σ_i.

The 'goodness' of fit was assessed using a χ^2 test. This statistic is defined as follows

$$\chi^2 = \sum_{i=1}^{n} \frac{\left[y_i^* - y(x_i;\alpha_0,\beta_0,\gamma_0)\right]^2}{y(x_i;\alpha_0,\beta_0,\gamma_0)}$$

where now the function is evaluated at the parameters α_0, β_0 and λ_0 that have been determined to give the best fit in the WLS sense and where the denominator is the variance in the population and not the measured sample(s). Other test statistics could be employed here, such as the Kolmogorov-Smirnov (KS) test or variants.

As a result of averaging over samples to improve particle counts there is only one sample per region (LB, UB and FT). This one sample is the sum (in terms of counts) over the entire campaign and is the best estimate of the mean total count. The particle sizing instruments (the SMPS and APS) are counting instruments and the variation in

counts between samples in a given size bin is described by a Poisson distribution (if one is to include system noise and other factors it may well be more Gaussian but for counts larger than about 5 this difference is not significant). In this case the variance in the counts is just the mean total count, which in our case can be approximated by the total count or in terms of number concentration the average over all samples (per region).

The criterion of a good fit by eye was not used explicitly to determine the fitted parameters. Not surprisingly, due to known inconsistencies in the data, quite often the statistical significance of the test failed. It should be noted that the χ^2 test will not produce good results unless indeed the sample (i.e. the measurements) are definitely from the population described by the distribution function $y(x)$. Bearing this in mind any small measurement error can affect the results profoundly. This is where understanding of the physics of how aerosol is produced, dispersed and generally behave in the atmosphere becomes important. It is not sufficient to simply let the mathematics and the statistics determine the fitted function. It is essential that understanding of the physics of aerosol size distributions guides the fitting procedure and ultimately whether the data are acceptably described by the fitted function. As noted in Gras [4], only in this way the distribution functions make sense mathematically and physically.

Appendix B: Nephelometer Issues

B.1. Relative Humidity (RH) Correction

Smoke particles are hygroscopic and will increase in size as the ambient relative humidity increases. This affects both the size distribution and the measured scattering coefficients. Both nephelometer sample RH and ambient RH were measured during the flights. At higher altitudes the RH sensor of the nephelometer was outside operating limits (5-95%) and hence a status flag was logged indicating that RH was less than 5%. The impact of RH changes on the scattering coefficient can be determined using a relationship called f(RH), with parameters calculated from a previous campaign [6]. The nephelometer deployed in the previous study was a Radiance Research Nephelometer operating at a single wavelength (530 nm). This f(RH) parameter describes the increase in scattering between a relatively dry condition and one of high humidity (in this case 20% and 80% humidity or f(RH) = $\beta_{sc}^{80\%} / \beta_{sc}^{20\%}$). This has the greatest impact on boundary layer flights, particularly those in the lowest section, or haze layer, where sample RH values were between 35-70%. In the case of higher altitude flight legs the RH changes are not important although sample heating might result in some loss of other volatile components. In all cases the nephelometer temperature was higher than the inlet temperature preventing condensation occurring inside the scattering chamber.

Gras et al. [6] found that for Northern Australia (Katherine) f(RH) lies predominantly between 1.1 and 1.7 (95% confidence limit). The median f(RH) for the Katherine flights was 1.37, which can be compared with 1.65 for sampling conducted in Kalimantan (Indonesian) and highlighting regional differences in biomass smoke.

Similar determinations of f(RH) were conducted, at ground level, at Jabiru during the September 2003 campaign. In this case two Radiance Research single wavelength (530nm) integrating nephelometers were operated in parallel, one measuring scattering at close to ambient RH (or wet), and the other with a dried sample stream (RH <40%). Scattering data were sorted for paired data with $RH(dry) \in (20,40)$ and $RH(wet) \in (60,90)$, and f(RH) was calculated from these data pairs. For these data f(RH) was found to fall predominantly between 1.0 and 1.3 with a median f(RH) of 1.11. The difference between the Jabiru and Katherine measurements is consistent with those reported in the literature between other measurements [44], although it is difficult to draw solid conclusions about the cause of the difference. It is most likely that this reflects differences in composition and size distribution. For the free troposphere and upper boundary layer the previous determination of f(RH) in smoky conditions should be the better estimator.

To obtain the scattering coefficient at the ambient RH from that measured by the nephelometer at the sample RH, the functional relationship [45]

$$\beta_{sc}(\gamma) = \beta_{sc}(\gamma_0)(1-\gamma)^{-\xi}$$

can be used. Here γ is the ambient RH (expressed as a saturation ratio) or RH/100, γ_0 is the sample RH and $\xi = 0.23$ for the Katherine flights derived from the median f(RH) value 1.37 and $\xi = 0.08$ for the Jabiru measurements. This correction can be applied on a sample-by-sample basis or uniformly for each flight leg based on flight leg average sample and ambient RH values. The highest value RH recorded in the nephelometer on the aircraft was 67% and most samples had RH < 50%.

Scattering coefficients in this report do not have RH correction applied. Any future work inferring ambient scattering coefficients from the reported data should include these corrections.

B.2. Angular Truncation Correction

The internal geometry of the nephelometer results in truncation of the angular integration to between 7 and 170 degrees (relative to the forward direction). This has the greatest impact on light scattering in the forward direction and is especially evident when there is a large concentration of coarse mode particles, and forward scattering becomes an increasingly important part of total scattering. There is also a small error due to the slightly non-Lambertian nature of the light source. Anderson et al. [46] showed that these departures from an ideal sampling environment introduce errors for the coarse mode particles for total scatter between 20%-50% for the 3563 model integrating nephelometer. Anderson and Ogren [47] made corrections for these angular truncation errors for the 3563 nephelometer using a correction factor $C = \beta_{true} / \beta_{neph}$ relating the true and observed nephelometer scattering coefficients, for the particular nephelometer geometry. Mie scattering theory was used, with an assumption of homogenous spherical particles. For the "true" calculation the integral was taken over $0\text{-}180^0$, whereas for the "nephelometer" calculation a modified Mie-integral was performed using the measured angular sensitivity of the nephelometer. A bi-modal lognormal size distribution was assumed for two main size ranges and a range of refractive indices were used. In this report the correction factors reported by Anderson and Ogren are used, parameterised in terms of the Ångstrom exponent.

The general relationship for the correction factor C in terms of the Ångstrom exponent is $C = a + b\overset{o}{A}$. The values for a and b vary for the three wavelengths as does the Ångstrom coefficient.

Table 15: Correction factors for total scatter as a function of Ångstrom exponent.

Wavelength	*a*	*b*	$\mathring{A}(\lambda_1/\lambda_2)$
Blue	1.365	-0.156	$\mathring{A}(450/550)$
Green	1.337	-0.138	$\mathring{A}(450/700)$
Red	1.297	-0.113	$\mathring{A}(550/700)$

As the Ångstrom coefficient increases, the correction factor approaches unity. This is expected since it reflects a predominance of fine mode particles, which do not scatter as much in the forward direction. The bulk of the boundary layer median Ångstrom exponents (450/700) for September are around 2 and hence the median boundary layer correction factor at 550 nm is around 6% (1.06). In regions where the scattering data are incomplete, particularly the free troposphere, the need for angular truncation corrections is also less important, due to the lack of coarse mode aerosol.

In this report angular truncation corrections have not been applied at all. Any further analyses should allow for both RH and angular truncation corrections.

B.3. Nephelometer Performance

The sensitivity of the nephelometer is a complex function of the photomultiplier tube, filter wheel, lens, scattering chamber, light source and the particle-laden air being sampled. Calibration of the instrument is critical to ensure that proper account is taken of the variation in response of these components. During the campaigns the nephelometer was calibrated before each flight using filtered ambient air as the low span gas and 99% pure CO_2 as the high span gas. In both cases the nephelometer sampled for 300 seconds. Total calibration time took about 25 minutes including thorough purging of the chamber before and between gas measurements. When a zero baseline measurement was performed immediately after calibration the nephelometer was purged with clean air to remove all CO_2.

Calibration is not the only factor affecting the performance of the nephelometer, knowledge is also required, for example about the background signal due to wall scattering inside the nephelometer. This is a function of nephelometer usage and the 'dirtiness' of the air being sampled. Typical concentrations were very low other than when sampling directly through a plume or during take off and landing at Darwin airport. Sampling was commenced and terminated as the aircraft taxied to and from the NFT.

The process that takes into account the wall scatter is called a zero baseline measurement (ZBM). In June a ZBM was not routinely performed. A ZBM was carried out three times, once early in the campaign, then again late in the campaign and finally

on the return flight from Darwin to Adelaide. To take account of the uncertainty due to the small number of ZBM's, wall scatter noise was estimated by considering the standard deviation in wall scatter values measured before, during and after the June campaign. This should be a conservative figure, as routine evaluation of the wall scatter values for September, indicate no worse variation in the wall scatter from flight to flight when the air was much more polluted.

The values obtained were $\delta\sigma_{WS}^{B} = 3.4\times10^{-7}\,m^{-1}$, $\delta\sigma_{WS}^{G} = 2.1\times10^{-7}\,m^{-1}$ and $\delta\sigma_{WS}^{R} = 3.8\times10^{-7}\,m^{-1}$. The superscript signifies the wavelength and the subscript stands for wall scatter. For reliable detection of a signal, the minimum detection limit (MDL) was set at two times the background noise of the instrument. This knowledge that a signal is less than the MDL is useful information, for example for determination of the significance of the impact of aerosol on E/O sensors.

In the future a more detailed study of the noise properties of our nephelometer might be beneficial, for example following the analysis of Anderson [46] and Anderson and Ogren [47].

Uncertainty due to limited information on wall scatter values will contribute to uncertainty in the MDL for the June data but is not included in these analyses. This is particularly relevant for scattering coefficients for altitudes above around 2.0 km for flight 4 in June 03.

For the September campaign, routine ZBM's were performed immediately before and then again straight after each stack of horizontal flights legs for each flight. The ZBM performed after the stack of flight legs was carried out once the aircraft had reached cruising altitude for the transit back to Darwin so that pressure remained approximately the same during the ZBM. Typically a stack of horizontal flight legs took about 3 hours to complete with the highest altitude legs always flown first where the air is clean especially in the free troposphere. The nephelometer was generally only sampling in the haze layer, where concentrations were high, for two to three hours. It is recommended to perform a ZBM once every hour, with a modified approach being needed in very contaminated air (ground based pollution studies) or very clean air (artic zones). The aircraft took less than 5 minutes to complete one flight leg, climb and turn before the commencement of the next leg. Due to this limited amount of time a ZBM was not performed after each flight leg or group of flight legs. Instead a ZMB was initiated after each completed stack of horizontal flight legs. This compromise was the best under the restriction of aircraft operation, where there is a trade off between optimal sampling requirements for each instrument, aircraft safety and logistics. Performance of a ZBM after the stack of flight legs enables determination of changes in wall scatter with time.

The difference between wall scatter values before and after each stack of flight legs was typically less than a couple of percent for all three wavelengths. Exceptions were

flights 1 and 3 where there was about a 15% and 10% difference respectively in the values for Blue.

Table 16: Nephelometer sensitivity and detection limits. The DSTO estimated values are based on the wall scatter values for June 2003 and on the noise response of the nephelometer during measurements of filtered air for September 2003.

Nephelometer Response (60 sec ave time)	Blue (450nm) $\times 10^{-7}\, m^{-1}$	Green (550nm) $\times 10^{-7}\, m^{-1}$	Red (700nm) $\times 10^{-7}\, m^{-1}$
TSI (Sensitivity)	3	2	2
Anderson (Detection limit)		2 (300 sec ave time)	
DSTO (Estimated Detection Limits)			
June 03 - Average	6.8	4.2	7.6
September 03 - Average	4.6	2.6	4.7

This analysis does not take into account calibration drift over time, also the noise level of the instrument during particle laden air sampling will possibly differ slightly from that for clean air.

The detection limits displayed in Table 16 assume a signal to noise ratio of 2. The value from Anderson [42] takes into account noise during the zeroing procedure with filtered air. TSI claim that the drift in the scattering signal is $< 2\times 10^{-7}\ m^{-1}$ at a 60 second averaging time for up to 1 hour after filtered-air reference measurements (i.e. ZBM) for a green wavelength. TSI do not define sensitivity but it assumed to mean the minimum detectable response of the instrument, defined as a signal to noise ratio. TSI values are typical 3563 sensitivities and those of Anderson are for a specific 3563 nephelometer. It is expected that there will be instrument-to-instrument variation. In particular for the DSTO nephelometer the performance and sensitivity of the Red channel does not appear optimal. In general the June measurements appear noisier than the September measurements; note that the colour filters were replaced between June and September. There were signs of some degradation in the filters especially for red.

DISTRIBUTION LIST

Aerosol Characterisation in the Northern Territory of Australia during the Dry Season with an Emphasis on Biomass Burning

S. B. Carr, J. L. Gras, M. T. Hackett and M. D. Keywood

AUSTRALIA

DEFENCE ORGANISATION	**No. of copies**
Task Sponsor	
CISRD	1 (paper)
S&T Program	
Chief Defence Scientist	Shared (paper)
FAS Science Policy	
AS Science Corporate Management	
Director General Science Policy Development	
Counsellor Defence Science, London	Doc Data Sheet
Counsellor Defence Science, Washington	Doc Data Sheet
Scientific Adviser to MRDC, Thailand	Doc Data Sheet
Scientific Adviser Joint	1
Navy Scientific Adviser	Doc Data Sht & Dist List
Scientific Adviser – Army	1
Air Force Scientific Adviser	1
Scientific Adviser to the DMO	Doc Data Sht & Dist List
Information Sciences Laboratory	
Research Leader IS	Doc Data Sht & Dist List
Head IEOS	1
Dr Stuart Anderson (ISRD)	1
Task Manager: S. B. Carr	5 (paper)
J. L. Gras	1 (paper)
M. T. Hackett	1 (paper)
M. D. Keywood	1 (paper)
DSTO Library and Archives	
Library Edinburgh	1 (paper)
Defence Archives	1 (paper)
Capability Development Group	
Director General Maritime Development	Doc Data Sheet
Director General Capability and Plans	Doc Data Sheet
Assistant Secretary Investment Analysis	Doc Data Sheet
Director Capability Plans and Programming	Doc Data Sheet
Director General Australian Defence Simulation Office	Doc Data Sheet
Chief Information Officer Group	
Director General Australian Defence Simulation Office	Doc Data Sheet
Director General Information Policy and Plans	Doc Data Sheet

AS Information Strategy and Futures	Doc Data Sheet
AS Information Architecture and Management	Doc Data Sheet
Director General Information Services	Doc Data Sheet

Strategy Group

Director General Military Strategy	Doc Data Sheet
Assistant Secretary Strategic Policy	Doc Data Sheet
Assistant Secretary Governance and Counter-Proliferation	Doc Data Sheet

Navy

Maritime Operational Analysis Centre, Building 89/90 Garden Island Sydney NSW	Doc Data Sht & Dist List
Deputy Director (Operations)	
Deputy Director (Analysis)	
Director General Navy Capability, Performance and Plans, Navy Headquarters	Doc Data Sheet
Director General Navy Strategic Policy and Futures, Navy Headquarters	Doc Data Sheet

Air Force

SO (Science) - Headquarters Air Combat Group, RAAF Base, Williamtown NSW 2314	Doc Data Sht & Exec Summ

Army

ABCA National Standardisation Officer	e-mailed Doc Data Sheet
Land Warfare Development Sector, Puckapunyal	
SO (Science) - Land Headquarters (LHQ), Victoria Barracks NSW	Doc Data & Exec Summary
SO (Science), Deployable Joint Force Headquarters (DJFHQ) (L), Enoggera QLD	Doc Data Sheet

Joint Operations Command

Director General Joint Operations	Doc Data Sheet
Chief of Staff Headquarters Joint Operations Command	Doc Data Sheet
Commandant ADF Warfare Centre	Doc Data Sheet
Director General Strategic Logistics	Doc Data Sheet
COS Australian Defence College	Doc Data Sheet

Intelligence and Security Group

AS Concepts, Capability and Resources	1
DGSTA , DIO	1
Manager, Information Centre, Defence Intelligence Organisation	1
Assistant Secretary Capability Provisioning	Doc Data Sheet
Assistant Secretary Capability and Systems	Doc Data Sheet

Defence Materiel Organisation

Deputy CEO	Doc Data Sheet
Head Aerospace Systems Division	Doc Data Sheet
Head Maritime Systems Division	Doc Data Sheet
Head Electronic and Weapon Systems Division	Doc Data Sheet
Program Manager Air Warfare Destroyer	Doc Data Sheet

OTHER ORGANISATIONS

National Library of Australia	1 (paper)
NASA (Canberra)	1 (paper)

UNIVERSITIES AND COLLEGES

Australian Defence Force Academy

Library	1
Head of Aerospace and Mechanical Engineering	1
Serials Section (M list), Deakin University Library, Geelong, VIC	1 (paper)
Hargrave Library, Monash University	Doc Data Sheet

OUTSIDE AUSTRALIA

INTERNATIONAL DEFENCE INFORMATION CENTRES

US Defense Technical Information Center	1
UK Dstl Knowledge Services	1
Canada Defence Research Directorate R&D Knowledge & Information Management (DRDKIM)	1
NZ Defence Information Centre	1

ABSTRACTING AND INFORMATION ORGANISATIONS

Library, Chemical Abstracts Reference Service	1
Engineering Societies Library, US	1
Materials Information, Cambridge Scientific Abstracts, US	1
Documents Librarian, The Center for Research Libraries, US	1

SPARES	5 (paper)

Total number of copies: 37 **Printed: 20** **PDF: 17**

DEFENCE SCIENCE AND TECHNOLOGY ORGANISATION
DOCUMENT CONTROL DATA

1. PRIVACY MARKING/CAVEAT (OF DOCUMENT)

2. TITLE

Aerosol Characterisation in the Northern Territory of Australia during the Dry Season with an Emphasis on Biomass Burning

3. SECURITY CLASSIFICATION (FOR UNCLASSIFIED REPORTS THAT ARE LIMITED RELEASE USE (L) NEXT TO DOCUMENT CLASSIFICATION)

Document	(U)
Title	(U)
Abstract	(U)

4. AUTHOR(S)

S. B. Carr, J. L. Gras, M. T. Hackett and M. D. Keywood

5. CORPORATE AUTHOR

DSTO Defence Science and Technology Organisation
PO Box 1500
Edinburgh South Australia 5111 Australia

6a. DSTO NUMBER	6b. AR NUMBER	6c. TYPE OF REPORT	7. DOCUMENT DATE
DSTO-RR- 0298	AR-013-472	Research Report	August 2005

8. FILE NUMBER	9. TASK NUMBER	10. TASK SPONSOR	11. NO. OF PAGES	12. NO. OF REFERENCES
2004/1091218/1	LRR 01/205	CISRD	75	47

13. URL on the World Wide Web

http://www.dsto.defence.gov.au/corporate/reports/DSTO-RR-0298.pdf

14. RELEASE AUTHORITY

Chief,
Intelligence, Surveillance and Reconnaissance Division

15. SECONDARY RELEASE STATEMENT OF THIS DOCUMENT

Approved for public release

OVERSEAS ENQUIRIES OUTSIDE STATED LIMITATIONS SHOULD BE REFERRED THROUGH DOCUMENT EXCHANGE, PO BOX 1500, EDINBURGH, SA 5111

16. DELIBERATE ANNOUNCEMENT

No Limitations

17. CITATION IN OTHER DOCUMENTS Yes

18. DEFTEST DESCRIPTORS

Aerosols, Seasonal variations, Northern Territory, Biomass, Smoke, Atmospheric composition

19. ABSTRACT

Results are presented on the atmospheric aerosol derived from aircraft measurements in the vicinity of Jabiru in Kakadu National Park during June and September 2003. The focus of the measurements was on the biomass burning aerosol (smoke) which is ubiquitous throughout the Northern Australian dry season (June - October). Data were also obtained on the coarse mode aerosol which is composed mainly of sea salt and soil. A comprehensive characterisation was made of the aerosol microphysics, chemistry and optical properties. Additional ground based measurements were made at Jabiru to more fully characterise the chemistry of the boundary layer aerosol. A range of instrumentation was used including particle sizing instruments mounted inside the aircraft and two external aerosol spectrometer probes which were used to measure the aerosol number size distribution. Additional instrumentation included a filter-sampler to collect particles for chemical analysis, a nephelometer to measure the aerosol scattering coefficient, an absorption photometer to measure the absorption coefficient and various meteorological sensors. Results show clear differences between the beginning and the end of the dry season most notably in terms of smoke concentration aloft and the relative abundance of fresh and aged smoke. The vertical aerosol profiles changed markedly between months primarily due to the difference in mixing depth.